

國立交通大學

光電工程研究所

博士論文

利用有機金屬氣相沈積法成長氮化鎵量子侷限
發光元件之研究

**Research on Nitride-Based Quantum Confined Light
Emitting Device Grown By Metalorganic Chemical
Vapor Deposition System**

研究生： 姚忻宏

Student: Hsin-Hung Yao

指導教授： 王興宗

Advisor: Shing-chung Wang

郭浩中

Hao-Chung Kuo

中華民國九十五年六月

利用有機金屬氣相沈積法成長氮化鎵量子侷限
發光元件之研究

**Research on Nitride-Based Quantum Confined Light
Emitting Device Grown By Metalorganic Chemical
Vapor Deposition System**

研究生： 姚忻宏

Student: Hsin-Hung Yao

指導教授： 王興宗
郭浩中

Advisor: Shing-chung Wang
Hao-Chung Kuo

國立交通大學

光電工程研究所

博士論文

A dissertation

Submitted to Institute of Electro-Optical Engineering
College of Electrical Engineering and Computer Science

National Chiao Tung University

In Partial Fulfillment of the Requirements

For the Degree of

Doctor of Philosophy

In Electro-Optical Engineering

June 2006

Hsin-chu, Taiwan, Republic of China

中華民國 九 十 五 年 六 月

利用有機金屬氣相沈積法成長氮化鎵量子侷限

發光結構之研究

研究生：姚忻宏

指導教授：王興宗 教授
郭浩中 教授

國立交通大學光電工程研究所

摘要

氮化鎵材料由於擁有極寬的直接能隙結構及優異的材料特性，因此成功的開發出高亮度之藍光、綠光和紫外光之短波長發光二極體，以及藍光雷射二極體等發光元件，成為極具潛力之開發材料。為了發展下一世代的氮化鎵系發光元件以及提升元件之內部及外部的量子效率，本論文在研究以有機金屬氣相化學沉積法(Metalorganic chemical vapor deposition, MOCVD)製作氮化鎵系量子侷限發光之結構。其中包括氮化鎵系半導體微共振腔以及氮化鎵量子點等結構之開發。

在本研究中，為了製作高品質的氮化鎵系微共振腔結構，我們先發展氮化鎵系高反射率布拉格反射鏡的結構。藉由設計和模擬布拉格反射鏡的結果，選擇了氮化鋁和氮化鎵材料作為氮化鎵系的布拉格反射鏡的基材來減少布拉格反射鏡的層數和增加高反射區域的寬度。本研究利用 MOCVD 技術成長高反射率的氮化鎵系布拉格反射鏡，以優化過的磊晶參數以及不對稱的布拉格反射鏡結構，成功製作出不會崩裂的高反射率的氮化鎵系布拉格反射鏡。

接著，利用發展出的高反射率氮化鎵系布拉格反射鏡為下反射鏡以及介電質氧化物布拉格反射鏡為上反射鏡，我們成功製作出一個 3 波長長度的高品質氮化鎵系微共振腔結構。利用光激發的方式測試製作出來的氮化鎵系面射型雷射結構，已可成功在室溫下觀測到激發輻射的雷射現象，其等效的臨界電流密度為 $53\text{mJ}/\text{cm}^2$ ，證明微共振腔結構的品質已達到要求。在元件開發上，我們也成功製做了電激發式的氮化鎵系微共振腔發光元件，觀察到微共振腔對自發輻射的侷限效應並使其發光波長對注入電流有極高的穩定性及較高的光輸出量子效率。

最後，我們成功的利用 MOCVD 成長了氮化鎵量子點結構並研究中斷成長對氮化鎵量子點的效應。以優化過的磊晶參數成長氮化鎵量子點結構其量子點密度已可達到 $4.5 \times 10^{10} \text{cm}^{-2}$ 且其量子點的平均側向大小為 11.5 奈米，平均高度為 1.6 奈米。研究結果顯示中斷成長能調製量子點的大小尺寸及其發光波長。優化的中斷成長參數可以增加量子點的密度和發光效率。對未來製作氮化鎵量子點的電激發式發光元件提供了良好的基礎。

Research on Nitride-Based Quantum Confined Light Emitting Devices Grown By Metalorganic Chemical Vapor Deposition

Student: Hsin-Hung Yao

Advisor: Dr. Shing-Chung Wang

Dr. Hao-Chung Kuo

Institute of Electro-Optical Engineering
National Chiao Tung University

Abstract

GaN materials are very interested for their direct wide bandgap structures and many advantages of material properties. Therefore they are likely to be the basis of a strong development of novel family semiconductor devices, for optronics as well as for electronics. Recently, III-V nitride semiconductors have been the commercial productions with a extremely wide applications; high brightness light emitting diodes (LEDs) emitting from green to near UV can be used as any kind of lighting, room-temperature violet laser light emission has paved the way to wider possibilities in optical storage, and high-power, high-temperature electronic devices have been used in harsh environments like automotive engines, space, and avionics.

In this study, in order to develop new generation device and to resolve some material issues on nitride-based light emitting devices, we have developed the optical and electric quantum confined structure grown by metal organic chemical vapor deposition (MOCVD). They are included the developments of GaN-based microcavity structures and InGaN Quantum dots (QDs) structure.

For the fabrication of high quality nitride-based microcavity structures, we started this study from design and simulation to obtain a high reflectance nitride-based distributed Bragg reflector (DBR) with a reasonable numbers of pair and stopband width in DBR structure. The monolithically grown AlN/GaN DBR structure has been demonstrated and the fabrication issues of AlN/GaN DBR structure have been resolved. By optimizing the growth condition and developing an non-quarterwave stacks DBR structure to control the accumulative strain energy, A high reflectance AlN/GaN DBR structure with crack-free surface have been successful growth.

Using the high reflectance AlN/GaN DBR as the bottom mirror, and a dielectric oxide DBR structure as the top mirror, we have fabricated a 3λ nitride-based microcavity with the hybrid DBR mirrors resonant structure. The feasibility of this nitride-based microcavity structure is examined by the performance of optical pumped, and the laser action has been achieved under the optical pumping at room temperature with a threshold pumping energy density of about 53 mJ/cm². The nitride-based microcavity emits 448 nm with a linewidth of 0.25 nm. Following, the electrically driven device with nitride-based microcavity structure has been fabricated and the characteristics of the 3λ GaN-based microcavity light emitting device structures have been discussed. A much less red-shift with injection current and a higher output power caused by the resonance effect in this MCLED has been observed.

Finally, the electric quantum confined structure with a quantum dots (QDs) structure has also been grown and the characteristic were also been studied. We have grown a self-assembled InGaN QDs structure with the growth interruption by MOCVD. The density of InGaN QDs was about $4.5 \times 10^{10} \text{ cm}^{-2}$ with an average lateral size of 11.5 nm and an average height of 1.6 nm. The effects of the interruption time on the morphological and

optical properties were studied. The results suggested that the interruption growth could modify the size of InGaN QDs and extend the emission wavelength to the short wavelength region, and at the same time improve optical quality of the QDs.



致謝

博士論文的完成，對我來說意義非凡，是對自我的肯定，也代表著另一階段人生的開始。自 1995 年高中畢業來到新竹，到 2006 年拿到博士學位，回想過去 11 年充實的學習生活，真的是在許多人的教導、協助與鼓勵之下，才能如此順利的拿到我的博士學位。

最要感謝指導老師王興宗教授在碩士、博士這七年期間的指導與教誨，讓我學習到做學問的方法、精神及態度。老師在研究資源上的高度支持，及鼓勵學生積極參與國際學術研討會的理念，促使學生的格局提高、眼界放寬，對我的人生有著很深的影響。想起初進實驗室的莽撞與不成熟到能夠完成一本厚厚的博士論文，在此向王老師至上的最高的謝意與敬意。老師，謝謝您。

這些年來跟著實驗室一起成長，感謝實驗室學長姐和學弟妹的幫忙與討論，也感謝郭浩中老師的指導，提升了我的研究的廣度；盧廷昌學長在成果發表的幫助，不厭其煩的幫我修改論文，特此感謝。研究過程中，要感謝佳鋒學長的提攜與機台的教導，讓我能夠順利進入氮化鎵長晶的研究領域；哲偉能夠在微共振腔元件草創時期勇敢扛下製成的重責大任並漂亮的完成任務，在此時，我特別懷念三人一起奮鬥的那段日子，謝謝你們。另外，也感謝最後加入的乃方學妹在數學模擬、理論計算的幫助，讓我能順利完成論文最後的部分，也要感謝學妹在論文撰寫時期在各方面的支持，辛苦你了。

這段不算短的時間，感謝安琪學姐、維巍、昭遠、俊華和名芳這群在資格考一起唸書的伙伴，能夠認識你們，是我博士班其間最珍貴的收穫，也是我的驕傲。還要感謝小狐狸、名益、炎璋、褚立、亦中、哩哩、俞君、佩玲、金鍊、佐昀、瓊文、IRIS 等，讓我的博士生活添加了許多色彩和歡樂。

最後，要感謝我親愛的父母親，姚培華先生與李榮嬌女士，你們全心全力的支持及毫無怨言的付出，讓我能在沒有後顧之憂的情況下，克服求學路程上之顛簸，希望我讓你們能感到絲毫的驕傲。

僅以此論文獻給所有關心我及幫助我的人

忻宏 于 95 年 6 月 24 日

交通大學光電所

謙虛卑恭，知足圓滿

CONTENTS

Abstract	i
(in Chinese)	
Abstract	ii
Acknowledgement	v
Contents	vi
List of tables	viii
List of figures	ix

CHAPTER 1 Introduction

1-1	Wide Bandgap Materials – Group III-Nitride Semiconductors	1
1-2	Next Generation Devices	3
1-3	Vertical Cavity Light Emitting Devices	3
1-4	Quantum Dots Structures	6
1-5	Overview of this thesis	8
	<i>References</i>	10

CHAPTER 2 Metalorganic Chemical Vapor Deposition System

2-1	Reaction Equations	19
2-2	Gas Blending Systems	23
2-3	Reactor Chamber	24
2-4	Heating System	26
2-5	In-Situ Reflectance Monitoring During III-Nitrides Growth	27
	<i>References</i>	31

CHAPTER 3 Fabrication of the Nitride-Based Distributed Bragg Reflector

3-1	Characteristics of Distributed Bragg Reflectors	48
3-2	Fabrication Issues of Nitride-based DBR structures	52
3-3	MOCVD Growth of AlN/GaN DBR Structures Under Various Ambient Conditions	55
3-4	Suppression of Crack Generation in AlN/GaN Distributed Bragg Reflector Grown by Metal Organic	59

	Chemical Vapor Deposition	
	<i>References</i>	67
CHAPTER 4	Characteristic of Nitride-Based Microcavity Structure	
4-1	Fabrication Process of Nitride-Based Microcavity Composed of Hybrid DBR Resonator	95
4-2	Characteristics of Optically Pumped Blue GaN-Based Microcavity Structure	97
4-3	Fabrication Process of Nitride-Based Microcavity Light Emitting Device	100
4-4	Characteristics of stable emission nitride-based microcavity light-emitting devices	102
	<i>References</i>	105
CHAPTER 5	Self-Assembled InGaN Quantum Dots Grown by MOCVD System	
5-1	Introduction of Self-Assembled Nitride-Based Quantum Dots	130
	Effects of growth interruption on InGaN/GaN self-assembled quantum dots grown by metal organic chemical vapor deposition	132
	<i>References</i>	142
CHAPTER 6	Conclusions and Future Works	
	Conclusions	162
	Future Works	165
	<i>References</i>	170

List of tables

Table 1-1	Comparison of features for EEL vs VCSEL.	14
Table 2-1	The names and properties of some of a the more commonly used metalorganic (MO) compounds for III-V and II-VI MOCVD "common" implies a widely used material.	33
Table 3-1	The boundary conditions of electric and magnetic fields at each interface	70
Table 3-2	The arrangement of simulation result of DBR structure with different index contrast.	74
Table 3-3	The arrangement of surface morphologies of DBR structure grown under different ambient gases.	80
Table 3-4	Comparison of the experimental and simulated peak reflectance values of these three 30-pair AlN/GaN distributed Bragg reflectors	82
Table 3-5	The necessary parameters to calculate strain energy in AlN/GaN DBR structures.	87
Table 4-1	The parameters used in the estimation of threshold gain and threshold carrier density.	115
Table 4-2	Initial Clean (I.C.) Process	119
Table 4-3	Detail process flowchart of nitride-based MCLED structure.	121
Table 5-1	The arrangement of AFM and PL measured	154
Table 5-2	The necessary parameters for simulation of InGaN QDs structure	156
Table 5-3	The arrangement of analysis results for growth interruption effect on InGaN QDs structure	160

List of figures

Chapter 1

- Figure 1-1** Energy band diagram for an ideal abrupt heterojunction of type I between two different semiconductor materials labeled A and B. 13
- Figure 1-2** The schematic diagram of nitride-based microcavity structure 15
- Figure 1-3** Three nitride-based microcavity structures: The all-epitaxial mirrors resonator structure, one amorphous-dielectric mirrors resonator structure, and all-dielectric mirrors resonator structure. 16

Chapter 2

- Figure 2-1** Schema of EMCORE D-75 system 34
- Figure 2-2** Major components of a low pressure MOCVD system. 35
- Figure 2-3** Components functions in a low pressure MOCVD system 36
- Figure 2-4** Schema of gas blending system in MOCVD. 37
- Figure 2-5** Two types MOCVD systems (a) Vertical chamber, (b) Horizontal chamber 38
- Figure 2-6** Gas flow patterns for high speed rotating disk 39
- Figure 2-7** Schema of reactor design in MOCVD D-75 system. 40
- Figure 2-8** Picture of Filament used in EMCORE D-75 41
- Figure 2-9** Model for the growth of GaN grown by MOCVD using the LT-buffer layer 42
- Figure 2-10** Schematic of in-situ monitoring configuration. By collecting the reflection of a tungsten-Lamp light perpendicularly impinging on the wafer surface 43
- Figure 2-11** The measured reflectivity of GaN bulk layer on 44

sapphire.

- Figure 2-12** The calibration of growth rate for different nitride-based materials by in-situ reflectance measurement. 45
- Figure 2-13** The schematic diagram of the controlling apparatus for in-situ monitoring system. 46

Chapter 3

- Figure 3-1** The schematic diagram of normal incidence on a single dielectric layer. 69
- Figure 3-2** The simulation results for DBR structures with 5, 10, 20, and 30 pairs. The refraction indices of nH and nL are set as 2.4, and 2.1, respectively. 71
- Figure 3-3** The peak reflectance of DBR structures with different pair number. 72
- Figure 3-4** The simulation results for 20-pair DBR structures with $n=0.2, 0.3, 0.4,$ and $0.5,$ respectively. 73
- Figure 3-5** The simulation result of asymmetric DBR structure. 75
- Figure 3-6** The arrangement of peak reflectance and stopband width for different thickness ratio between these two composed materials of 20-pair DBR structure. 76
- Figure 3-7** The schematic structures of a 30-pair AlN/GaN DBR. 77
- Figure 3-8** The schematic of the reflectance measurement setup with normal incidence at room temperature. 78
- Figure 3-9** The surface morphologies of AlN/GaN DBR structure grown under (a) N₂, (b) H₂+N₂, and (c) H₂ ambient gas. 79
- Figure 3-10** Experimental optical reflectance spectra of three 30-pair AlN/GaN DBR (solid lines) and numerical simulations of the optical reflectance spectra (dash lines). 81

Figure 3-11	(a) Cross-section TEM image of sample A. The darker layers are AlN while the lighter layers are GaN. (b) the layer images for sample A, B, and C.	83
Figure 3-12	The arrangement of thickness of AlN and GaN layers in these three DBR samples.	84
Figure 3-13	In situ normal reflectance measurement during the growth of the Bragg mirror by a fixed measurement wavelength of 450nm. The growth time t_A was set as the AlN layer started at a reflectivity maximum, and ended at the following minimum. The growth time t_G was set as the alternating GaN layer started at a reflectivity minimum, and ended at the following maximum.	85
Figure 3-14	The schematic of these three AlN/GaN DBR structures composed with different thickness ratios.	86
Figure 3-15	The DC X-ray rocking curve of 10-pair InGaN/GaN MQW structure used in the $3\text{-}\lambda$ nitride-based microcavity structure.	88
Figure 3-16	Microphotograph images of (a) Sample A, (b) Sample B, and (c) Sample C.	89
Figure 3-17	X-ray reciprocal space maps of the 20-pair of AlN/GaN DBR around $(10\bar{1}5)$ of (a) ample A, (b) sample B, and (c) sample C	91
Figure 3-18	Parameter γ under various H. γ described the strain energy remained in whole AlN/GaN DBR structure and was determined by XRD. γ_{crack} described the strain energy remained after generating crack and was calculated from crack density on sample surface.	92
Figure 3-19	Reflectance spectra of the 20-pair AlN/GaN DBR structures measured with normal incidence at room temperature.	93

Chapter 4

- Figure 4-1** The measured reflectivity of nitride-based microcavity structure on sapphire 106
- Figure 4-2** The DCX-ray rocking curve of 10-pair InGaN/GaN MQW structure used in the $3\text{-}\lambda$ nitride-based microcavity structure. 107
- Figure 4-3** The photoluminescence spectrum of 10-pair InGaN/GaN MQW structure. 108
- Figure 4-4** (a) The schematic diagram of the overall vertical-cavity surface emitting laser structure. (b) The SEM image of the full structure. 109
- Figure 4-5** The reflectivity spectrum of the top 8-pair Ta₂O₅/SiO₂ DBR, and the bottom 20-pair AlN/GaN DBR; the peak reflectivity of the top and bottom DBRs are about 97.5% and 94% at 450 nm, respectively. 110
- Figure 4-6** The schematic diagram of setup for optical pumping nitride-based microcavity structure 111
- Figure 4-7** The PL spectrum of the GaN-based VCSEL at room temperature. 112
- Figure 4-8** The variation of laser emission spectrum with the increasing pumping energy. The laser emission wavelength is 448 nm with a linewidth of about 0.25 nm. 113
- Figure 4-9** Emission intensity versus excitation intensity of the nitride-based microcavity. The threshold energy was about 1.5 μJ . 114
- Figure 4-10** The photoluminescence spectrum of 10-pair InGaN/GaN MQW structure used in the nitride-based MCLED structure. 116
- Figure 4-11** The DCX-ray rocking curve of 10-pair InGaN/GaN MQW structure used in the nitride-based MCLED structure. 117

Figure 4-12	Reflectance of 2-pairs $\text{TiO}_2/\text{SiO}_2$ DBR and 20-pairs AlN/GaN bottom DBR The EL emission spectrum was located at 410nm in these two DBRs high reflectance spectra.	118
Figure 4-13	The Process steps of the nitride-based microcavity light emitting device on sapphire	120
Figure 4-14	(a) 2D schematic diagram of completed nitride-based MCLED structure. (b) microscopic top view image of MCLED. (c) SEM images of MCLED.	122
Figure 4-15	The setup of EL measurement system	123
Figure 4-16	The top view of light emission photograph of the MCLED at 20mA current injection	124
Figure 4-17	The IV curves of nitride-based MCLED and commercial LED structures	125
Figure 4-18	Comparison of the output power of the complete MCLEDs and without top $\text{TiO}_2/\text{SiO}_2$ DBR structure at different injection current densities.	126
Figure 4-19	EL spectra of (a) without top-DBR and (b) complete MCLED structures under various current driven.	127
Figure 4-20	The current dependence of the peak positions of the complete and without top DBR nitride-based MCLED structures.	128

Chapter 5

Figure 5-1	The schematic diagram of three heteroepitaxial growth modes.	144
Figure 5-2	The schematic diagram of the overall InGaN Quantum Dots structure.	145
Figure 5-3	(a) The in-situ reflectance trace measurement for a whole sequence of GaN epitaxial thin film on sapphire substrate. and (b) AFM image of the GaN/sapphire template.	146

Figure 5-4	(a) An typical AFM $1\ \mu \times 1\ \mu$ image of sample B with tint = 30s, (b) section analysis along dash line in (a), (c) the shape profile of a single InGaN QD structure.	147
Figure 5-5	Surface morphologies of InGaN QDs under various growth and interruption times.	148
Figure 5-6	(a) Average diameter and height in dependence of the InGaN growth time, and (b) Dependence of the density of InGaN QDs on the InGaN growth time.	149
Figure 5-7	Histograms of the dot lateral size and height distribution. (a), (b), and (c) are the lateral size distribution for sample A, B, and C, respectively. (d), (e), and (f) are the height distribution for sample A, B, and C, respectively.	150
Figure 5-8	(a) Average diameter and height in dependence of the interruption time, and (b) Dependence of the density and the coverage of InGaN QDs on the interruption time.	151
Figure 5-9	Photoluminescence spectra of sample A, B, and C at room temperature under the excitation power of 20 mW.	152
Figure 5-10	Arrhenius plots of the temperature dependence of the integrated PL for (a) sample A, (b) sample B, and (c) sample C. The solid lines are linear regressions at high temperature to extract the values of the activation energies E_a .	153
Figure 5-11	The schematic of the simulation model of InGaN QD structure.	155
Figure 5-12	The calculation result of raise energy due to the confinement effect on electrons and holes with the same In composition for these three InGaN QD samples.	157
Figure 5-13	The calculation result of raise energy due to the confinement effect on electrons and holes with the same In composition for these three InGaN QD	158

samples under various internal electric fields from 0 MV/cm to 1 MV/cm.

Figure 5-14 the calculation result of the In compositions for these three samples. The In compositions of sample A and B were 0.28 and 0.27, respectively. The In composition of sample C was determined by extensive method and the internal electric field was modified to 0.2 MV/cm.

159

Chapter 6

Figure 6-1 The simulation results of the threshold current density under various mirror loss and scattering loss.

171



Chapter 1

Introduction

1.1 Wide Bandgap Materials – Group III-Nitride Semiconductors

The III-nitrides AlN, GaN, and InN with related alloys form an interesting class of direct wide bandgap materials, which are likely to be the basis of a strong development of novel family semiconductor devices, for optronics as well as for electronics [1]. With very large band offsets in type I heterojunctions (Figure 1-1), GaN-based semiconductor devices have attracted great attentions for application not only to light source of short wavelength, but also high-speed/high-power electron device [2]. These areas where Si and other III-V semiconductors can not be used have many potential applications. Actually, III-nitrides are particularly suitable for applications in these areas based on their unique properties including wide bandgap ($\sim 0.9\text{-}6.1\text{eV}$), high bond energy ($\sim 2.3\text{eV}$), high-saturation velocity ($\sim 2.7 \times 10^4 \text{ cm/s}$), high-breakdown field ($\sim 2 \times 10^6 \text{ V/cm}$), and strong excitonic effects ($> 50 \text{ meV}$) [3, 4]. Furthermore, Wurtzite III-nitrides exhibit large effect of spontaneous and strain induced polarization from the noncentrosymmetric and uniaxial crystals and the piezoelectric coefficients are almost an order of magnitude larger than in traditional III-V compounds such as GaAs. The very strong internal electric field induced by the polarization charge and piezoelectricity is very unique to III-nitride heterostructures and has a dramatic effect on the properties of quantum structures [5].

III-V nitride semiconductors have been the commercial production of high brightness light emitting diodes (LEDs) emitting from green to near UV with a extremely wide applications [6-10]; standard green to violet LEDs are currently used in traffic light, full colour displays, automotive panel instruments, and any kind of lighting. UV LEDs can be application in detection of bio particular, air and water purification, and medical treatment and diagnosis. Indeed, the white LEDs can be achieved by covering either a blue or a UV LED with appropriate phosphorescent dyes, and therefore it is a candidate for using as general illumination. When the time comes, LEDs for lighting will save a huge power since lighting accounts for about 20% of the world's total electricity consumption [11].



The demonstration of room-temperature violet laser light emission in InGaN MQW based heterostructures under continuous-wave operation has paved the way to wider possibilities in optical storage. There are the new generation of high density digital versatile disk (HD-DVD) called, using a 405nm LD with an output of 30mW. Because of the smaller the λ value, the smaller the spot and the higher the storage density, the capacity of the Blu-ray disks will be increased up to 27Gb on a single-side, single-layer DVD-size disk [12].

On the other hand, due to the high electron saturation velocity and high breakdown field, GaN and other III-V nitride semiconductor alloys are most promising for

high-power, high-temperature electronic devices [13, 14]; such devices will be used in harsh environments like automotive engines, space, and avionics.

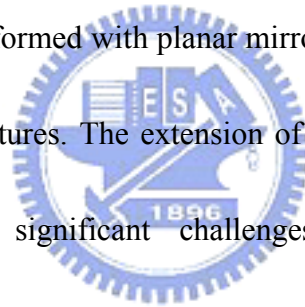
1.2 Next Generation Devices

In order to develop new generation devices and to resolve some material issues on nitride-based light emitting devices, some of efforts in the field of GaN-based device research has been already shifted to quantum dots (QDs) lasers, vertical cavity surface emitting lasers (VCSELs), UV light emitting lasers, intersubband transition devices, and field effect transistors/bipolar transistors [2]. For example, the high density of defects which were generated due to the use of foreign substrate with large lattice mismatch [15] may be resolved in nitride VCSELs structure due to the relatively small volumes of their active regions [16]. On the other hand, QDs structure in nitride-based devices not only can reduce the effect of defect density but also can reduce the threshold current density in GaN based materials due to the large effective mass in comparison with GaAs or InP based materials [2]. Therefore in this thesis, we have used metal organic chemical vapor deposition system to fabricate nitride-based microcavity structure, and InGaN QDs structure.

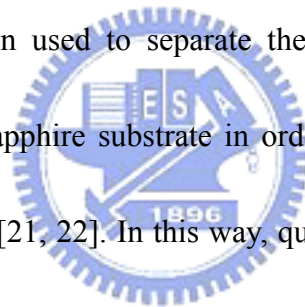
1.3 Vertical Cavity Light Emitting Devices

In generally, the technological and economical advantages in migrating from

conventional edge-emitting to surface-emitting configuration for light emitting devices are readily established, witnessed by a growing presence of VCSELs components in both tele- and data-communication technologies [17]. Some additional advantages of VCSELs with respect to edge-emitting lasers (EELs) are listed in Table 1-1. However, even in the absence of stimulated emission, resonant-cavity light emitting diodes (RC-LEDs) can also be very useful through enhanced spontaneous emission, low divergence output beams, high spectral purity, good temperature stability, and higher modulation bandwidth [18]. Both devices are characterized by the need for an optical resonator which has high quality or Q-factor and is formed with planar mirrors parallel to the growth surface of the semiconductor heterostructures. The extension of these device concepts to the blue and near-ultraviolet presents significant challenges and opportunities to III-nitrides technology. The nitride-based microcavity structure is composed of a nitride-based cavity space major included an active layer and which is sandwiched by two distributed Bragg reflectors (DBRs). The schematic structure is shown in Figure 1-2. There are three types of resonator to form nitride-based microcavity and shown in Figure 1-3, they are (1) All-epitaxial DBR resonator, (2) All-dielectric DBR resonator, and (3) Hybrid DBR resonator [19]. An acknowledged basic difficulty in applying in situ epitaxial growth techniques to form nitride-based distributed Bragg reflectors for high-Q vertical cavities is the small index of refraction contrast that is achievable within the full AlGaN alloy



range. The small contrast in the index of refraction between GaN ($n \sim 2.35$) and AlN ($n \sim 2.10$) mandates a large number of layer pairs and high aluminum fraction in a multi-layer AlGaIn distributed Bragg reflector (DBR) stack, in order to achieve sufficiently high reflectivity ($R \sim 0.99$) [20]. Furthermore, the high-reflectance region is small with a wavelength band width 10-20 nm. However, a large mismatch in the lattice constant (2.4%) implies difficulties in strain management and potential occurrence of structural defects due to strain relief which can seriously compromise the optical integrity of a high-Q microcavity. To circumvent the problems with as-grown AlGaIn DBRs, laser lift-off methods have been used to separate the InGaIn multi quantum well (MQW) heterostructure from its sapphire substrate in order to encase it within a high-Q cavity with two dielectric DBRs [21, 22]. In this way, quasi-continuous-wave optically pumped vertical-cavity lasing [21] and resonant-cavity LED operation [22] have been achieved in the 405-415 nm range, at excitation levels comparable to the equivalent current injection in a good edge-emitting diode laser. However, the obvious obstacle to fabricate all-dielectric DBR resonator is posed by the need to separate the nitride-based cavity space from the sapphire substrate. Therefore, the hybrid DBR resonator composed of one in situ grown AlGaIn DBR and one dielectric DBR is hopeful to form high quality nitride-based microcavity [23].

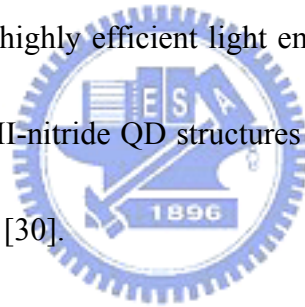


1.4 Quantum Dots Structures

During the last decade, the impressive progress in the epitaxial crystal growth techniques, such as molecular beam epitaxy (MBE) and metal organic chemical vapor deposition leads that the fabrication of low-dimensional semiconductor structures is possible [24]. The effective dimension of semiconductor structure can be reduced from three dimensional bulk materials, to quasi-two dimensional quantum well systems, to quasi-one dimensional quantum wires, and even to quasi-zero dimensional quantum dots. These quantum confined structures with quantum confined effect can modify the electronic and optical properties [25]. For example, the radiative recombination lifetimes in low-dimensional III-V semiconductor structures can be improved. This is due to two factors: the forced increase in overlap of the wavefunctions for electrons and holes, and the changes in the shapes of the density of states distribution for the conduction and valence bands. This leads to higher recombination rates and a narrowing of the gain spectrum. This feature makes quantum confined semiconductor very promising for possible device applications such as an increase in quantum efficiency for LEDs and a decrease in threshold current density for lasers [26].

The quantum confined nano-structures and quantum dot (QD) structures are low-dimensional confinement structures and have many unique physical characteristics. For example, the application of QD structure in LDs has known to have lower threshold

currents due to the enhancement of excitonic effects in the quantum dots [27]. Recently, the fabrication and studies of GaN-based nano-structures have attracted a great deal of interests for potential applications in electronic and optoelectronic devices. It has been reported that the compositional inhomogeneous occurred in InGaN films could form localized In-rich regions in InGaN active layers that play a key role in increasing the efficiency and performance of optoelectronic devices [28]. It was believed that such indium-rich nanoscale structures form the localized states, similar to those of quantum dots, and the localized states can trap significant amount of carriers for radiative recombination, leading to highly efficient light emission [29]. For GaN-based materials, the report suggested that III-nitride QD structures can reduce the effect of defect density on the device performance [30].



Furthermore, QDs structures also play an important role in microcavity devices, because the drawback of such devices is that they suffer from edge effects due to carrier loss and nonradiative recombination which may limit their efficiency. Using QDs as active light sources offer many advantage to overcome such limitation, due to their zero dimensional properties [31]. Therefore, semiconductor QD structure is also a candidate for single photon emitter. QD offers several advantages as a source for single photon. The quantum efficiency and oscillator strength of the dots are very high. The dots do not suffer from photobleaching or shelving, and are stable indefinitely [32]. Unlike

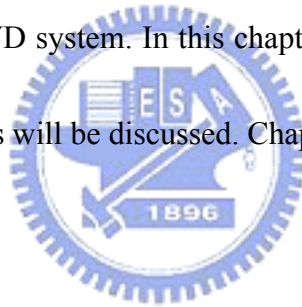
mesoscopic quantum wells, quantum dots allow the number of confined carriers to be controlled without resorting to the Coulomb blockade effect, allowing for higher-temperature operation. The materials used to make the dots are compatible with mature semiconductor technologies, allowing for the sources to be further developed and to be incorporated into larger structures. QDs structures Combine with microcavity structure to couple a single quantum dot to a single mode of a microcavity results in an efficient source of single photons [33].

1.5 Overview of this thesis

This study has focused on the fabrication of optical and electric quantum confined structure grown by metal organic chemical vapor deposition (MOCVD).

Since all the epitaxial structures in this study were grown by MOCVD system, chapter 2 reviews the fundamentals of MOCVD system which includes reaction equations, gas blending systems, reaction chamber, heating system, and in-situ reflectance monitoring. Chapter 3 reports the growth of nitride-based DBR structure used in short wavelength range. The optimized ambient gas during the growth AlN/GaN DBR structure in MOCVD system has been determined by investigating performance of DBR reflectance spectrum, and the serious problem of crack generation in AlN/GaN DBR structure was also been solved by growing an asymmetric DBR structure. After the fabrication of the high quality AlN/GaN DBR structure, an optical quantum confined

structure with a semiconductor microcavity structure has been studied. Chapter 4 reports the characteristic of nitride-based microcavity structure which is composed of a nitride-based cavity space major included an active layer and which is sandwiched by one AlN/GaN DBR structure and one dielectric oxide DBR structure. The characteristic of nitride-based microcavity structure for optical pumping and the electrically driven device has been fabricated and the characteristics will be discussed. The electric quantum confined structure with a quantum dots structure has also been grown and the characteristic were also been studied. Chapter 5 reports the self-assembled InGaN QDs structure grown by MOCVD system. In this chapter, the effect of growth interruption on self-assembled InGaN QDs will be discussed. Chapter 6 is the summary of this thesis.



References

- [1] B. Monemar, and G. Pozina, *Progress in Quantum Electronics*, 24, 239, 2000
- [2] Y. Arakawa, *IEEE Journal of Selected Topic in Quantum Electronics*, 8, 823, 2002
- [3] H. Morkoc, *Nitride Semiconductors and Devices* (Springer Verlag, Heidelberg), 1999
- [4] S. N. Mohammad, and H. MorKoc, *Progress in Quantum Electronics*, 20, 361, 1996
- [5] F. Bernardini, V. Fiorentini, and D. Vanderbilt, *PHYSICAL REVIEW B*, 56, 56, 1997
- [6] S. Nakamura and G. Fasol, *The Blue Laser Diode*. (Berlin, Germany Springer-Verlag) 1997.
- [7] I. Akasaki and H. Amano, *Jpn. J. Appl. Phys.*, 36, 5393, 1997.
- [8] S. Nakamura, M. Senoh, S. Nagahama, N. Iwasa, T. Yamada, T. Matsushita, H. Kiyoku, and Y. Sugimoto, *Jpn. J. Appl. Phys.*, 35, L74, 1996.
- [9] I. Akasaki, S. Sota, H. Sakai, T. Tanaka, M. Koike, and H. Amano, *Electron. Lett.*, 32, 105, 1996.
- [10] S. Nakamura, M. Senoh, S. Nagahama, T. Matsushita, H. Kiyoku, Y. Sugimoto, T. Kozaki, H. Umemoto, M. Sano, and T. Mukai, *Jpn. J. Appl. Phys.*, 38, 226, 1999
- [11] Pierre Gibart, *Rep. Prog. Phys.*, 67, 667, 2004
- [12] Shuji Nakamura,^{a)} Masayuki Senoh, Shin-ichi Nagahama, Naruhito Iwasa, Takao Yamada, Toshio Matsushita, Hiroyuki Kiyoku, Yasunobu Sugimoto, Tokuya Kozaki, Hitoshi Umemoto, Masahiko Sano, and Kazuyuki Chocho, *Appl. Phys. Lett.*, 72, 2014, 1998
- [13] J. I. Pankove, M. Leksono, S.S. Chang, C. Walker, B. Van Zeghbroeck, *MRS Internet Journal of Nitride Semiconducting Research* 1, 161, 1996
- [14] S. T. Sheppard, K. Doverspike, W. L. Pribble, S. T. Allen, J. W. Palmour, L. T. Kehias, J. T. Jenkins, *IEEE Electronic Device Letters*, 20, 610, 1999
- [15] Meixner M, Kunert R, Scholl E. *Physical Review B*, 67, 195301, 2003

- [16] P. Mackowiak, and W. Nakwask, J. Phys. D: Appl. Phys. 33, 642, 2000
- [17] Kent D. Choquette, and Hong Q. Hou, Proceeding of the IEEE, 85, 1730, 1997
- [18] Danae Delbeke, Ronny Bockstaele, Peter Bienstman, Roel Baets, and Henri Benisty, IEEE Journal of Selected Topic in Quantum Electronics, 8, 189, 2002
- [19] Arto Nurmikko, and Jung Han, MRS Bulletin, 502, 2002 (Conference)
- [20] T. Someyaa) and Y. Arakawa, Appl. Phys. Lett., 73, 3653, 1998
- [21] Y.-K. Song, H. Zhou, M. Diagne, I. Ozden, A. Vertikov, A. V. Nurmikko, C. Carter-Coman, R. S. Kern, F. A. Kish, and M. R. Krames, Appl. Phys. Lett. 74, 3441, 1999.
- [22] Y.-K. Song, H. Zhou, M. Diagne, A. V. Nurmikko R. P. Schneider, Jr. C. P. Kuo, M. R. Krames, R. S. Kern, C. Carter-Coman, and F. A. Kish, Appl. Phys. Lett. 76, 1662, 2000
- [23] M. Diagne, Y. He, H. Zhou, E. Makarona, A. V. Nurmikko, J. Han, K. E. Waldrip, J. J. Figiel, T. Takeuchi, and M. Krames, Appl. Phys. Lett., 79, 3720, 2001
- [24] Y. Arakawa, phys. stat. sol. (a) 188, 37, 2001
- [25] Thierry Taliercio, Pierre Lefebvre1, Mathieu Gallart and Aur'elien Morel, JOURNAL OF PHYSICS: CONDENSED MATTER, 13, 7027, 2001
- [26] M. Rowe, M. Vehse, P. Michler, J. Gutowski, S. Heppel, and A. Hangleiter, phys. stat. sol. (c) 0, 1860, 2003
- [27] Y. Arakawa and H. Sakaki, Appl. Phys. Lett. 40, 939, 1982
- [28] D. Gerthsen*, E. Hahn, B. Neubauer, V. Potin, A. Rosenauer, and M. Schowalter phys. stat. sol (c) 0, 1668, 2003
- [29] Richard J. Warburton, Contemporary Physics, 43, 351, 2002
- [30] Y. Arakawa, T. Someya, and K. Tachibana, phys. stat. sol. (b) 244, 1, 2001
- [31] Li Jiawei, Ye Zhizhen, Nasser NM. Physica A. 16 (2003)244.
- [32] V. Zwiller, T. Aichele, and O. Benson, PHYSICAL REVIEW B 69, 165307, 2004
- [33] J. P. Reithmaier, G. Sełk, A. Löffler, C. Hofmann, S. Kuhn, S. Reitzenstein, L. V. Keldysh,

V. D. Kulakovskii, T. L. Reinecke, and A. Forchel, NATURE, 432, 197, 2004



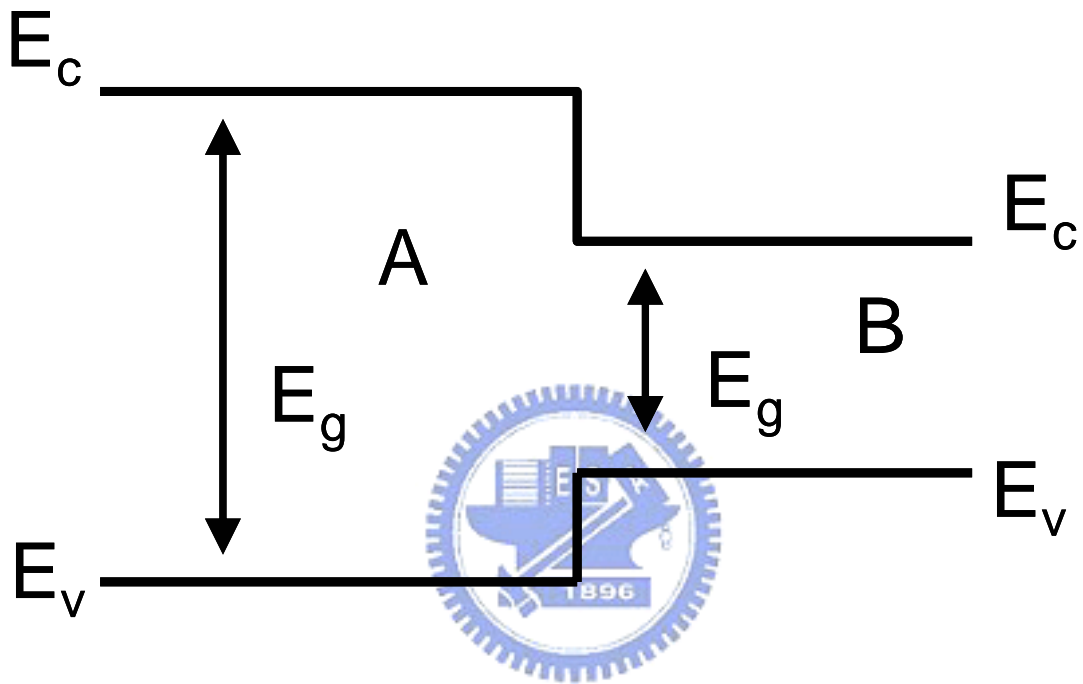


Figure 1-1 Energy band diagram for an ideal abrupt heterojunction of type I between two different semiconductor materials labeled A and B.

<i>Feature</i>	EEL	VCSEL
Spectral bandwidth	Very narrow	Narrow
Size of active area	Typically 0.5-1×2-10 μm	Variable, 5-50 μm in diameter
Beam geometry	Strong elliptic	Circular
Beam divergence	High, up to 60°×20°	Low, 5°
Number of modes	Typically 1 or few	1 or even up to many 10s
Coupling to fiber	Difficult and sensitive	Easy
Coupling efficiency	Moderate	High
Threshold current	Approximately 10 mA	Some mA
Direct modulation bandwidth	High, up to 10 Gbit/s	High, up to 10 Gbit/s
Temperature drift of P _{op}	Fairly high	Tendentially low
Environmental sensitivity	Extremely high	Moderate
Processing of chip	Very specific	Similar to LED
Final processing	Single bar	On wafer
Burn-in and functional test	Single on heatsink	On wafer

Table 1-1 Comparison of features for EEL vs VCSEL.

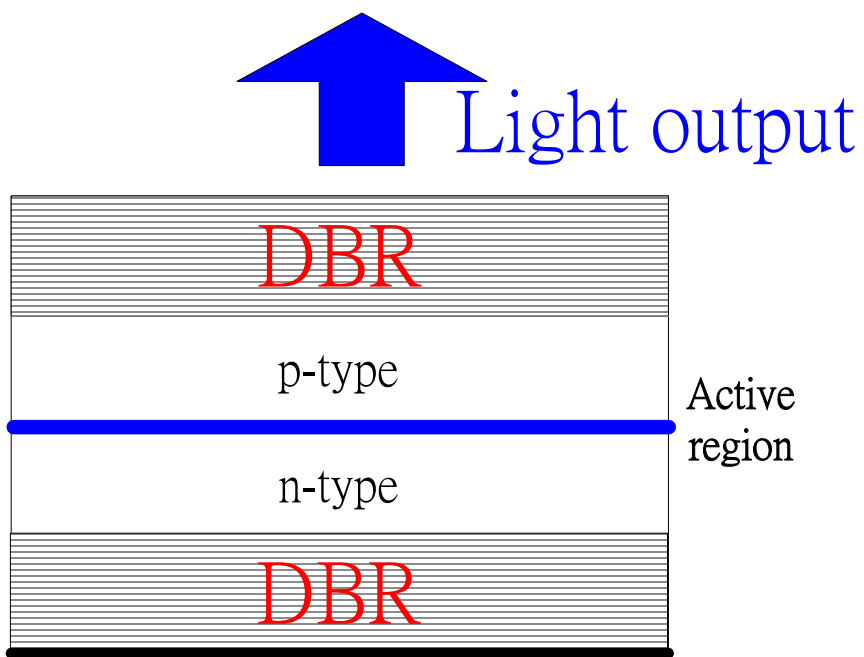


Figure 1-2 The schematic diagram of nitride-based microcavity structure.

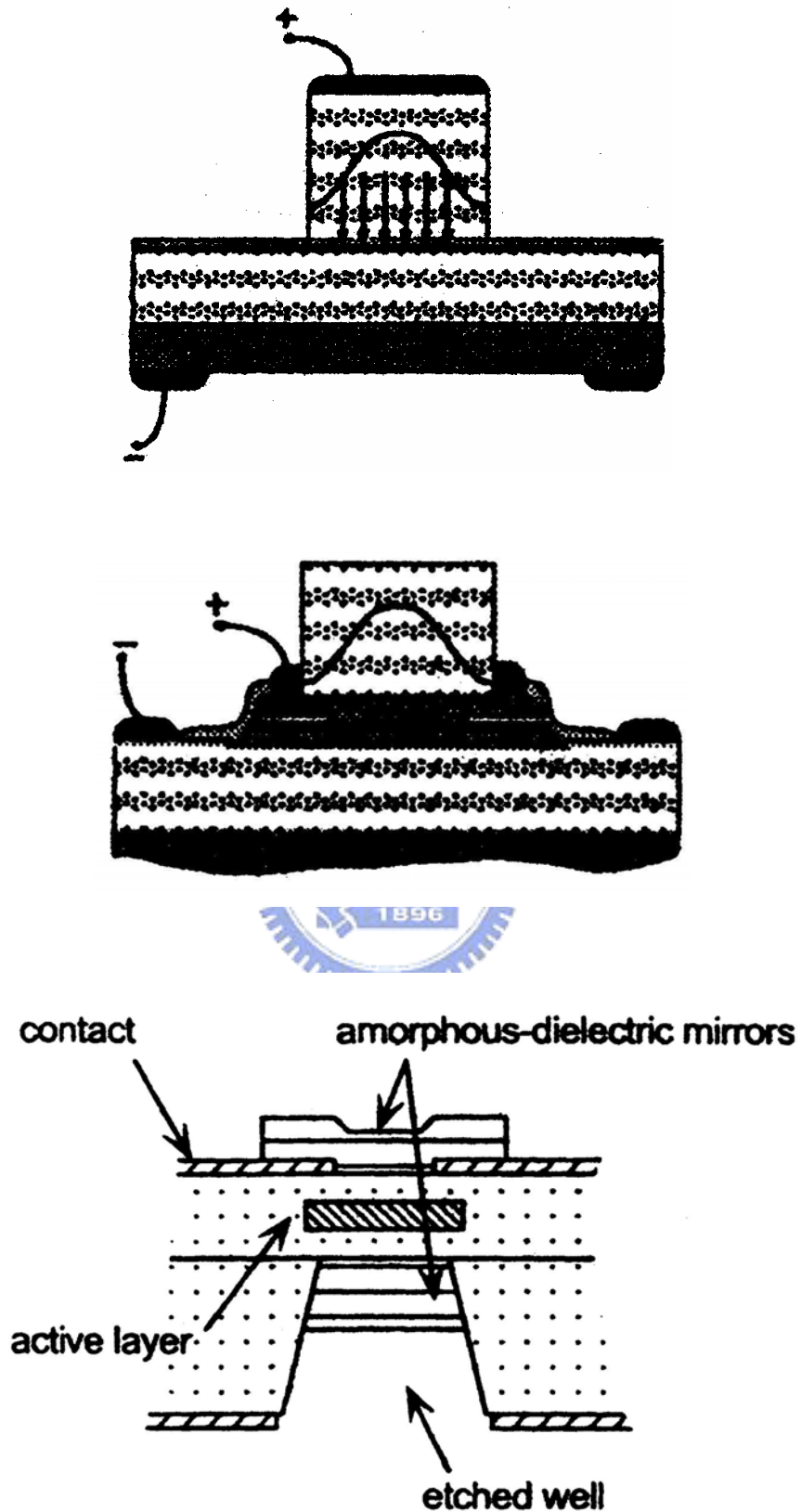


Figure 1-3 Three nitride-based microcavity structures: The all-epitaxial mirrors resonator structure, one amorphous-dielectric mirrors resonator structure, and all-dielectric mirrors resonator structure.



Chapter 2

Metalorganic Chemical Vapor Deposition System

For the past twenty years, metal organic chemical vapor deposition (MOCVD) system has become a commonly used technology for production of III-V compound semiconductor optoelectronic and electronic devices. The term “MOCVD” was originated by Manasevit [1-3], and it was used to express a form of chemical vapor deposition (CVD) utilizing the new process transported metals using organic compounds for one or more of the precursors. Alternative names included OM (OrganoMetallic) CVD, MOVPE (Vapor Phase Epitaxy), and OMVPE are all the same meaning, except epitaxy is a special case of thin film deposition where the layer replicates the crystal structure of the substrate. Because of the improvement in the material quality produced by MOCVD, many important III-V devices have become commercially viable. Indeed, the achievement of growing ultra-bright blue light emitting diodes by MOCVD [4] makes this technology be a leading candidate for manufacturing optoelectronics devices. In this dissertation, we use MOCVD system to grow all the epitaxial structures. The detailed descriptions and specific functions of MOCVD system are given in this chapter.



2.1 Reaction Equations

The MOCVD process for the growth of compound semiconductor materials and devices originated in the pioneering work has been done by H. M. Manasevit. Briefly, MOCVD process relies on vapor transport of the group III alkyls combined with group V hydrides into heated substrate. At the heated substrate, the molecules pyrolyze to produce the group III and group V elements needed for formation of desired III-V semiconductors and subsequent reaction. The simplest case in MOCVD [5] involves a pyrolysis reaction of the vapor of a volatile organometallic compound and a gaseous hydride, given by:



A and D are the constituent species for the deposited solid. R is an organic radical of some unspecified form, and many organometallic compounds have been studied as sources for the MOCVD processes. Table 2-1 [6] shows some of the more widely used MOs and their key properties. However, the lower order organic radicals are generally used, such as a methyl- or ethyl-radical, and the most important are trimethylgallium (TMGa), triethylgallium (TEGa), trimethylaluminum (TMAI), and trimethylindium (TMIn). Desirable properties include a reasonable vapor pressure at room temperature or below, high purity, low cost, a low affinity for oxygen and water vapor, and low toxicity. Unfortunately, many of the MOs that meet the vapor pressure and purity needs best are also highly reactive with oxygen. They are therefore contained in stainless steel bubblers,

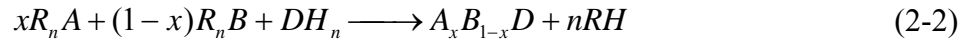
and great effort is made to avoid their contamination by air. Contrasting with V sources, metalorganic group III source are either liquids, such as TMGa, TEGa, and TMAI, or solids such as TMIIn. Therefore, the organmetallic constituents generally are transported to a heated substrate by passing a carrier gas, over or through the compound contained in a constant-temperature bubble vessel. Highly purified hydrogen or nitrogen is bubbled through the liquid to transport the material into the reactor. A knowledge of the vapor pressure (at the bubble temperature and pressure) and the carrier gas flow rate is sufficient to determine the transport rate.

On the other hand, most MOCVD growth of III-V compound semiconductors and alloys involves the use of hydrides, such as arsine, phosphine, or ammonia for the column V species. In principle, these are the simplest of column V sources to use because they are already gaseous and supplied from simple cylinder-based delivery system. In spite of the fact that they are extremely toxic, since they are relatively inexpensive with high purity layers.

The dopants processes are available in the form of MOs in bubblers (for example, Cp_2Mg), or in the form of gases (for example, SiH_4). Because of the concentration may be varied over a wide range, the dopant sources have to adjust the concentration, typically with a dilution network.

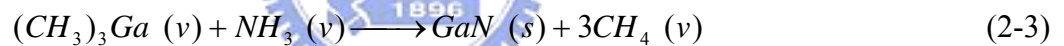
The growth of semiconductor alloys by MOCVD is easily accomplished by mixing the

vapors from the different alloy constituents in the appropriate vapor phase ratio to form the desired composition. A general equation for a ternary alloy is given by:

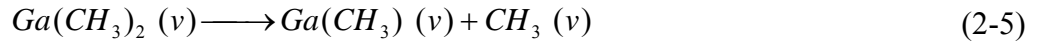


For GaN-based material growth, the first MOCVD system design for GaN growth was developed by Maruska and Tietjen [7]. Soon after, Manasevit applied this technique to grow GaN onto sapphire substrate [8]. The choice of sapphire substrate results from the facts that no GaN bulk substrate are available and a very stable material is required to deal with the high temperature required for GaN growth at around 1000°C.

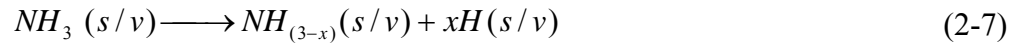
Based on the equation (2-1), the GaN epitaxy process by using MOCVD can be written:



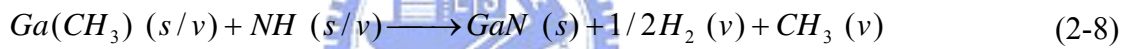
which v is vapor and s is solid. This simple equation, however, ignores the complicated reaction path and reactive species in the reactor. The incoming materials partially decompose and are then adsorbed on the surface. Then, they decompose further or are desorbed. The atoms and radicals move around on the surface with growth occurring at steps for smooth, two-dimensional layers, replicating the structure of the substrate [9]. In fact, the detail of the reaction is still unknown. Nishizawa, Abe and Kurabayashi (1985); Denbaars et al. (1996) [10] reported a reaction pathway arise from growing GaAs epitaxial layers involves homogeneous decomposition of TMGa :



In the other hand, the group V source, NH_3 , is considered to decompose heterogeneously on the GaN surface or reactor wall to provide atomic nitrogen, or a nitrogen containing radical at high grow temperature.



Combine the above mentioned equation, one possible growth mechanism of GaN that occur at the solid/vapor interface could be expressed as follows:



Although the growth mechanism of GaN can be briefly expressed by Eq. (2-8). The most difficult topic is the kinetics of the process and growth mechanism occurring at solid/vapor interface during MOCVD growth.

Optimization of MOCVD grown condition is typically done by empirical studies of external parameters such as grown temperature, V/III ratio, and mass flow rate. These studies have identified three regions of growth: mass transport limited, desorption and surface kinetically limited regimes. Conventional GaN MOCVD growth is usually performed in mass transport limited regime that takes place over a wide temperature (600~1100°C), and the growth is limited by mass transport of the column III reactant to

the growing interface.

2.2 Gas Blending Systems

The MOCVD system used in this dissertation is EMCORE D75 system and the system of EMCORE D-75 is illustrated in Figure 2-1. There are four major components in the modern MOCVD system as shown in Figure 2-2: (1) the gas blending system including the source alkyls and hydrides and all of the valves, plumbing, and instruments necessary to control the gas flows and mixtures; (2) the reactor chamber in which the pyrolysis reaction and deposition occurs; (3) the heating system used to obtain pyrolysis temperature; and (4) the vacuum and scrubbing system. All of them are controlled by a programming logical unit. The gas blending unit is responsible for transporting and mixing the precursors. The reactor chamber with a heated susceptor determines the crystal quality, the layer thickness, and the uniformity. The vacuum and scrubbing system is responsible for exhausting the gas after reaction and balancing the pressure in reactor chamber. The scrubbing system deals with the toxic gas after reaction for the safety considerations. Figure 2-3 describes the basic function of these components.

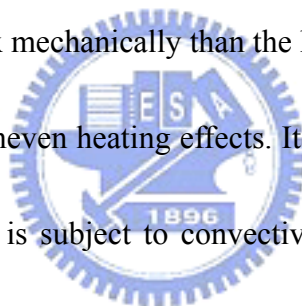
The gas blending system is illustrated in Figure 2-4. The gas blending system [11-15] for D-75 MOCVD system is a very clean, leak-free network of stainless- steel tubing, automatic valves, and electronic mass flow controllers. Hydride delivering modules

generally require a few valves and an electronic mass flow controller, since these sources are already provided as dilute, high pressure gases in gas cylinders. Alkyl delivery modules are more complicated. These high-vapor-pressure sources are contained in stainless-steel bubblers and held in a temperature-controlled bath to maintain a stable vapor pressure over the liquid or solid sources. An important part of the gas blending system is the supply of carrier gases within a vent-run configuration, show in Figure 2-4 as the injection block. The design of the injection block can avoid transients from switching or dead space. The vent-run valves couple the individual source modules to the supply line. The stable and controllable source flow rate can then be established and stabilized while the valve is vented to a waste line and prior to injection into the run supply line as shown in Figure 2-4. The absolute and differential pressures are all dynamically controlled, so that when switching of flows occurs there are no pressure transients which could upset the transition from one layer to the next. This is particularly important for quantum well based devices, which often require monoatomically abrupt interface. A main carrier gas flow is also directed to the reactor, which combination of all flows preferably taking place in the reactor.

2.3 Reactor Chamber

The reactor chamber is the vessel in which the source gases are mixed, introduced

into a heated zone where an appropriate substrate is located, and the basic pyrolysis reactions take place. The most common reaction chambers are the vertical and horizontal chamber shown in Figure 2-5 [16]. The horizontal is easy to construct provide a good glass blower and the gases flow parallel to the wafer, from one side to the other. Reactant depletion effects result in a decreasing growth rate across the wafer, which can be mitigated by tilting the wafer, increasing the carrier gas flow, and rotating the wafer. A lateral depletion effect becomes important for wider tubes, making scale-up of this geometry difficult. In the vertical geometry, the gases flow perpendicular to the wafer surface. It is more complex mechanically than the horizontal, since it is desirable to rotate the wafer to average out uneven heating effects. It is also difficult to scale up, because of worsening uniformity and is subject to convective recirculation. However, these issues can be overcome by rotating the substrate rapidly. The disk rotation pulls the incoming gases to the wafer surface, and providing the reactants are fed in uniformly across the inlet result in a uniform deposit over the entire surface. The schematic image is shown in Figure 2-6 [17].



The reactor of geometry of EMCORE D-75 system is shown in Figure 2-7, which is a vertical type chamber and made up with a double walled water-cooled stainless-steel chamber. The alkyl and hydride sources inject into the reactor via regulated mass flow controllers which are fully computer controlled. The flow rate ratio between mass flow

controllers labeled 1 to 3 for alkyls injection determines the growth rate and the uniformity of the epitaxial layer. Alkyl and hydride sources do not mix together until they reach the wafer surface in order to prevent the pre-reaction. The wafer carrier for D-75 type MOCVD contains a two-inch wafer recesses and is driven by the susceptor which was on top of a spindle rotation. The spindle rotation is by means of a high speed motor driving a toothed belt. To achieve uniformly laminar gas flow near the wafer surface at relatively low pressure, the rotation speed is 900 rounds per minute. The reactor pressure for the epitaxial growth is maintained by a throttle valve.

2.4 Heating System



The susceptor may be heated in any manner that avoids directly heating the neighboring surface, especially upstream of the sources. There have been several methods which are included RF introduction, infrared heating, and resistance heater, used in MOCVD system to heat the wafer susceptor [18-21]. In EMCORE D-75 system, the filament which is a type of resistance heater is used as heater and the image of filament is shown in Figure 2-8. The growth temperature is controlled by a temperature controller, which is better than $\pm 1^{\circ}\text{C}$ with a PID controlled ac low voltage power supply.

2.5 In-Situ Reflectance Monitoring During III-Nitrides Growth

For many years, high vacuum growth techniques such as MBE have enjoyed the advantage of using in situ diagnostic tools such as RHEED to determine substrate surface conditions and measure growth rates. Now MOCVD has responded with a variety of optical techniques to perform diagnostic on the layers as they grow [22]. Indeed, the in-situ monitoring of optical techniques is very useful for growing optoelectronic devices such as VCSELs due to the stringent requirement of phase matching. The in-situ monitoring is also an important tool to grow III-Nitride materials on foreign substrate, such as sapphire, because the limitation of homoepitaxial substrate absence is usually overcome by growing a low-temperature (LT) AlN [23] or GaN [24] nucleation layer on a sapphire substrate before the high-temperature (HT) growth. A growth mode of GaN film on sapphire substrate covered with a thin AlN buffer layer is shown in Figure 2-9. In order to realize the growth information during growing GaN, the in-situ monitoring tool is usually used to extracting growth information.

In our D-75 system, we use an in-situ normal incidence reflectance method to extract the information of growth rate and crystal quality. The tungsten-lamp reflectometry is applied as the in-situ monitoring in D-75 type MOCVD system. The schematic of the configuration is shown in Figure 2-10. Two optical heads are mounted on the top flow flange of the reactor and monitoring the growth conditions for the upper and lower points

of the wafer surface. An optical head couples two fibers; one is from the light source with the continue band wavelength, and the other is to the detector. Suppose the optic index of thin film materials is different from the substrate, the reflectance and interference from the underlying interface can be described as $R = |r|^2$, and r can be described as [25]

$$r(t) = \frac{r_{\infty} + r_i \exp(-i4\pi\beta_2)}{1 + r_{\infty} r_i \exp(-4\pi\beta_2)} \quad (2-9)$$

where $\beta_2 = 4\pi nd / \lambda$ is the phase shift in the film, r_{∞} and r_i are the reflectance of an infinitely thick film of the top layer and the internal layer reflectance, respectively.

The $\exp(-i4\pi\beta_2)$ term describe and oscillatory behavior of β_2 . Thus growth rate can be determined with the refractive index at certain growth temperature at a given wavelength.

The growth rate can be obtained by

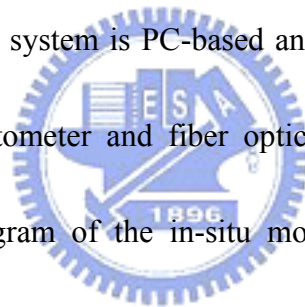
$$G_R = \lambda T_d / 2n_{\lambda} \quad (2-10)$$

where λ is the chosen wavelength, T_d is the oscillation period of the reflectivity curve, n_{λ} is the refractive index of the epitaxial layer at the growth temperature for λ . This is very useful controlling the thickness of the LT nucleation layer. Figure 2-11 shows the example for the measured reflectivity of a GaN bulk structure.

Furthermore, applying the in-situ monitoring system, we can also do temperature calibrations. In the former case, one can perform temperature calibration with eutectic wafers (Al-coated Si wafers or Silver-coated Si wafers) quickly and easily by plotting the reflectance as a function of temperature, while the temperature of the reactor is ramped

slowly. As the temperature ramps up to the melting point of aluminum or silver, 660°C, and 961°C, respectively, the reflectance would drop down rapidly. Thus one could know the meter temperature is the metal melting point. In the latter case, one can design a “calibration” structure that contains layers of different compositions or different growth conditions in a single growth run without requiring any post-growth characterization. Figure 2-12 shows the typical reflectance plot as a function of time depicting the growth of different layers for calibration of growth rate. The result shows that the growth rates of layers can be clearly judged.

The in-situ monitoring system is PC-based and integrates measurement and analysis software with spectrophotometer and fiber optic measurement hardware. Figure 2-13 shows the schematic diagram of the in-situ monitoring apparatus. Light source is a tungsten-halogen bulb that supplies light from approximately 400nm to 3000nm. This light is delivered to and collected from the sample through a fiber optic cable bundle and a lens. The intensity of the reflected light is measured at 512 different wavelengths with a spectrometer. The spectrometer uses a diffraction grating to disperse the light and a linear photodiode array to measure the light at the different wavelengths. The photodiode array operates by integrating the current generated by light falling on each of the 512 pixels. After a user-selectable integration time, the accumulated charge in each photodiode is read by the computer. Appropriate adjustment of the integration time to meet the proper signal



level.



References

- [1] J. B. Mullin, S. J. C. Irvine, and J. Tunnicliffe, *J. Cryst. Growth*, 68, 214, 1984
- [2] B. Cockayne, and P. J. Wright, *J. Cryst. Growth*, 68, 223, 1984
- [3] H. M. Manasevit, *Appl. Phys. Lett.* 12, 156, 1968
- [4] S. Nakamura, T. Muksi, and M. Senoh, *Appl. Phys. Lett.* 64, 1687, 1994
- [5] H. M. Manasevit, and W. I. Simpson, *J. Electrochem. Soc.*, 116, 1725, 1969
- [6] Alan G. Thompson, *Materials Letters*, 30, 255, 1997
- [7] H. P. Maruska, and J. J. Tietjen, *Appl. Phys. Lett.*, 15, 367, 1969.
- [8] H. M. Manasevit, F. Erdmann and W. Simpson, *J. Electrochem. Soc.*, 118, 1864, 1971
- [9] S.Yu. Karpov, V.G. Prokofjev, E.V. Yakovlev, R.A. Talalaev, Yu.N. Makarov, *MRS J. Nitride Semicond. Res.* 4, 4, 1999
- [10] S. P. DenBaar, B. Y. Maa, P. D. Dapkus, and H. C. Lee, *J. Cryst. Growth*, 77, 188, 1986
- [11] H. Kawai, I. Hase, K. Kaneko, and N. Watanabe, *J. Cryst. Growth*, 68, 406, 1984
- [12] C. C. Wang and S. H. McFarlane, III, *J. Cryst. Growth*, 13/14, 262, 1972
- [13] E. J. Thrush, J. E. A. Whiteaay, and Wale-Evans, *J. Cryst. Growth*, 68, 412, 1984
- [14] R. D. Dupuis, L. A. Moudy, and P. D. Dapkus, *Inst. Phys. Conf, Ser.*, 45, 1, 1978
- [15] J. S. Roberts, and N. J. Mason, *J. Cryst. Growth*, 68, 422, 1984
- [16] M. J. Ludowise, *J. Appl. Phys.*, 58, R31, 1985
- [17] S. Yu. Karpov, *J. Cryst. Growth*, 248, 1, 2003
- [18] H. Beneking, A. Escobosa, and H. Kraeutle, *J. Electron. Mater.*, 10, 473, 1981.
- [19] C.C. Hsu, R. M. Cohen, and G. B. Stringfellow, *J. Cryst. Growth*, 63, 8, 1983
- [20] J. P. Noda and A. J. SpringThorpe, *J. Electron. Mater.*, 9, 601, 1980.
- [21] R. H. Moss and P. C. Spurdens, *J. Cryst. Growth*, 68, 96, 1984
- [22] D. E. Aspnes, *IEEE J. Select. Topic Quant Elect.*, 1, 1054, 1995
- [23] H. Amano, N. Sawaki, I. Akasaki, and Y. Toyoda, *Appl. Phys. Lett.*, 48, 353, 1986.

[24] S. Nakamura, Jpn. J. Appl. Phys., 30, L1705, 1991

[25] W. G. Breiland, and K. P. Killeen, J. Appl. Phys., 78, 6726, 1995



Element	Name	Symbol	Vapor pressure (Torr at °C)	Liquid or Solid	Comments
Aluminum	Trimethylaluminum	TMAI	9 at 20	L	Common
Antimony	Trimethylantimony	TMSb	50 at 10	L	
Arsenic	Tertiarybutylarsine	TBAAs	125 at 20	L	high C
	Trimethylarsenic	TMAAs	300 at 25	L	
Cadmium	Diethylcadmium	DECd	1 at 30	L	
	Dimethylcadmium	DMCd	28 at 20	L	
Gallium	Triethylgallium	TEGa	3 at 20	L	Common
	Triisopropylgallium	TIPGa	1 at 25	L	
	Trimethylgallium	TMGa	65 at 0	L	Common
Indium	Ethyldimethylindium	EDMIn	2 at 20	L	
	Trimethylindium	TMIn	2 at 20	S	Common
Iron iron	Biscyclodipentadienyl	Cp ₂ Fe	1 at 20	S	Doping InP
Magnesium	Biscyclodipentadienyl-magnesium	Cp ₂ Mg	0.1 at 35	S	Sp-dopant
Phosphorus	Tertiarybutylphosphine	TBP	250 at 20	L	
Tellurium	Diethyltelluride	DETe	7 at 20	L	
Zinc	Diethylzinc	DEZn	12 at 20	L	
	Dimethylzinc	DMZn	120 at 0	L	

Table 2-1 The names and properties of some of a the more commonly used metalorganic (MO) compounds for III-V and II-VI MOCVD "common" implies a widely used material.

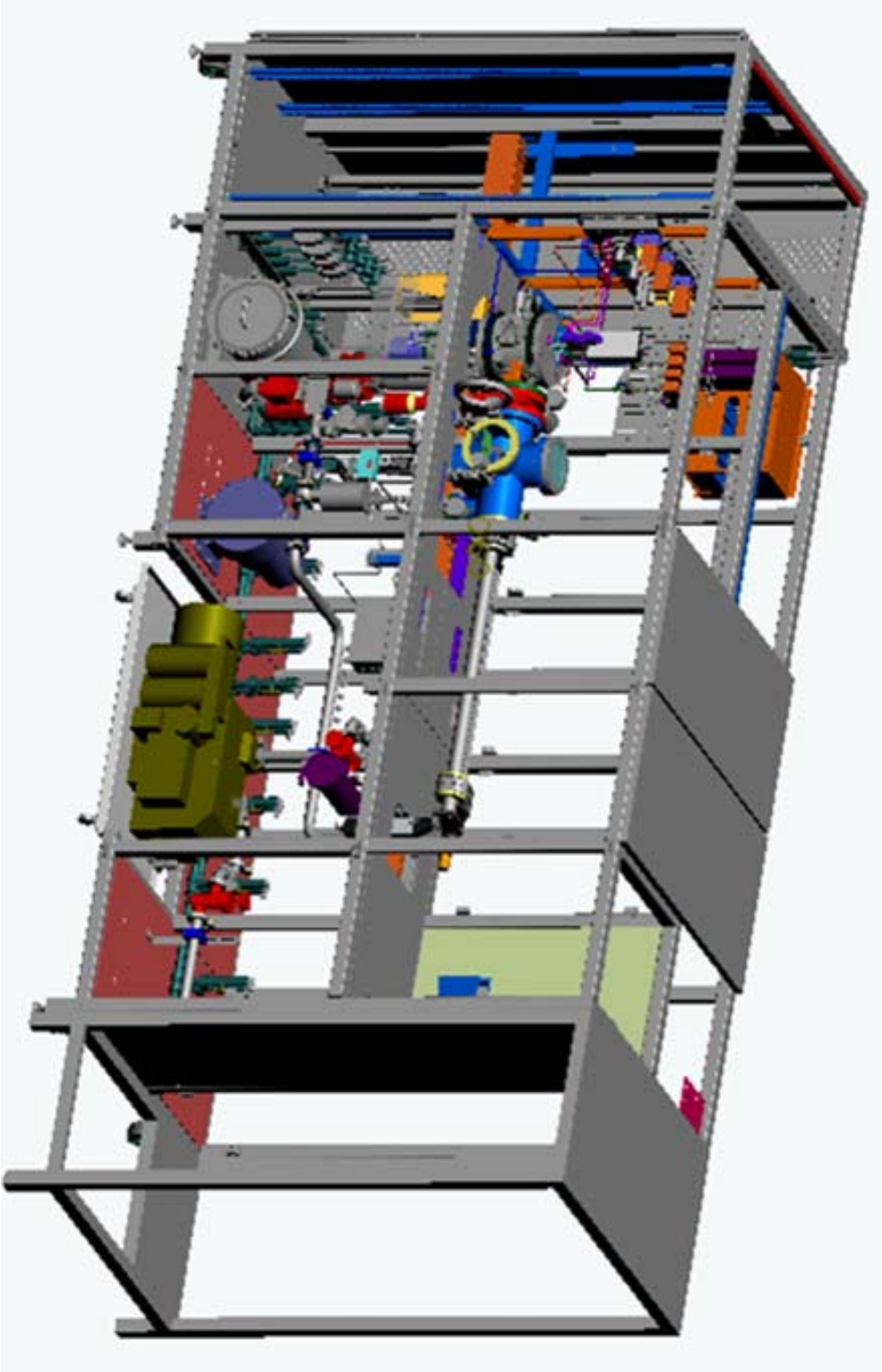


Figure 2-1 Schema of EMCORE D-75 system

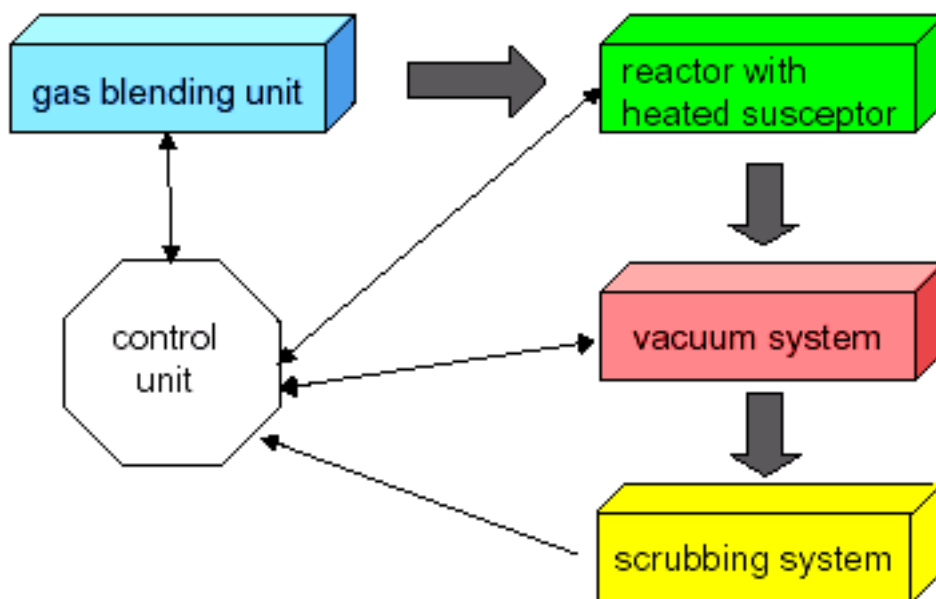


Figure 2-2 Major components of a low pressure MOCVD system.

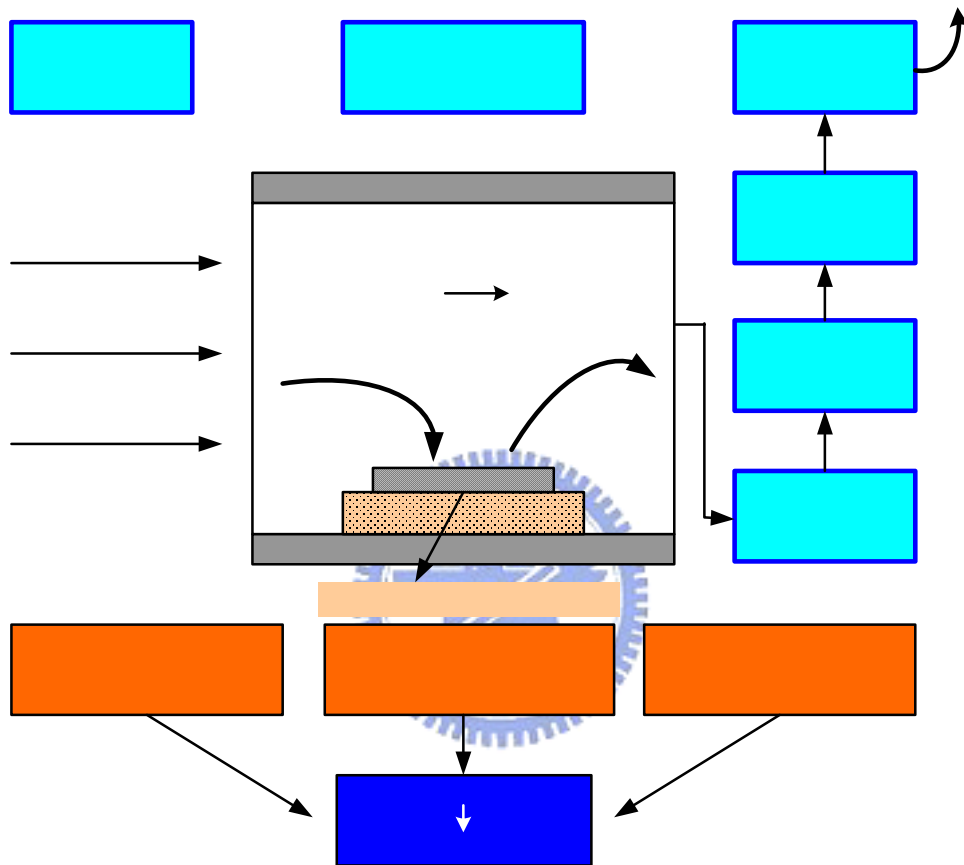


Figure 2-3 Components functions in a low pressure MOCVD system

Gas Blending

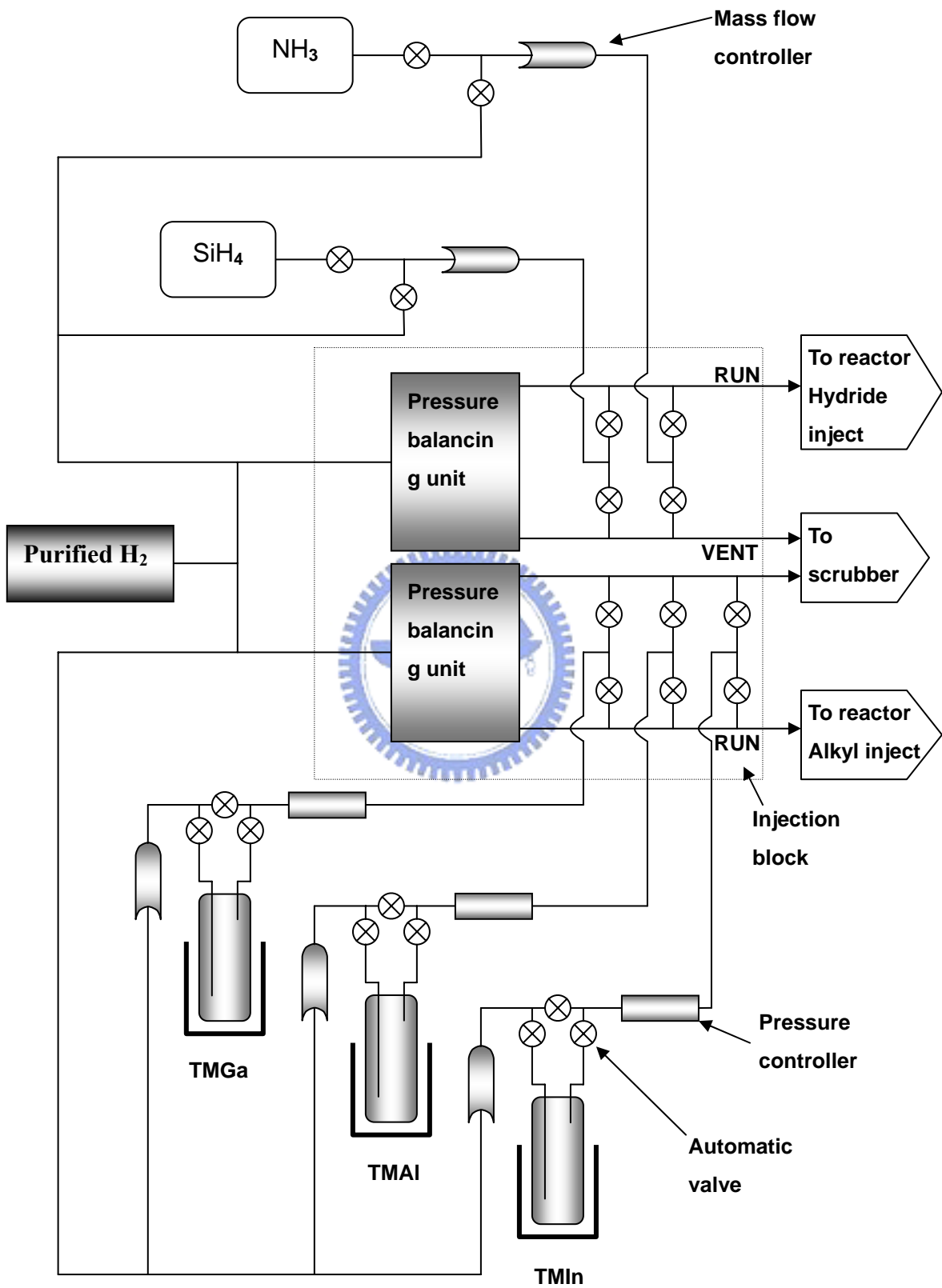


Figure 2-4 Schema of gas blending system in MOCVD.

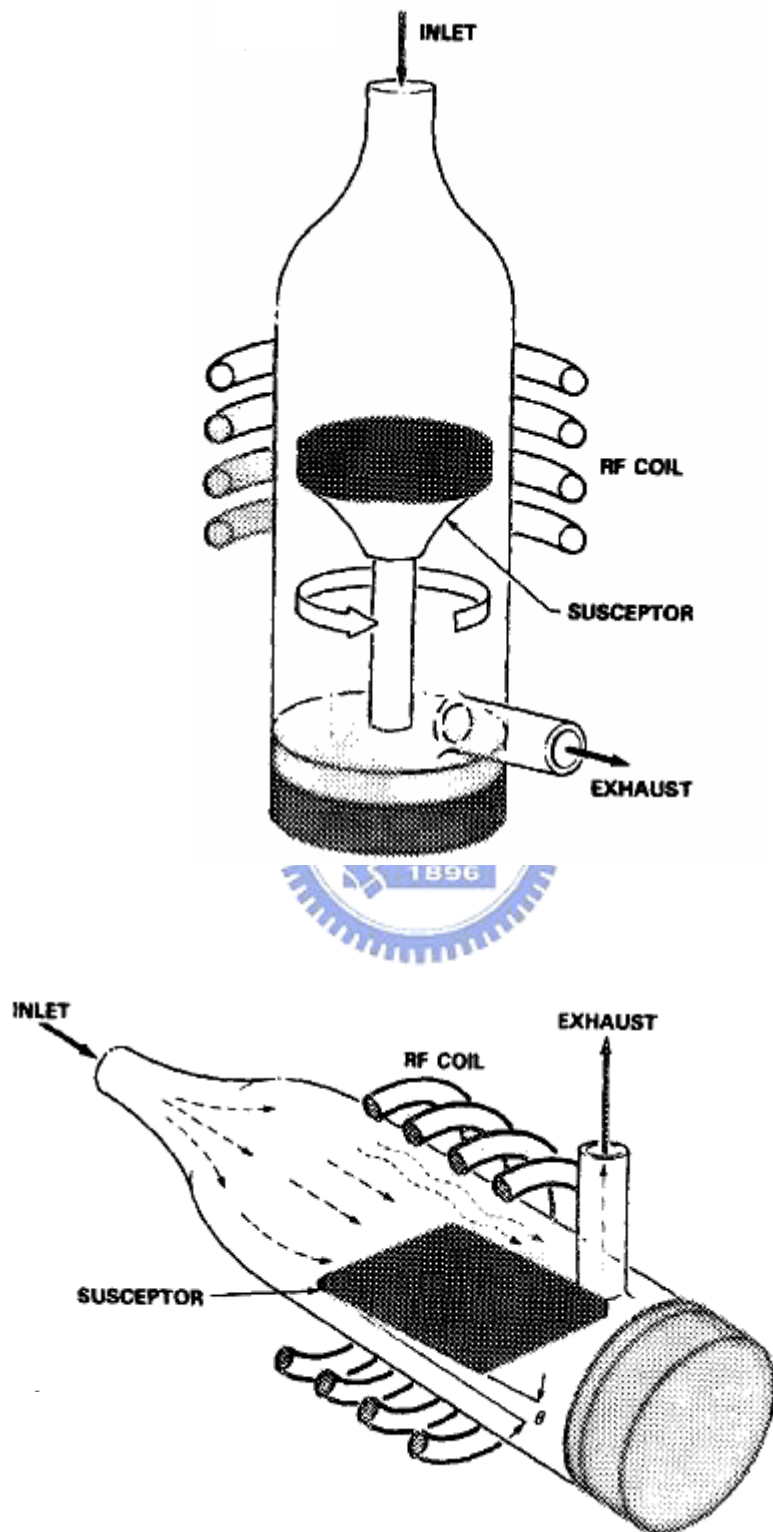
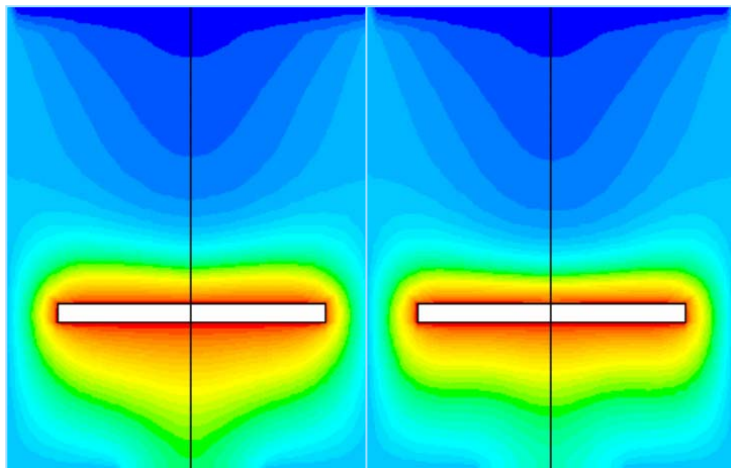
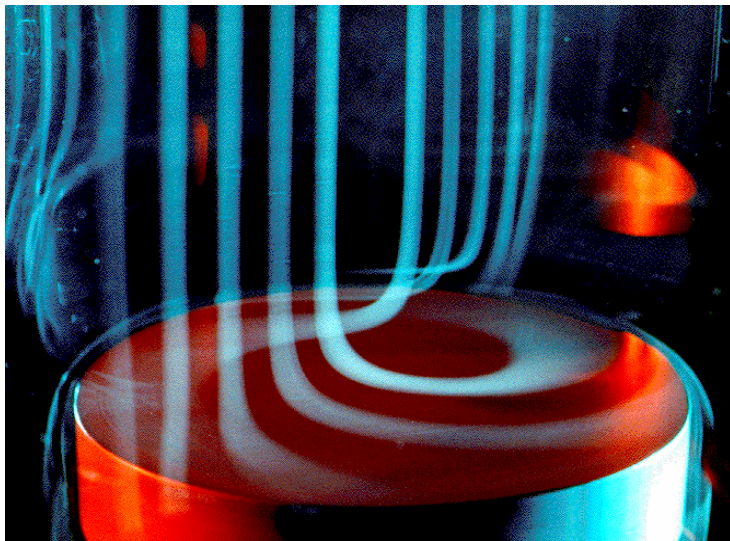
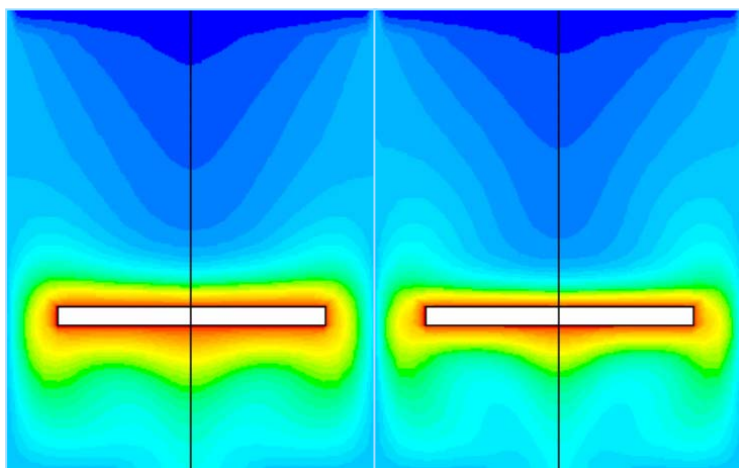


Figure 2-5 Two types MOCVD systems (a) Vertical chamber, (b) Horizontal chamber



200 RPM

400 RPM



800 RPM

1600 RPM

Figure 2-6 Gas flow patterns for high speed rotating disk

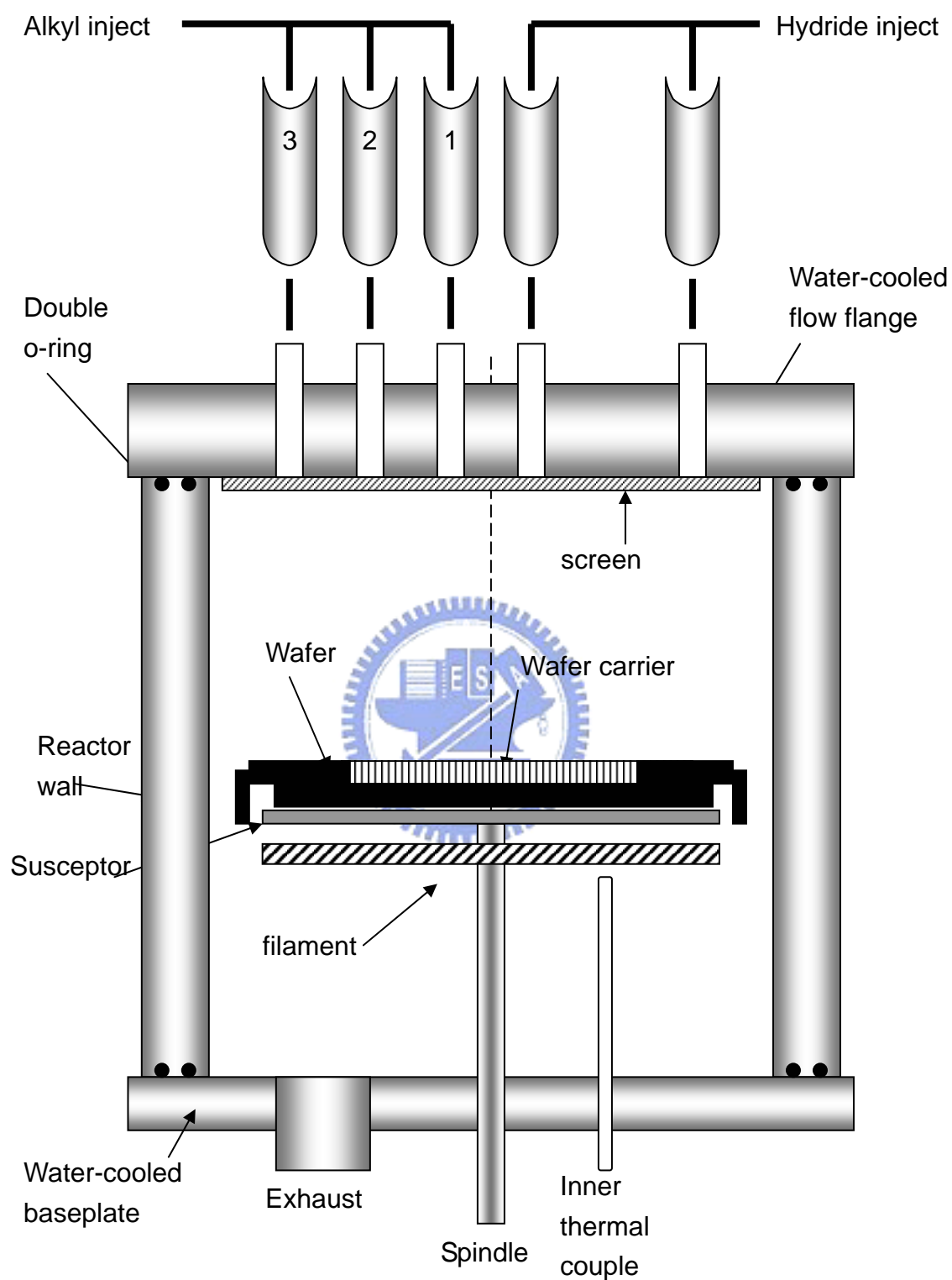


Figure 2-7 Schema of reactor design in MOCVD D-75 system.



Figure 2-8 Picture of Filament used in EMCORE D-75

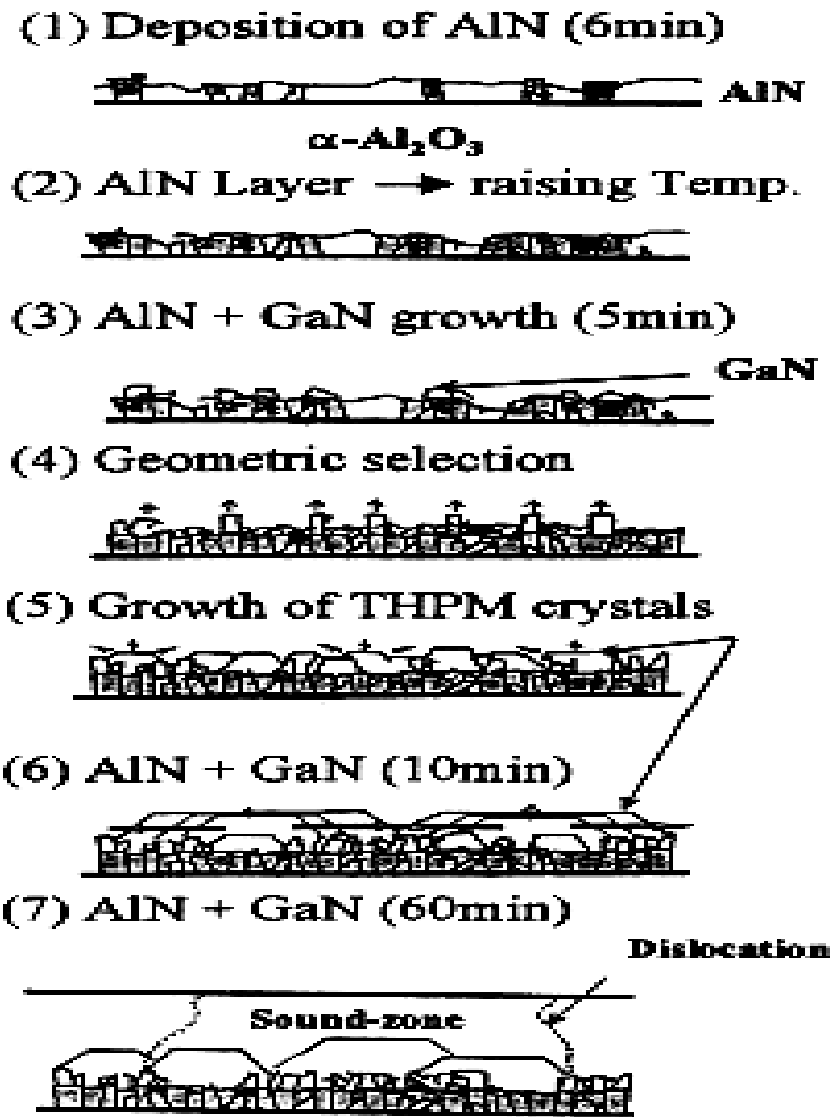


Figure 2-9 Model for the growth of GaN grown by MOCVD using the LT-buffer layer.

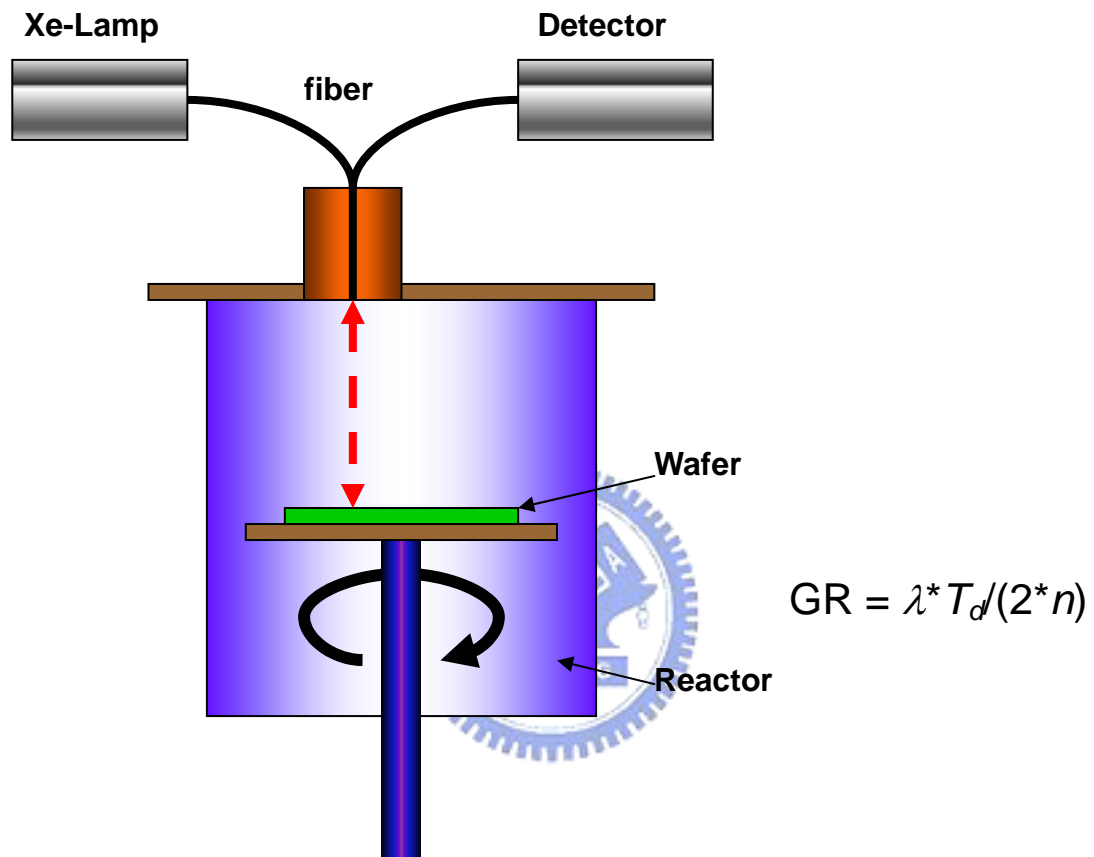


Figure 2-10 Schematic of in-situ monitoring configuration. By collecting the reflection of a Xe-Lamp light perpendicularly impinging on the wafer surface

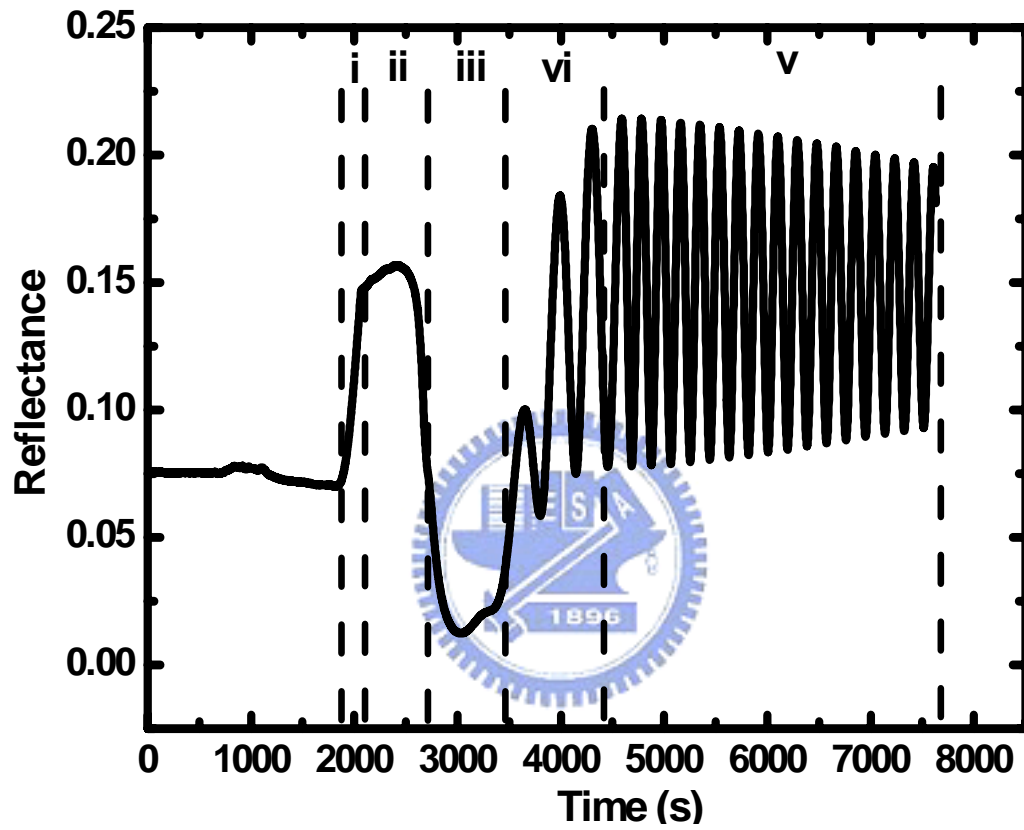


Figure 2-11 The measured reflectivity of GaN bulk layer on sapphire.

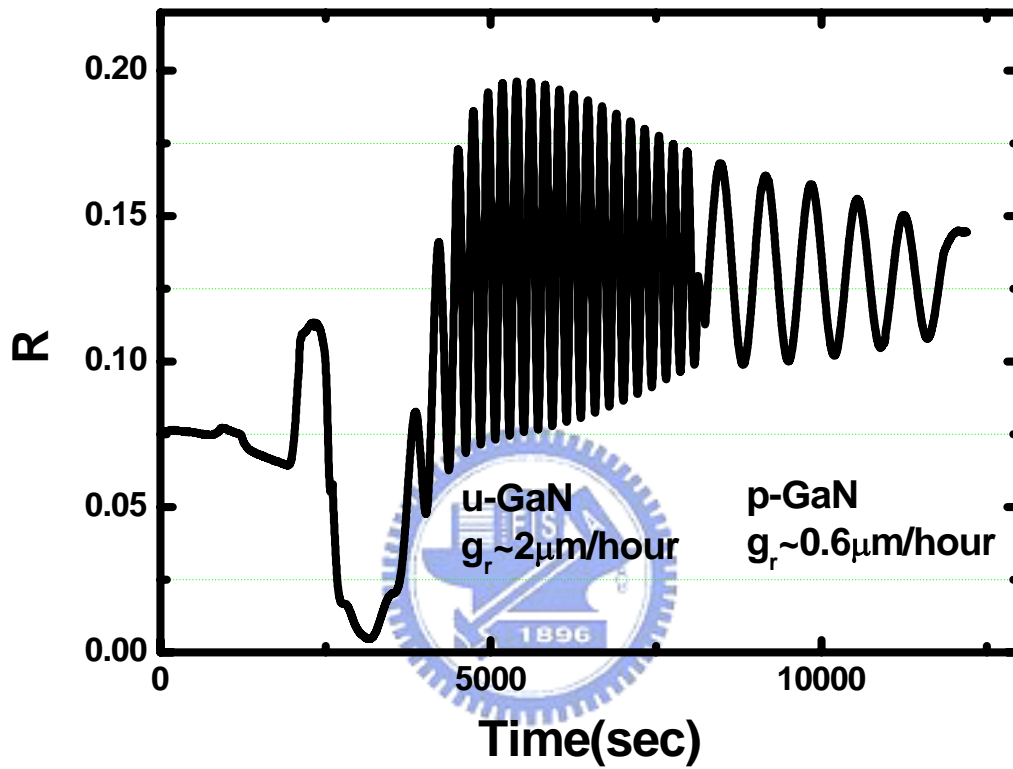


Figure 2-12 The calibration of growth rate for different nitride-based materials by in-situ reflectance measurement.

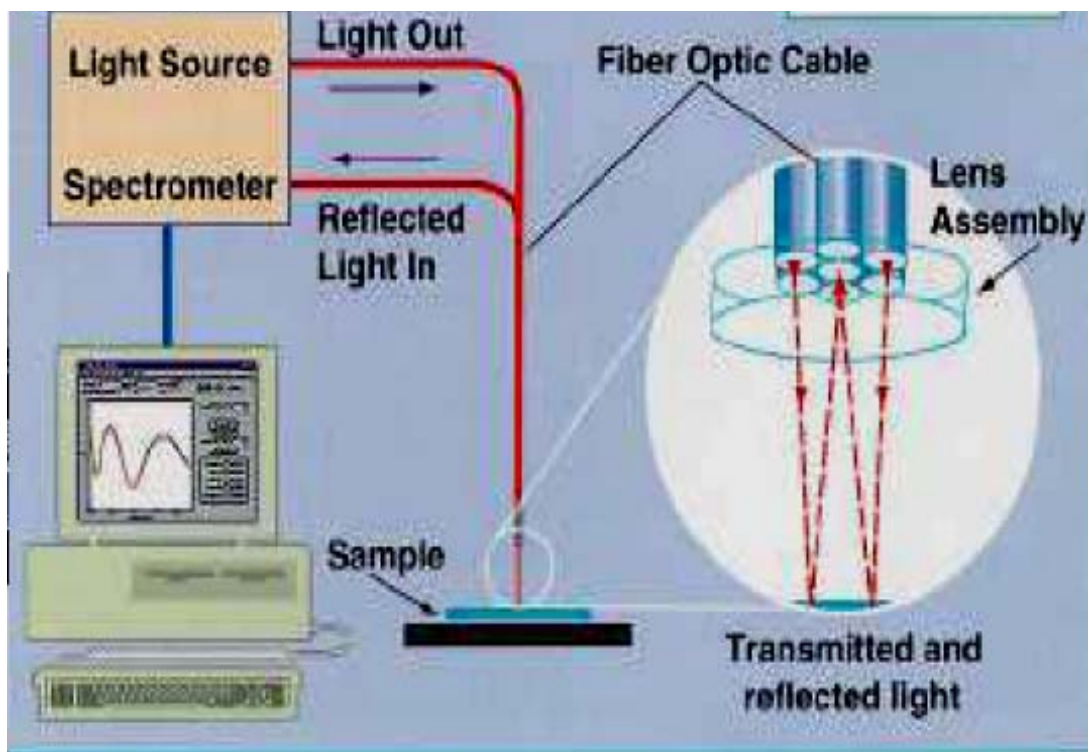


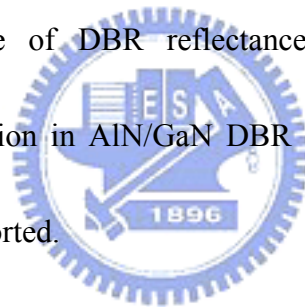
Figure 2-13 The schematic diagram of the controlling apparatus for in-situ monitoring system.



Chapter 3

Fabrication of the Nitride-Based Distributed Bragg Reflector

Chapter 3 reports the fabrication of high reflectance nitride-based distributed bragg reflector by MOCVD technique. We start this chapter with the discussion of DBRs characteristics. Following the DBR discussion, the monolithically grown issues of nitride-based DBR structure will be described. After that, the optimized ambient gas during the growth AlN/GaN DBR structure in MOCVD system has been determined by investigating performance of DBR reflectance spectrum. Finally, a technique of suppressing crack generation in AlN/GaN DBR structure with non-quarterwave stacks DBR structure will be reported.



3-1 Characteristics of Distributed Bragg Reflectors

We start this section with the transfer matrix method in stacks of thin films. We construct a computational simulation program for the transfer matrix. Then, based on the simulation, we'll discuss the DBR reflectance spectrum with different pairs, different index contrasts, and different ratios of thicknesses for the two composed materials in DBR structures.

A thin film is shown in Figure 3-1, and the dielectric of index of the thin film is n_1

with thickness L between two infinite media of indices n_0 and n_T . The amplitude of the electric vector of the normally incident light is E_0 . That of the reflected beams is E_0' , and that of the transmitted beam is E_T . The electric-field amplitudes in the film are E_1 and E_1' for the forward and backward traveling waves, respectively, as indicated in the Figure 3-1. The boundary conditions require that the electric and magnetic fields be continuous at each interface. These conditions are expressed in table 3-1. The phase factors e^{ikl} and e^{-ikl} result from the fact that the wave travels through a distance l from one interface to the other. If we eliminate the amplitudes E_1 and E_1' , we obtain

$$\begin{aligned} 1 + \frac{E_0'}{E_0} &= (\cos kl - i \frac{n_T}{n_1} \sin kl) \frac{E_T}{E_0} \\ n_0 - n_0 \frac{E_0'}{E_0} &= (-in_1 \sin kl + n_T \cos kl) \frac{E_T}{E_0} \end{aligned} \quad (3-1)$$

and we can write (3-1) in matrix form,

$$\begin{bmatrix} 1 \\ n_0 \end{bmatrix} + \begin{bmatrix} 1 \\ -n_0 \end{bmatrix} \frac{E_0'}{E_0} = \begin{bmatrix} \cos kl & -i \sin kl \\ -in_1 \sin kl & \cos kl \end{bmatrix} \begin{bmatrix} 1 \\ n_T \end{bmatrix} \frac{E_T}{E_0} \quad (3-2)$$

which can be abbreviated as

$$\begin{bmatrix} 1 \\ n_0 \end{bmatrix} + \begin{bmatrix} 1 \\ -n_0 \end{bmatrix} r = M \begin{bmatrix} 1 \\ n_T \end{bmatrix} t \quad (3-3)$$

We have here introduced the reflection coefficient

$$r = \frac{E_0'}{E_0} \quad (3-4)$$

and the transmission coefficient

$$t = \frac{E_T}{E_0} \quad (3-5)$$

The matrix, know as the *transfer matrix*

$$M = \begin{bmatrix} \cos kl & -\frac{i}{n_1} \sin kl \\ -in_1 \sin kl & \cos kl \end{bmatrix} \quad (3-6)$$

where n_1 is the index of refraction, and $k = \frac{2\pi}{\lambda} = 2\pi \frac{n_1}{\lambda_0}$. If there are N layers numbered 1, 2, 3, ... N having indices of refraction $n_1, n_2, n_3, \dots, n_N$ and thicknesses $l_1, l_2, l_3, \dots, l_N$, respectively. In the same way that we derived Equation (3-3), we can show that the reflection and transmission coefficients of the multilayer film are related by a similar matrix equation:

$$\begin{bmatrix} 1 \\ n_0 \end{bmatrix} + \begin{bmatrix} 1 \\ -n_0 \end{bmatrix} r = M_1 M_2 M_3 \dots M_N \begin{bmatrix} 1 \\ n_T \end{bmatrix} t = M \begin{bmatrix} 1 \\ n_T \end{bmatrix} t \quad (3-7)$$

Where the transfer matrices of the various layers are denoted by $M_1, M_2, M_3, \dots, M_N$. Each transfer matrix is of the form given by Equation (3-6) with appropriate values of n, l , and k . The overall transfer elements of M be A, B, C , and D , that is

$$M_1 M_2 M_3 \dots M_N = M = \begin{bmatrix} A & B \\ C & D \end{bmatrix} \quad (3-8)$$

We can then solve Equation (3-7) for r and t in terms of these elements. The result is

$$r = \frac{An_0 + Bn_T n_0 - C - Dn_T}{An_0 + Bn_T n_0 + C + Dn_T}$$

$$t = \frac{2n_0}{An_0 + Bn_T n_0 + C + Dn_T} \quad (3-9)$$

The reflectance R and the transmittance T are then given by $R = |r|^2$ and $T = |t|^2$, respectively. The detail description of **transfer matrix method** can be referred in [1].

In general, DBR structures are composed of two materials with high index n_H and low index n_L , and the thickness of each layer being $\frac{\lambda_0}{4n}$ ($n = n_H$ or n_L), Figure 3-2 shows the

reflectance spectra of 5, 10, 20, and 30 pairs DBR structures with center wavelength at 450nm. The refraction indices of n_H and n_L are set as 2.4, and 2.1, respectively. The simulation results indicate that DBR structure can be obtained a high reflectance by increasing pair number of DBR structure. Figure 3-3 shows the reflectance depends on the DBR pair numbers.

In order to know the relationship between the refraction index contrast in DBR structure and the reflectance, Figure 3-4 shows the simulation results of 20 pairs DBR structures with $\Delta n = 0.2, 0.3, 0.4,$ and $0.5,$ respectively. It can be seen that the peak reflectance and stopband width will be reduced as Δn getting small. The result also indicates that the DBR structures with low index contrast necessary increase pair number to obtain enough reflectance. Table 3-2 is the arrangement of pair number and stopband width for DBR structures with different refraction index contrast for obtaining $R=99\%$.

Based on the generalized theory of Bragg distribution, DBR structures can be composed of non-quarterwave stacks and just the thickness of each pair of DBR structure being $\frac{\lambda}{2}$. It can be described as

$$n_H d_H + n_L d_L = \frac{\lambda}{2} \quad (3-10)$$

The non-quarterwave stacks DBR structure is important for fabrication of crack-free nitride-based DBR structure, and we will have a discussion in section 3-4. Figure 3-5 shows the influences of varying the thickness ratio between these two composed

materials of 20-pair DBR structure. The simulation results of peak reflectance for 20-pair DBR structure shows that the quarterwave-stack DBR structure has the highest reflectance, and the peak reflectance will be got lower as the DBR structure become more asymmetric. The asymmetric DBR structure will also get narrower stopband width. Figure 3-6 is the arrangement of peak reflectance and stopband width for different thickness ratio between these two composed materials of 20-pair DBR structure.

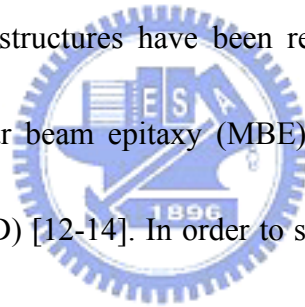
3-2 Fabrication Issues of Nitride-based DBR structures

The DBR structures are particular important for fabricating high quality GaN microcavity structure in two aspects. First, according to Honda et al. [2], the threshold current density of a GaN VCSEL can be reduced by an order of magnitude with an increase of the DBR peak reflectance from 90% to 99%. Therefore, the DBRs with high reflectivity are necessary for VCSELs. The second aspect is that the DBRs should have large stopband width. This is important because the active region of the GaN based VCSEL is typical made of InGaN multiple quantum wells (MQWs), and the emission peak of the InGaN MQWs tends to fluctuate with small variations in either the growth conditions or the process parameters [3-5]. The DBRs with wide stopband can provide sufficient coverage of such spectral variation in emission wavelength. However, the small contrast of refraction index obtained within the entire AlGaIn alloy compositions limits the stopband width of nitride-based DBR structure and it also leads a requirement of large

pair number DBR structure to achieve the necessary high reflectance. The nitride-based DBR structure with large pair number leads two issues to obtain high reflectance. First is accurately controlling the thickness of the individual layers in DBR structure. Such control is important in nitride-based DBR structure than in similar structure based on arsenides because the thicknesses of the quarterwave layers in the nitrides are 400–600 Å while those for the arsenides are approximately 800–1000 Å. In the previous report [6], H. M. Ng group used the plasma-assisted MBE to fabricate a 20.5 pairs AlN/GaN DBR structure by accurately controlling the thickness of the individual layers and obtained a high quality DBR structure with 99% at 467nm. However, it is relatively difficult for the MOCVD system to grow good structural quality and high-reflectivity AlN/GaN DBR structures, because of the difficulty in the control of the epitaxial layer thickness due to the growth of nitride-based thin film at high temperature is a competitive process between deposition and surface chemical reactions leading to etching. For example, the onset temperature for GaN decomposition is lower in H₂ ambient compared to other ambient conditions such as N₂, Ar and vacuum [7]; Rebey et al. [8] reported that the decomposition rate at 1050°C increased rapidly with increasing H₂ flow rate and at 3 slm reached 30 μm/h. The decomposition rate can be reduced by diluting the hydrogen-containing ambient and using a mixture ambient gas with N₂ and H₂. A maximum 75% reduction was achieved using a mixture of 2.5 slm (83 vol%) N₂ and 0.5



slm (17 vol%) H₂. Hence, using the MOCVD system to grow high reflectance AlN/GaN DBR structures is relatively difficult. The second aspect is that the large lattice mismatch between GaN and AlN (~2.4%) will tend to rough the interface between GaN and Al_xGa_{1-x}N, and to accumulate the tensile strain during the growth of quarterwave stacks AlGaN/GaN DBR structures. The strong tensile strain and the large different of thermal expansion coefficients between GaN (5.59 x 10⁻⁶/K) and AlN (4.20 x 10⁻⁶/K) could lead to the acute problem of crack formation on the surface. The roughness surface and crack generation result in increase of scattering loss and decrease of reflectance. Several GaN/AlGaN based DBR structures have been reported previously. These DBRs were either grown by molecular beam epitaxy (MBE) [9-11] or by metal organic chemical vapor deposition (MOCVD) [12-14]. In order to suppress these crack generations, Figiel and co-worker [12] reported the control and elimination of the tensile growth stress by insertion of multiple AlN interlayers in the GaN/AlGaN DBR structures. They have demonstrated the crack-free growth of 60 pairs of Al_{0.20}Ga_{0.80}N/GaN DBR mirrors over the entire 2 inch wafer with a maximum reflectivity of at least 99%, and the stopband width of 13nm. In addition, many research groups have studied and reported the approaches of using superlattice (SL) insertion layers to reduce the biaxial tensile strain and suppress crack generation while growing high Al-contained structures [15-19]



3-3 MOCVD Growth of AlN/GaN DBR Structures Under Various Ambient Conditions

In this section, we report the study of the ambient gas effect during the growth of AlN in AlN/GaN DBR structures by the MOCVD system. The optimal growth conditions of AlN/GaN DBRs for obtaining high optical and structural quality with high reflectivity and wide stopband width were established.

The GaN/AlN DBRs are grown on the polished optical-grade C-face (0 0 0 1) 2 inch diameter sapphire substrates by the MOCVD system (EMCORE D-75). Trimethylgallium (TMGa) and trimethylaluminum (TMAI) were used as Ga and Al sources, respectively, and ammonia (NH₃) was used as N source. A thermal cleaning process was carried out at 1080°C for 10 min in a stream of hydrogen ambient before the growth of epitaxial layers. After depositing of a 30-nm-thick GaN nucleation layer at 530°C, the temperature was raised up to 1045°C for the growth of a 1-μm-thick GaN buffer layer. The flow rate of TMGa was 89.5 mmol/min and the flow rate of NH₃ was 3.6 l/min. Then a 30-pair AlN/GaN DBR structure was grown at 1040°C under the fixed chamber pressure of 100 Torr. During the growth of GaN and AlN epitaxial layers for the DBR structures, the growth times of GaN and AlN layer were fixed at 85 and 528 s, respectively, and the flow rates of TMAI, TMGa, NH₃ were set at 74.9 mmol/min, 71.6 mmol/min and 1.2 l/min, respectively. By fixing the GaN growth condition in H₂ ambient gas with a H₂ flow rate of 3400 sccm, the AlN layer was grown under three differential ambient gas conditions.

Sample A was grown in N₂ ambient gas, sample B was grown in N₂ and H₂ mixture ambient gas (with a 35% H₂ gas), and sample C was grown in H₂ ambient gas. The ambient gas flow rate was fixed at 3400 sccm. The schematic structure of the grown DBR is shown in Figure 3-7. The surface morphology and epitaxial thickness of AlN layers were measured by atomic force microscopy (AFM), and transmission electron microscopy (TEM). The reflectivity spectrum of the AlN/GaN DBR structure was measured by the n&k ultraviolet – visible spectrometer with normal incidence at room temperature. The schematic of the setup of the reflectance measurement is shown in Figure 3-8.

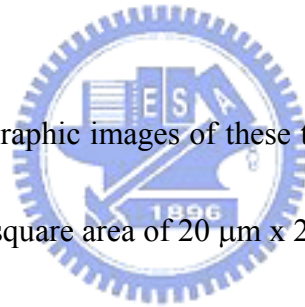
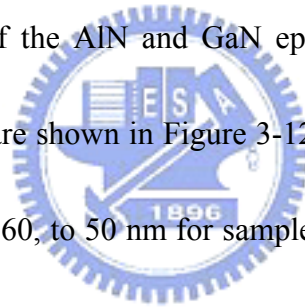


Figure 3-9 is the topographic images of these three 30-pair GaN/AlN DBR structures measured by AFM over a square area of 20 μm x 20 μm square. The roughness was slight increased from 8.1 nm, 10.7 nm, to 12.4 nm, and the grain size shows an increase from 2 μm to 10 μm by increasing the H₂ ambient gas ratio. Table 3-3 is the measured results of surface roughness. The increase in the roughness of DBR surface could be caused by the interface rough between the AlN and GaN layers at higher H₂ contents during the AlN layer growth. The reflectivity spectra of samples A, B, and C were shown in Figure 3-10 (solid line). Sample A showed the highest reflectivity of about 94.5% with a peak wavelength at 442 nm and a stopband width of 18 nm. Sample B showed a decrease in the peak reflectivity to about 92% at a blue-shifted peak wavelength of 418 nm with a

stopband width of 13 nm. For sample C, the peak reflectivity was further decreased to 79.7% with a narrower stopband width of only 6 nm at a peak wavelength further blue-shifted to 371 nm. To investigate the blue shift in the peak wavelength of the DBRs, the cross-section TEM images of these three samples were investigated. Figure 3-11 (a) shows the general view of TEM image of the entire DBR structure (30 periods) of sample A. The lighter and the darker layers are the GaN layers and AlN layers, respectively. The dislocation defect was observed in the bottom GaN bulk layer, but the dislocations did not extend into the DBR structure. Figure 3-11(b) are the layer images for samples A, B, and C. The thicknesses of the AlN and GaN epitaxial layer estimated from the TEM pictures of three samples are shown in Figure 3-12. The thickness of AlN layers shows a gradual decrease from 66, 60, to 50 nm for samples A, B, and C, respectively. The result suggests that the blue shift in the peak wavelength of the DBRs could be caused by the thickness decrease of the AlN layers. Based on the thickness data we could estimate the growth rate of AlN layer and obtained a gradual decrease of growth rate from 1.25 Å/s for sample A in pure N₂ ambient gas, 1.10 Å/s for sample B in N₂/H₂ mixture ambient gas and to 0.95 Å/s for sample C in pure H₂ ambient gas. The lower AlN growth rate in H₂ ambient gas than that in N₂ ambient gas could be due to the higher AlN decomposition rate in H₂ ambient gas than that in N₂ ambient gas. This phenomenon was also observed by Koleske et al. [20] during the growth of GaN layer. Using the thickness data obtained

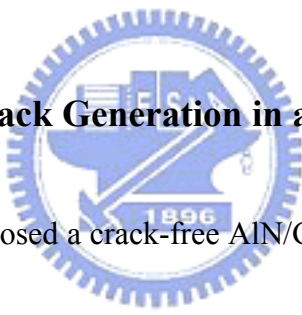


from the TEM analysis, we simulated the reflectivity spectra of the DBR structures using the transfer matrix method and fitted with the experimental spectra. The refraction index values for GaN and AlN material were adapted from the published data [21]. Since the center DBR wavelengths of these samples are all near the GaN bandedge, the estimated GaN absorption coefficient values of 150, 200 and 3385 cm^{-1} for wavelength at 440, 418 and 371 nm, respectively, from the published data of Yu et al. [22] are also used. The simulation results are plotted along with the experimental data in Figure 3-10 (dash line). Table 3-4 lists the peak reflectivity and the peak wavelength based on the simulation results and comparison with the experimental data. The simulation results suggest that the AlN layer thickness variation is a major contributing factor in the blue-shift of the peak wavelength. Besides the variation in the AlN layer thickness, the different in the surface roughness of the DBRs as observed by the AFM could also contribute to the reduction in peak reflectivity and the bandwidth narrowing of the DBR structures. From these experiment results, the H_2 ambient gas content during the growth of AlN layers in AlN/GaN DBR structures has a strong influence on the optical and structural quality of the DBR structures grown by MOCVD. For obtaining high reflectivity and wide stopband width of AlN/GaN DBR structures by MOCVD, the best condition is to grow AlN layers in the N_2 ambient gas environment.

In conclusion, the high-reflectivity AlN/GaN DBR structures were obtained by

MOCVD growth under pure N_2 ambient gas for growth of AlN epilayers. The highest peak reflectivity of about 94.5% with a stopband width of 18 nm at center wavelength of 442 nm was obtained. For the DBR structure with AlN layer grown under mixture N_2/H_2 and H_2 conditions, both the peak reflectivity and the stopband width were decreased and the center wavelengths of the DBR structures were blue-shifted. Therefore for realization of a high reflectivity and broad bandwidth of AlN/GaN DBR by using the MOCVD growth method, the pure N_2 ambient gas for growth of AlN layer should be the preferable and optimal condition.

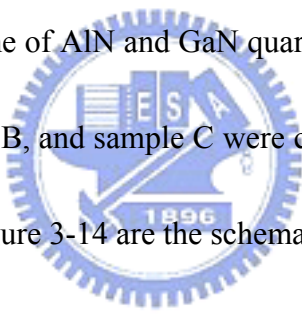
3-4 Suppression of Crack Generation in asymmetric AlN/GaN DBRs



In this section, we proposed a crack-free AlN/GaN DBR structure could be fabricated with an asymmetric DBR structure by MOCVD system. The accumulation of strain energy during grown AlN/GaN DBR structure could be controlled by controlling the thickness of AlN and GaN layers in DBR structure. By carefully selecting the thickness ratio between AlN and GaN layers to match the design center wavelength with 430nm, the high reflectivity of 96% was obtained for an asymmetric DBR with only 20 AlN/GaN pairs. No cracks were observed and the stopband width for the reflectivity spectrum was 27 nm at center wavelength around 429 nm.

The GaN/AlN DBRs were grown on C-face (0001) 2-inch diameter sapphire

substrates by the EMCORE D-75 MOCVD system. Trimethylgallium (TMGa) and trimethylaluminum (TMAI) were used as Ga and Al sources, respectively, and ammonia (NH_3) was used as N source. A 1 μm -thick GaN buffer layer was grown on the sapphire substrate, and then a 20-pair AlN/GaN DBR structure was grown at 1090°C under the fixed chamber pressure of 100 Torr. Three DBR samples have been grown with different thickness ratio of AlN and GaN layers. Sample A was a standard quarterwave stacks structure and used to determine the growth times, t_A , and t_G , of quarterwave thickness of AlN and GaN layer, respectively. The in-situ reflectance trace measurement for determining the growth time of AlN and GaN quarterwave stack is shown in Figure 3-13.



The other samples, sample B, and sample C were composed with $(0.8 t_A, 1.2 t_G)$, and $(1.2 t_A, 0.8 t_G)$, respectively. Figure 3-14 are the schematic of these three structures. In order to calculate the peak reflectance of asymmetric DBR structure composing of non-quarterwave stacks, the transmission matrix method was used to model the reflectance spectrum. The cross-section image was measured by high-resolution scanning electron microscopy. The surfaces of these samples were characterized by optical microscopy. Measurements on the reciprocal space maps (RSMs) of x-ray diffraction intensity were performed on the Philips X'Pert material research diffraction system around an asymmetrical GaN (1015) Bragg peak. And the reflectivity spectrum of the AlN/GaN DBR structure was measured by the n&k ultraviolet - visible spectrometer

with normal incidence at room temperature.

In these three AlN/GaN DBR structures, which composed of a period heterostructure, strain relief mechanisms are more complex since one has to consider both the strain in each layer and the strain in the whole DBR structure. However the thicknesses of these individual layers in DBR structure are larger than the critical thickness, AlN/GaN DBR structure was not like a coherent superlattices structure, and these individual layers would relieve strain and return their in-plane lattices constant to the unstrained state. Considering the accumulative stress σ_a during the growth of AlN/GaN DBR structure

can be written as

$$\sigma_a = N \left(\frac{\sigma_{AlN/GaN} + \sigma_{GaN/AlN}}{d_{AlN} + d_{GaN}} \right) \quad (3-11)$$

$$\sigma_{i/j} = (c_{11} + c_{12} - 2c_{13}^2/c_{33})_i \varepsilon_i \gamma d_i \quad (3-12)$$

$$\varepsilon_i = (a_i^0 - a_j^0) / a_j^0 \quad (3-13)$$

$$\gamma = 1 - \frac{a_j - a_i}{a_j^0 - a_i^0} \quad (3-14)$$

where N is the pair numbers of AlN/GaN DBR, $\sigma_{AlN/GaN}$ and $\sigma_{GaN/AlN}$ are the individual in-plane stress in AlN and GaN layers, respectively, i and j are instead of AlN or GaN, ε is the in-plane isotropic strain, γ describes the relative extent of the biaxial strain [23], c are the stiffness constants, d is the film thickness, and a and a_0 are the measured lattice parameters and the extrapolated lattice parameters for the fully relaxed case, respectively. From formula (1) and (2), the value of σ_a can be controlled by

modified the thicknesses of AlN and GaN layers in DBR structure.

The influences of varying the thickness ratio between AlN and GaN layers in DBR structure have been calculated. Figure 3-15 is the calculation result of the accumulative stress σ_a and the peak reflectance of 20-pair AlN/GaN DBR structure under different optical length parameter H, which was defined as:

$$H = \frac{n_{AlN}d_{AlN}}{n_{GaN}d_{GaN} + n_{AlN}d_{AlN}} \quad (3-15)$$

the material parameters used for calculation for AlN and GaN are listed in Table [3, 24].

In Figure 3-15, we supposed the strained-layers in DBR structure were unrelaxed ($\gamma = 1$),

and the center wavelength of DBR structure was 430nm. The calculation result indicated

that $\sigma_a = 0$ at $H = 0.43$, implying that the asymmetric AlN/GaN DBR structure with

thicker optical length $d_{GaN}n_{GaN}$ might compensate the tensile stress by the compressive

stress. From the calculation, the accumulative stress σ_a for sample A, B, and C were

-13.0 GPa, 7.3 GPa, and -29.4 GPa. Sample A, a general quarterwave-stack DBR

structure, exhibited a negative σ_a value because of the AlN thickness being larger than

the GaN thickness in one pair DBR structure. And among these three samples, sample B

is the only structure with a positive σ_a value indicated that a compressive stress could

be accumulated in one pair DBR structure. On the other hand, the calculation result of

peak reflectance for 20-pair AlN/GaN DBR structure showed that the quarterwave-stack

DBR structure ($H = 0.5$) has the highest reflectance and the reflectance decreased as the

optical path parameter H deviated from 0.5. However, the peak reflectance was calculated to be higher than 0.99 when $0.35 < H < 0.65$. As a result, the calculated peak reflectance of 20-pairs AlN/GaN DBR structure for sample B could still be kept as high as 0.99.

The micro-photograph images of the grown AlN/GaN DBR structures were observed by the optical microscope and shown in Figure 3-16. Over the whole 2-inch wafer, a crack-free surface was observed on sample surface of sample B. On the other hand, a parallel-crack pattern and a network-crack pattern were observed on sample surface of sample A, and sample C, respectively. The average crack density determined by the micro-photograph images for sample A, B, and C were 15.6/mm, 0/mm, and 26.7/mm. It demonstrated that the generation of crack could be eliminated by controlling the thicknesses of AlN and GaN layers during the growth of AlN/GaN DBR structure, since the crack generation was due to the accumulation of tensile stress in the multiple layer structures.

In order to determine the strain in the DBRs, the XRD measurement on reciprocal space maps (RSM) around the asymmetrical $(10\bar{1}5)$ Bragg peak of the GaN substrate was proceeded. Figure 3-17 (a), (b), and (c) shows the $(10\bar{1}5)$ RSMs of sample A, B, and C, respectively. The lattice parameter c along the growth direction and lattice parameter a along in-plane were represented by the perpendicular axis and the parallel axis, respectively. Both axes were inversely proportional to each lattice constant. The

diffraction pattern around spots labeled A and C are due to the AlN and GaN layers, respectively, and the diffraction pattern around spots labeled B is considered as zero order peak of DBR structure. It can be seen that the location of the diffraction pattern B was shifted to GaN diffraction pattern as the thickness of AlN layers decreasing in DBR structure. Compare with the labeled C of RSM patterns, sample A and B are shown slightly strained GaN embedded between the AlN layers, but sample C is not shown strain within GaN layers. Furthermore, the in-plane strains ε_{xx} in AlN layers can be obtained from $\varepsilon_{xx} = \frac{q_x^{AlN}}{q_x^{epi}} - 1$, where the q_x^{epi} and q_x^{AlN} are the x positions of the actual epitaxy AlN film and unstrained AlN, respectively. The biaxial tensile strain in AlN layer in sample A, B and C were calculated to be 0.00722, 0.00902, and 0.00521, respectively. These results indicate that the AlN layers are under tensile strain and the tensile strain is partially relaxed because the diffraction peaks don't align in a vertical straight line. However, the degree of relaxation decreases as the thickness of AlN layer in DBR structure decreasing.

Indeed, the relaxation of strain energy by generating cracks on sample surface and the relative strain parameter γ_{crack} can be calculated from the density of generated cracks on the sample surface [23]. The calculation results of γ_{crack} for sample A, B, and C were 0.62, 1 (crack-free), and 0.49, respectively. Beside, the relative strain parameters γ determined by the results of x-ray diffraction patterns on the RSMs were 0.36, 0.56, and 0.26 for

sample A, B, and C, respectively. Figure 3-18 shows the strain parameters versus optical length parameter H for sample A, B, and C. The difference between γ_{crack} and γ indicated that there are other mechanisms, such as misfit dislocation and V-trench, to relax the strain energy of AlN/GaN multi-layer structure [24]. The decreasing trends in γ_{crack} versus H indicated that increasing the thickness of AlN layers in AlN/GaN DBR structure could easily lead to strain energy relaxation by generating cracks on the sample surface.

The reflectivity spectra of these DBRs were measured by the n&k ultraviolet-visible spectrometer with a normal incidence measurement setup. The normalized reflectance spectra of AlN/GaN DBR structures for samples of A, B, and C were shown in Figure 3-19. The stopband center of reflectance spectrum of sample A composed of quarterwave stacks DBR structure was 431 nm with a peak reflectance of 96.0% and the stopband width of 27 nm. Sample B has the similar reflectivity peak value of about 96% around 429 nm and the stopband width of 27 nm for the asymmetry AlN/GaN DBR structure. However, the stopband center of reflectance spectrum of sample C is 436 nm with a lower peak reflectance of 90.0% and a smaller stopband width of 20 nm. It may be indicated that the generation of surface cracks due to the strain energy relaxation could lead to increasing fluctuation of the growth rate resulting in the red-shifted of stopband centers [25] and degradation of the peak reflectance and stopband width [3, 26].

In conclusion, the crack-free AlN/GaN DBR structures on (0001) sapphire were

grown by MOCVD. The peak reflectivity of a 20-pair asymmetric AlN/GaN DBR structure was about 96% with a stopband width of 27 nm around the center wavelength of 429 nm. By reducing the ratio of AlN and GaN layer thickness, the density of surface cracks per unit area could be reduced. By this approach, the realization of high quality III-nitride DBRs shall pave the way for development of nitride-based high-Q microcavity and blue VCSELs.



References

- [1] Grant R. Fowles, "Introduction to Modern Optics", Chapter 4, 1975.
- [2] T. Honda, A. Katsube, T. Sakaguchi, F. Koyama, K. Iga, Jpn. J. Appl. Phys. Pt. 1 34, 3527, 1995.
- [3] H.M. Ng, T.D. Moustakas, S.N.G. Chu, Appl. Phys. Lett. 76, 281, 2000.
- [4] R. Singh, D. Doppalapudi, T.D. Moustakas, L.T. Romano, Appl. Phys. Lett. 70, 1089, 1997.
- [5] D. Doppalapudi, S.N. Basu, T.D. Moustakas, J. Appl. Phys. 85, 883, 1999.
- [6] H.M. Ng, T.D. Moustakas, S.N.G. Chu, Appl. Phys. Lett. 76, 2818, 2000.
- [7] D.D. Koleske, A.E. Wickenden, R.L. Henry, J.C. Culbertson, M.E. Twigg, J. Crystal Growth 223, 466, 2001.
- [8] S. Yamaguchi, M. Kosaki, Y. Watanabe, Y. Yukawa, S. Nitta, H. Amano, I. Akasaki, Appl. Phys. Lett. 79, 3062, 2001.
- [9] R. Langer, A. Barski, J. Simon, N.T. Pelekanos, O. Konovalov, R. Andre, Le Si Dang, Appl. Phys. Lett. 74, 3610, 1999.
- [10] S. Fernandez, F.B. Naranjo, F. Calle, M.A. Sanchez-Garcia, E. Calleja, P. Vennegues, A. Trampert, K.H. Ploog, Appl. Phys. Lett. 79, 2136, 2001.
- [11] F. Natali, D. Byrne, A. Dussaigne, N. Grandjean, J. Massies, B. Damilano, Appl. Phys. Lett. 82, 499, 2003.
- [12] T. Someya, Y. Arakawa, Appl. Phys. Lett. 73, 3653, 1998.
- [13] K.E. Waldrip, J. Han, J.J. Figiel, H. Zhou, E. Makarona, A.V. Nurmikko, Appl. Phys. Lett. 78, 3205, 2001.
- [14] H.P.D. Schenk, P. de Mierry, P. Vennegues, O. Tottereau, M. Laugt, M. Vaille, E. Feltin, B. Beaumont, P. Gibart, S. Fernandez, F. Calle, Appl. Phys. Lett. 80, 174, 2002.
- [15] N. Nakada, H. Ishikawa, T. Egawa, and T. Jimbo, Jpn. J. Appl. Phys., Part 2 42, L144,

2003.

[16] J. P. Zhang, H. M. Wang, M. E. Gaevski, C. Q. Chen, Q. Fareed, J. W. Yang, G. Simin, and M. Asif Khan, *Appl. Phys. Lett.* 80, 3542, 2002.

[17] E. Feltin, B. Beaumont, M. Laugt, P. Vennegues, H. Lahreche, M. Leroux, and P. Gibart, *Appl. Phys. Lett.* 79, 3230, 2001.

[18] M. Kurimoto, T. Nakada, Y. Ishihara, M. Shibata, T. Honda, and H. Kawanishi, *Jpn. J. Appl. Phys., Part 2* 38, L552, 1999.

[19] Y. Ishihara, J. Yamamoto, M. Kurimoto, T. Takano, T. Honda, and H. Kawanishi, *Jpn. J. Appl. Phys., Part 2* 38, L1296, 1999.

[20] D.D. Koleske, A.E. Wickenden, R.L. Henry, J.C. Culbertson, M.E. Twigg, *J. Crystal Growth* 223, 466, 2001.

[21] D. Brunner, H. Angerer, E. Bustarret, F. Freudenberg, R. Hopler, R. Dimitrov, O. Ambacher, M. Stutzmann, *J. Appl. Phys.* 82, 5090, 1997.

[22] G. Yu, G. Wang, H. Ishikawa, M. Umeno, T. Soga, T. Egawa, J. Watanabe, T. Jimbo, *Appl. Phys. Lett.* 70, 3209, 1997.

[23] S. Einfeldt, V. Kirchner, H. Heinke, M. Dießelberg, S. Figge, K. Vogeler, and D. Hommel, *J. Appl. Phys.* 88, 7029, 2000.

[24] P. Vennéguès, Z. Bougrioua, J. M. Bethoux, M. Azize, and O. Tottereau, *J. Appl. Phys.* 97, 024912, 2005.

[25] J.-M. Wagner and F. Bechstedt, *Phy. Rev. B.* 66, 125202, 2002.

[26] N. Naoyuki, I. Hiroyasu, E. Takashi and J. Takashi, *Jpn. J. Appl. Phys.* 42 (2003) L144.

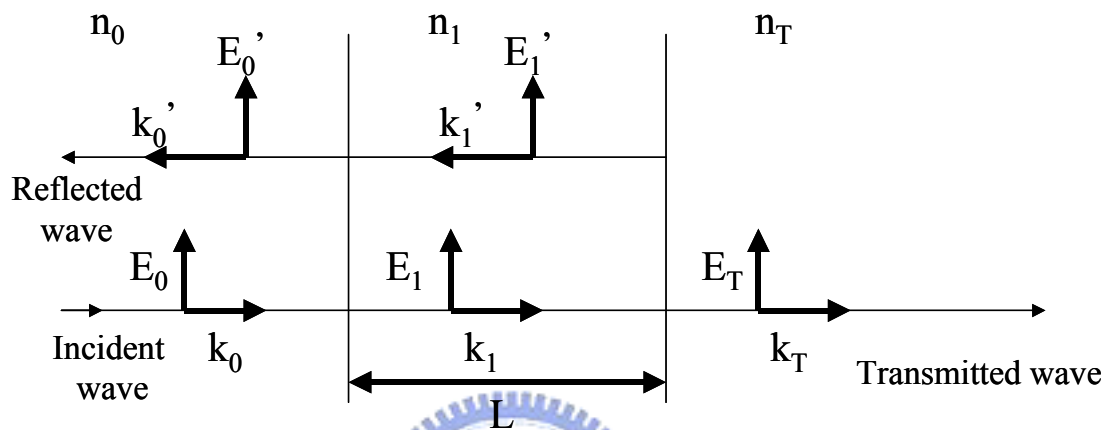


Figure 3-1 The schematic diagram of normal incidence on a single dielectric layer.

Table 3-1 The boundary conditions of electric and magnetic fields at each interface

First Interface	Second Interface
Electric: $E_0 + E_0' = E_1 + E_1'$	$E_1 e^{ikt} + E_1' e^{-ikt} = E_T$
Magnetic: $H_0 - H_0' = H_1 - H_1'$	$H_1 e^{ikt} - H_1' e^{-ikt} = H_T$
or $n_0 E_0 - n_0 E_0' = n_1 E_1 - n_1 E_1'$	$n_1 E_1 e^{ikt} - n_1 E_1' e^{-ikt} = n_T E_T$



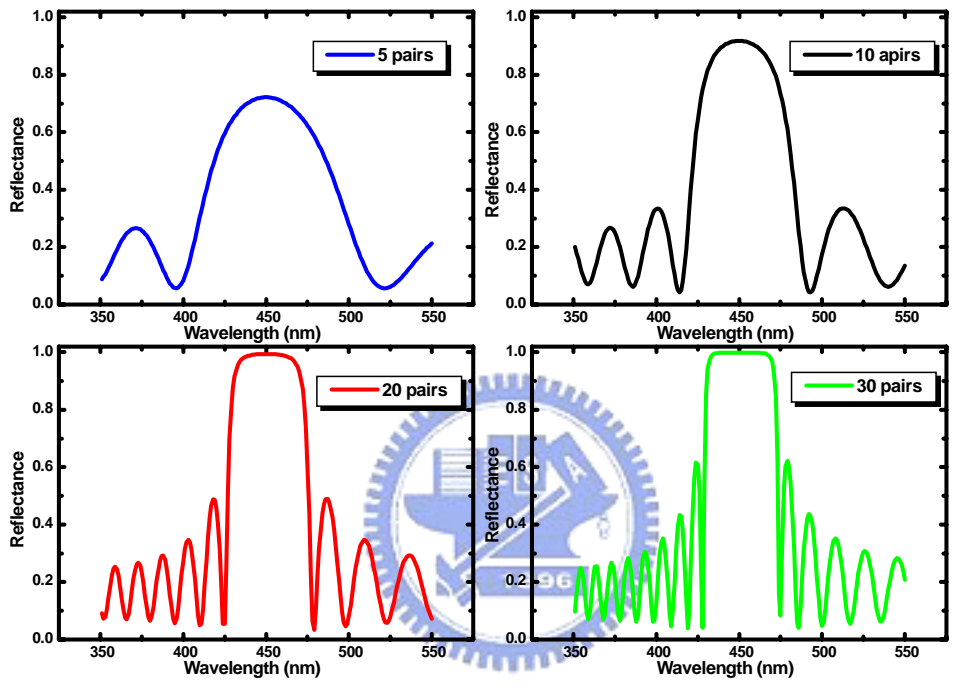


Figure 3-2 The simulation results for DBR structures with 5, 10, 20, and 30 pairs. The refractive indices of n_H and n_L are set as 2.4, and 2.1, respectively.

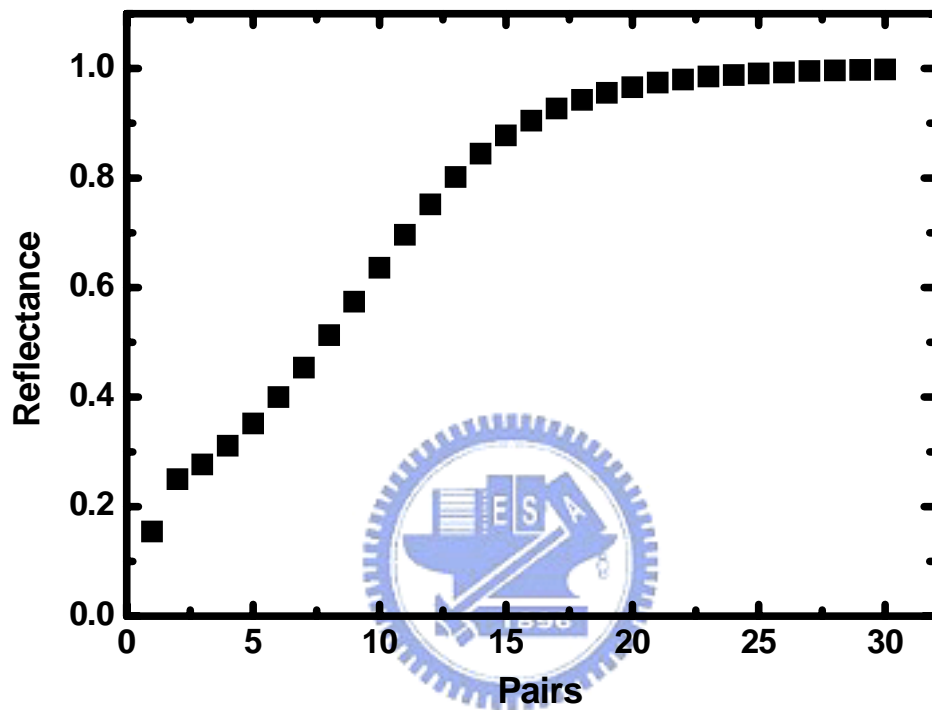


Figure 3-3 The peak reflectance of DBR structures with different pair number.

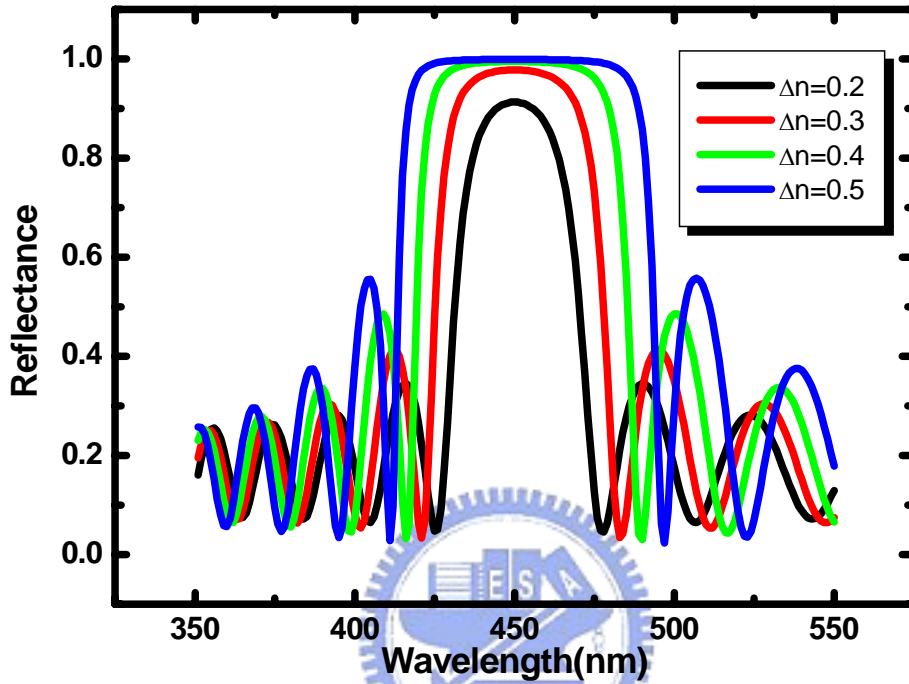
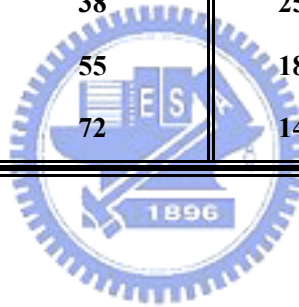


Figure 3-4 The simulation results for 20-pair DBR structures with $\Delta n=0.2$, 0.3, 0.4, and 0.5, respectively.

Table 3-2 The arrangement of simulation result of DBR structure with different index contrast.

15-pair DBR Structure			99% DBR Structure	
Δn	Peak Reflectance (%)	StopBand Width (nm)	Needed Pairs	StopBand Width (nm)
0.2	91.3	24	38	25
0.3	97.8	38	25	41
0.4	99.5	55	18	56
0.5	99.9	72	14	73



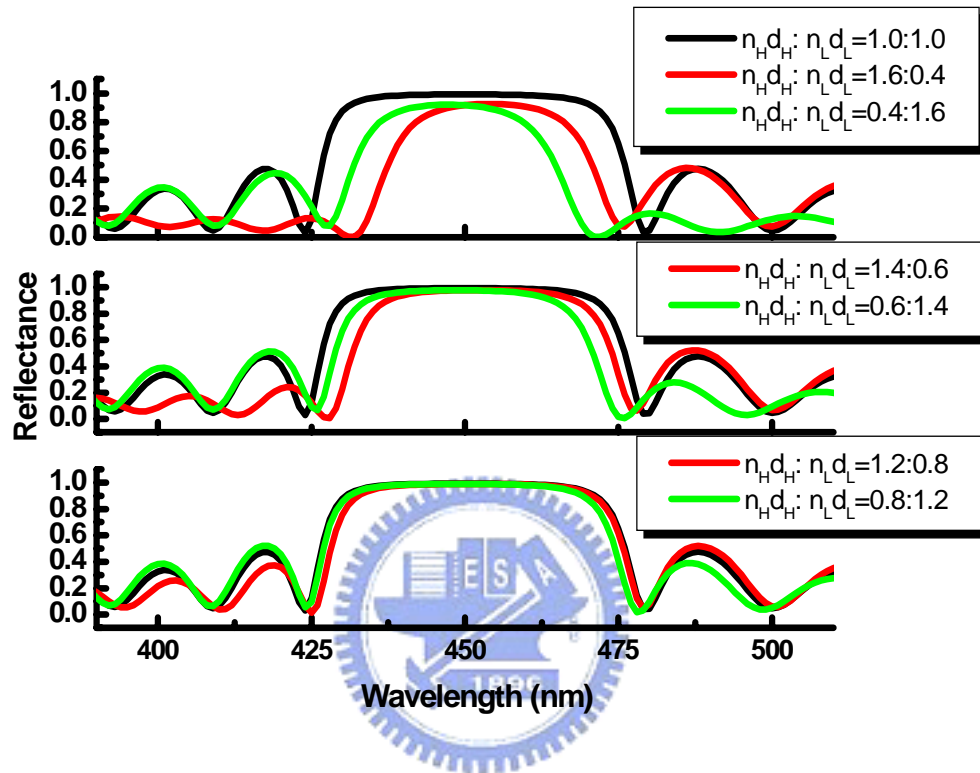


Figure 3-5 The simulation result of asymmetric DBR structure.

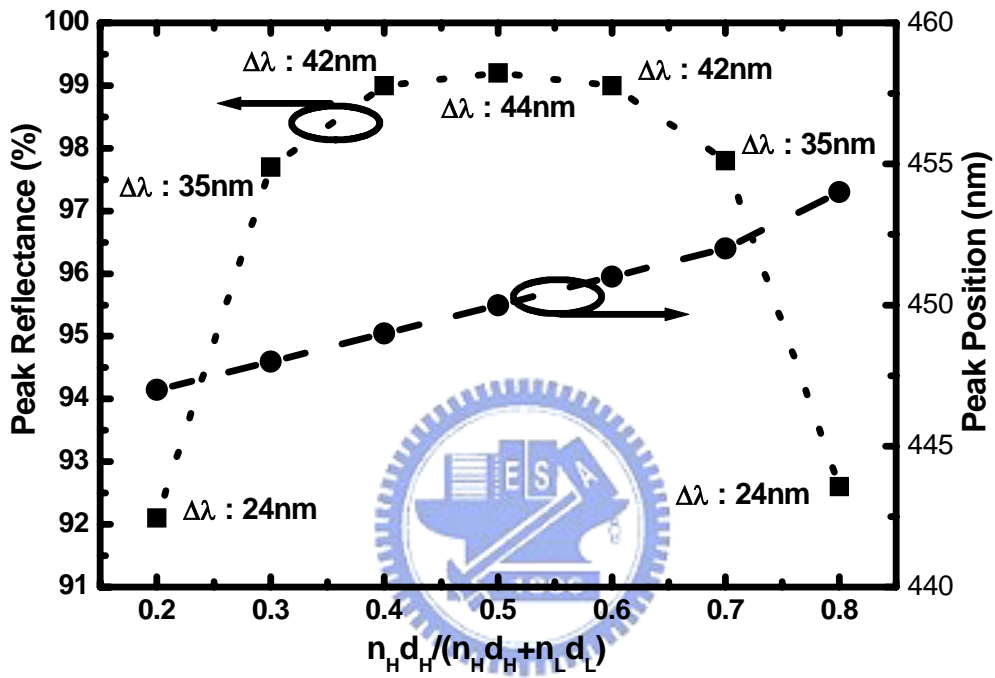


Figure 3-6 The arrangement of peak reflectance and stopband width for different thickness ratio between these two composed materials of 20-pair DBR structure.

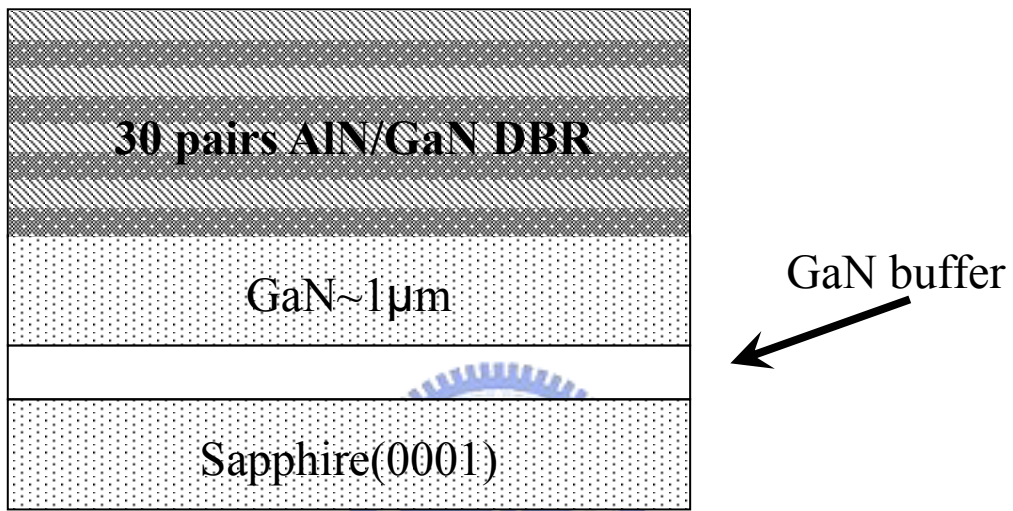


Figure 3-7 The schematic structure of a 30-pair AlN/GaN DBR.

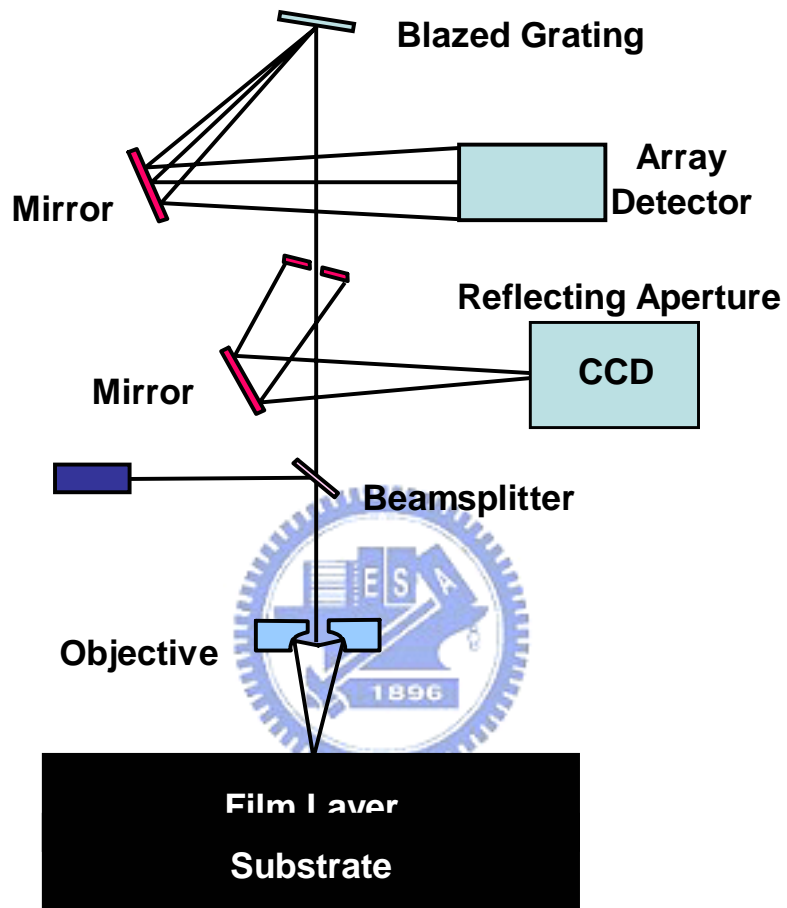


Figure 3-8 The schematic of the reflectance measurement setup with normal incidence at room temperature.

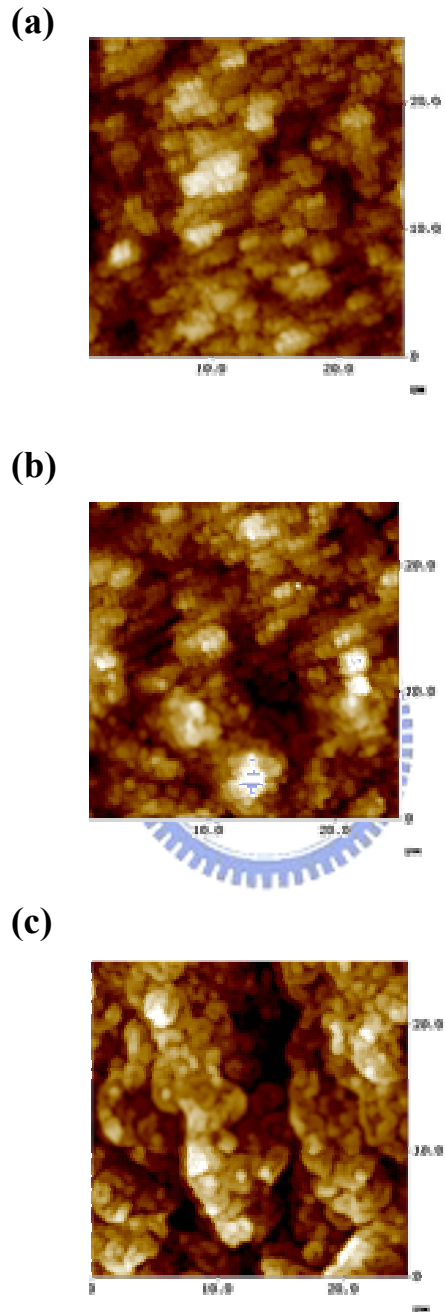


Figure 3-9 The AFM surface morphologies of AlN/GaN DBR structure grown under (a) N_2 , (b) H_2+N_2 , and (c) H_2 ambient gas.

Table 3-3 The arrangement of surface morphologies of DBR structure grown under different ambient gases.

	surface roughness Ra (nm)	grain size (μm)	H2 component
Sample A	8	2	0%
Sample B	10	5	35%
Sample C	12	10	100%

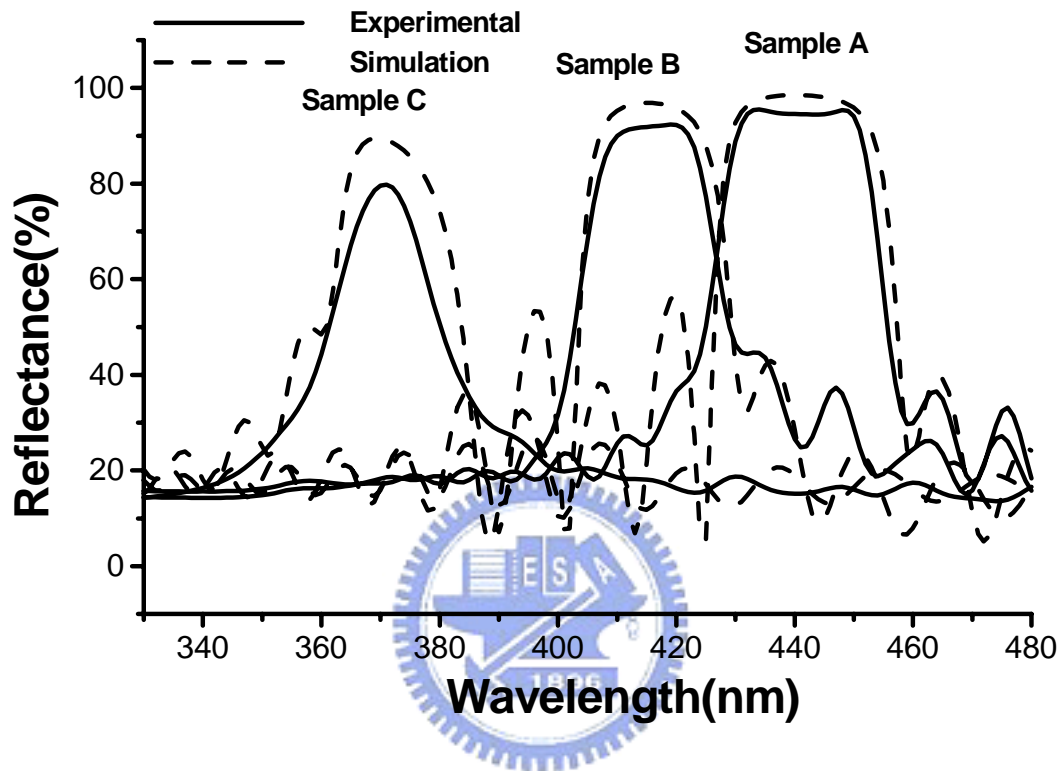


Figure 3-10 Experimental optical reflectance spectra of three 30-pair AlN/GaN DBR (solid lines) and numerical simulations of the optical reflectance spectra (dash lines).

Table 3-4 Comparison of the experimental and simulated peak reflectance values of these three 30-pair AlN/GaN distributed Bragg reflectors

	Experimental (%)		Simulation (%)	
	Peak reflectance (%)	Center wavelength (nm)	Peak reflectance (%)	Center wavelength (nm)
Sample A	94.5	442	98.5	440
Sample B	92.0	418	96.9	415
Sample C	79.9	371	89.5	369



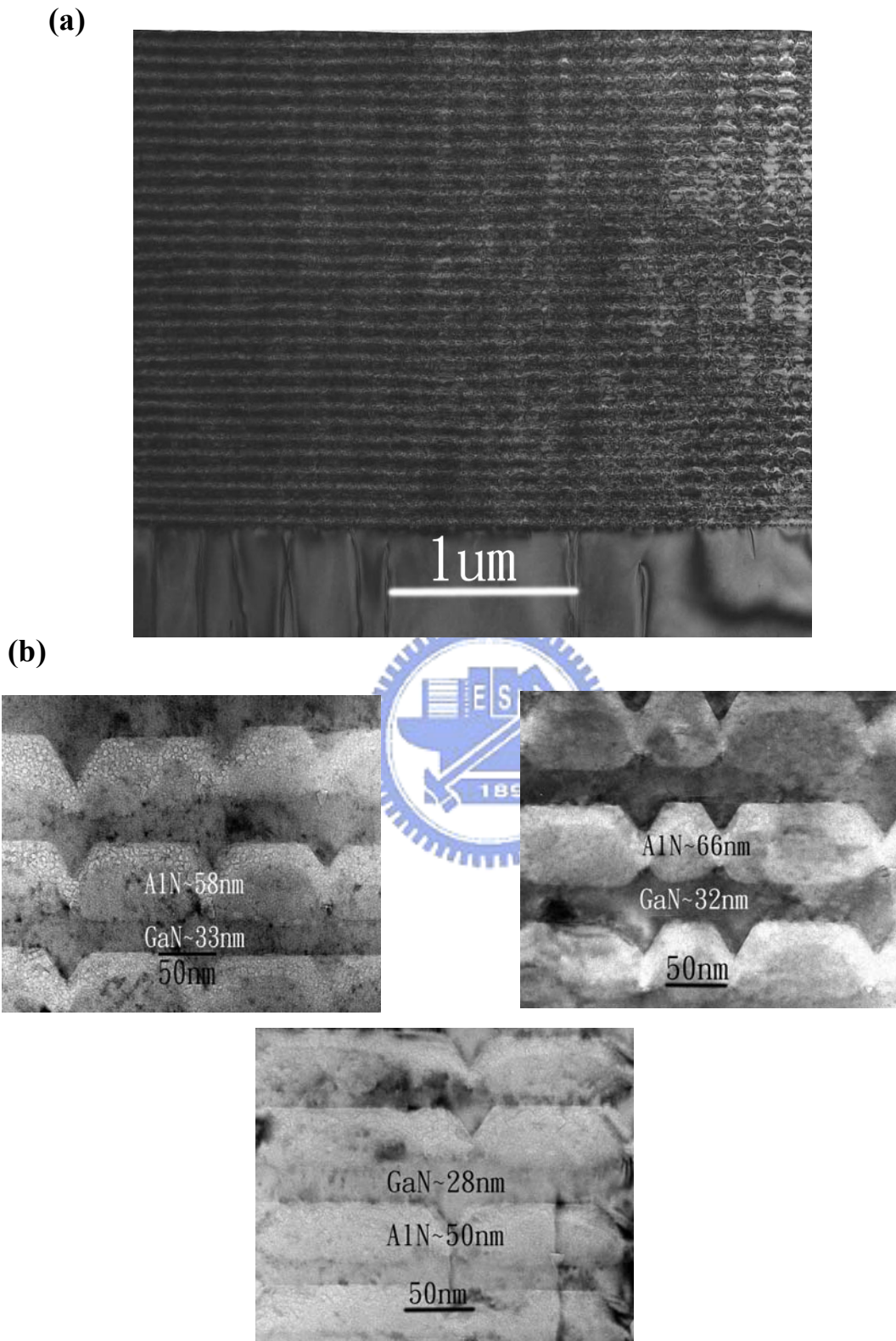


Figure 3-11 (a) Cross-sectional TEM image of sample A. The darker layers are GaN while the lighter layers are AlN. (b) the layer images for sample A, B, and C.

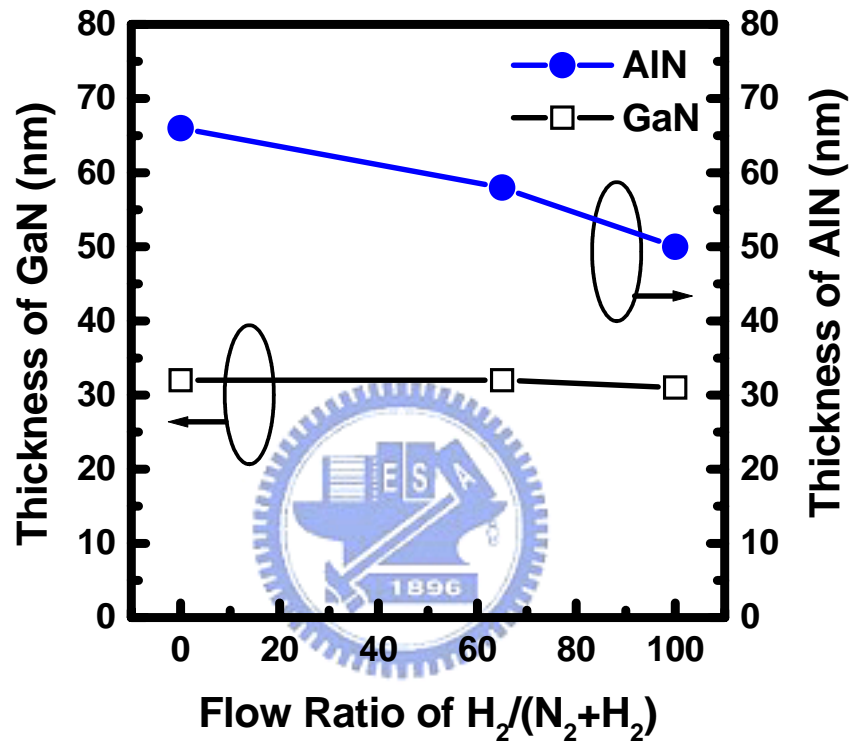


Figure 3-12 The arrangement of thickness of AlN and GaN layers in these three DBR samples.

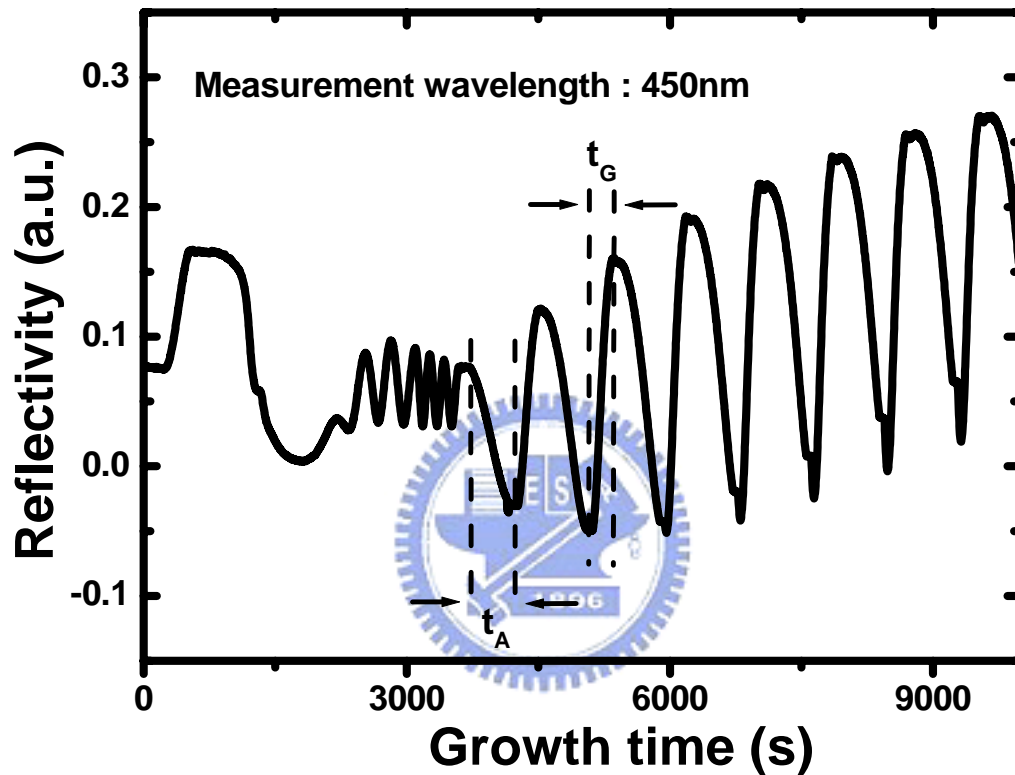


Figure 3-13 In situ normal reflectance measurement during the growth of the Bragg mirror by a fixed measurement wavelength of 450nm. The growth time t_A was set as the AlN layer started at a reflectivity maximum, and ended at the following minimum. The growth time t_G was set as the alternating GaN layer started at a reflectivity minimum, and ended at the following maximum.

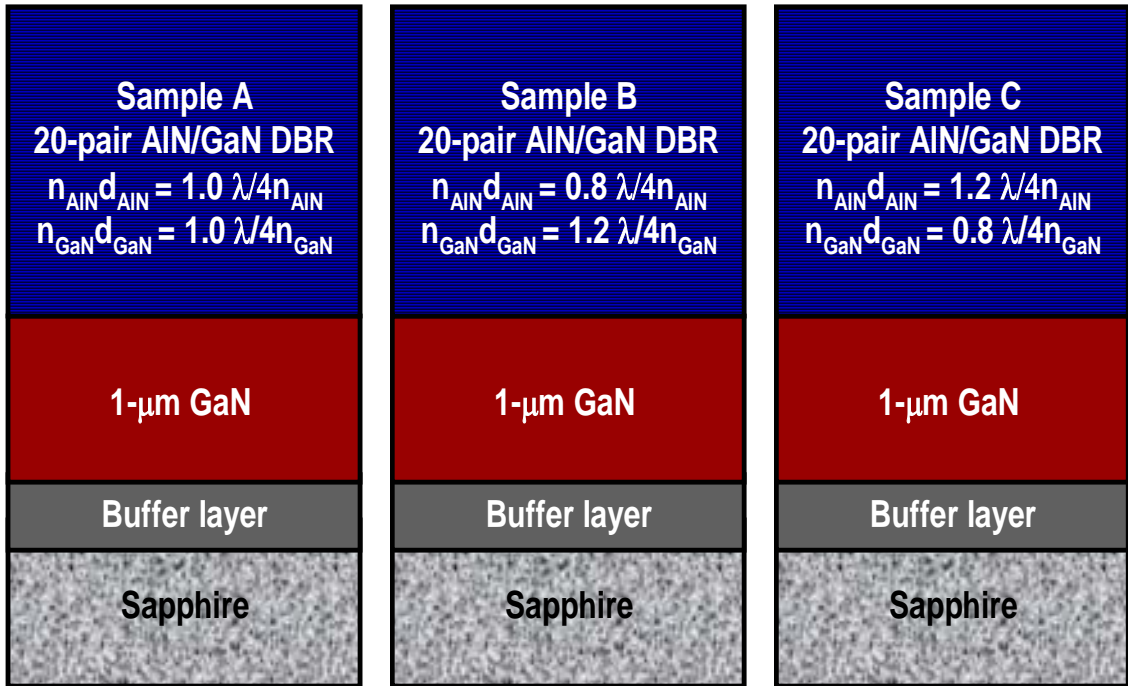


Figure 3-14 The schematic of three AlN/GaN DBR structures composed with different thickness ratios.

Table 3-5 The necessary parameters to calculate strain energy in AlN/GaN DBR structures.

	a (Å)	$C_{11}+C_{12}$	C_{13}	C_{33}	n
AlN	3.126	538	113	370	2.11
GaN	3.201	515	104	414	2.45

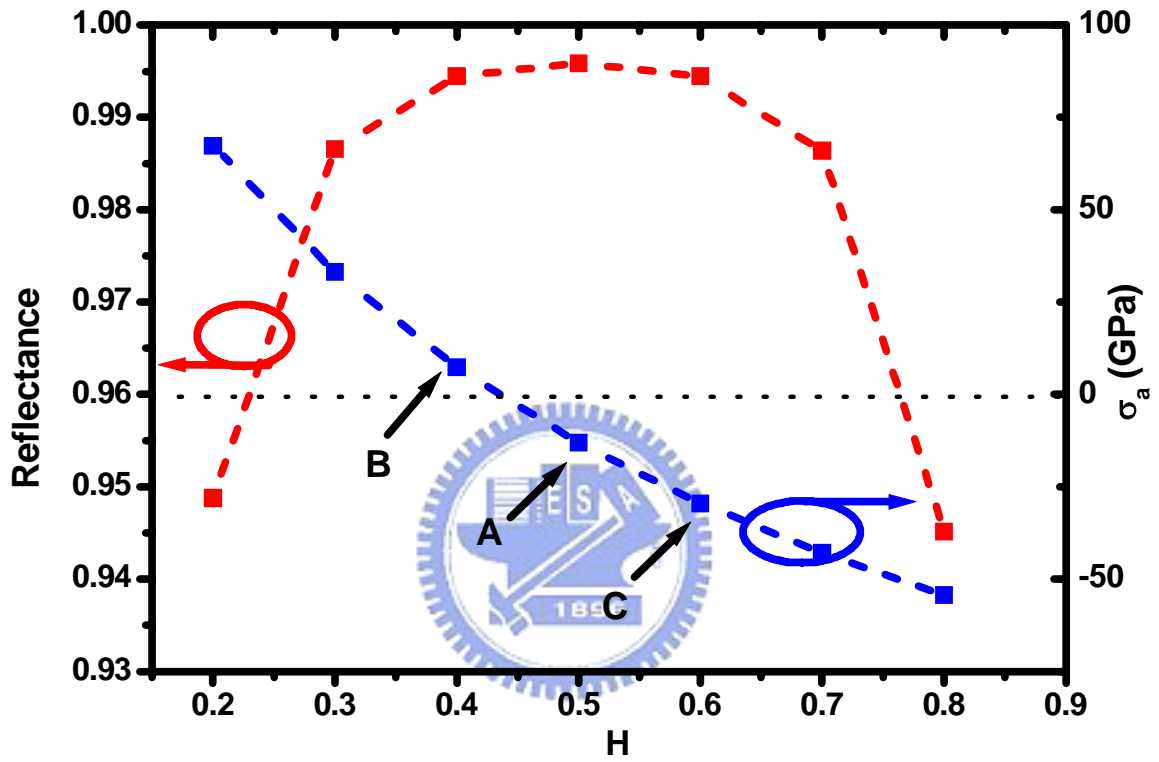


Figure 3-15 Calculation result of average in-plane stress and peak reflectance of 20-pair AlN/GaN DBR structure under different optical length parameter H

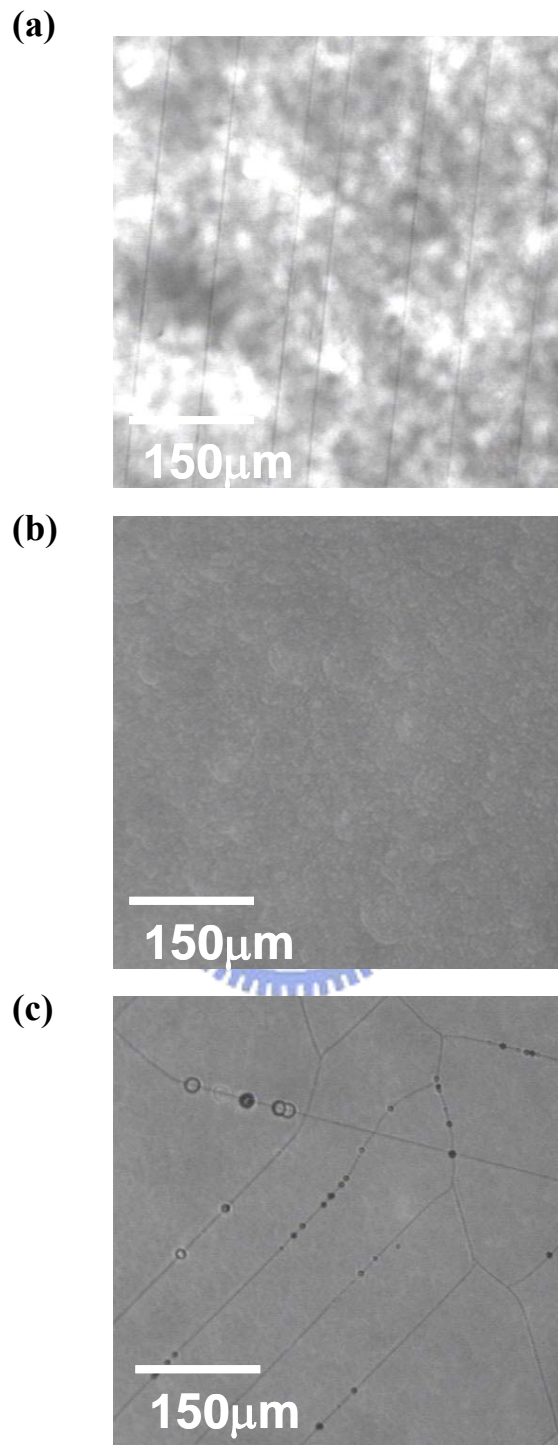
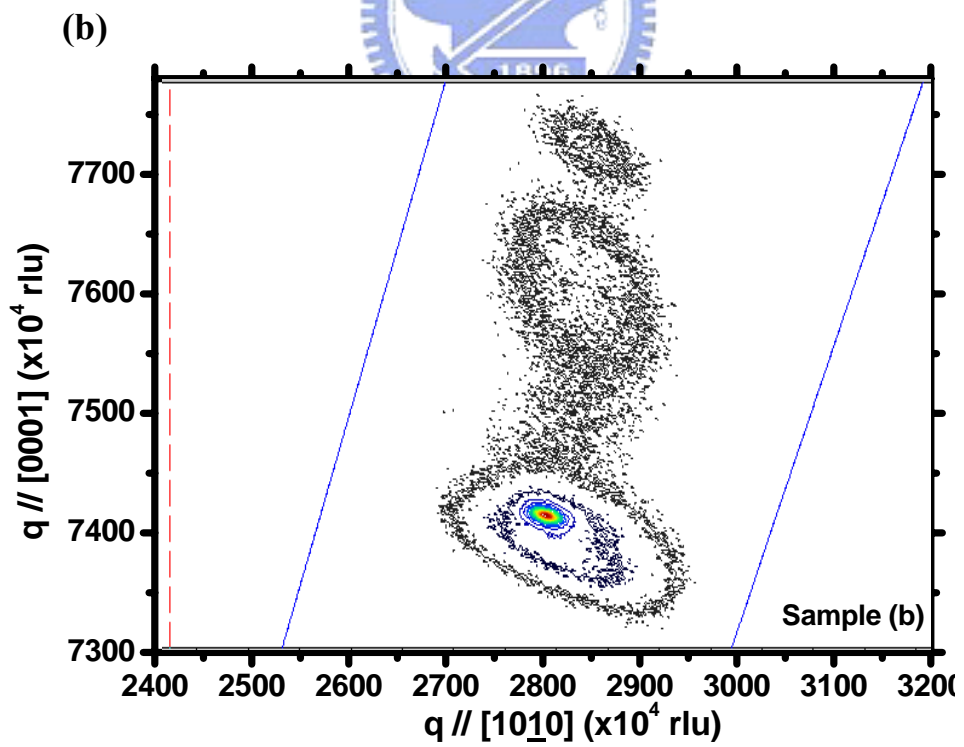
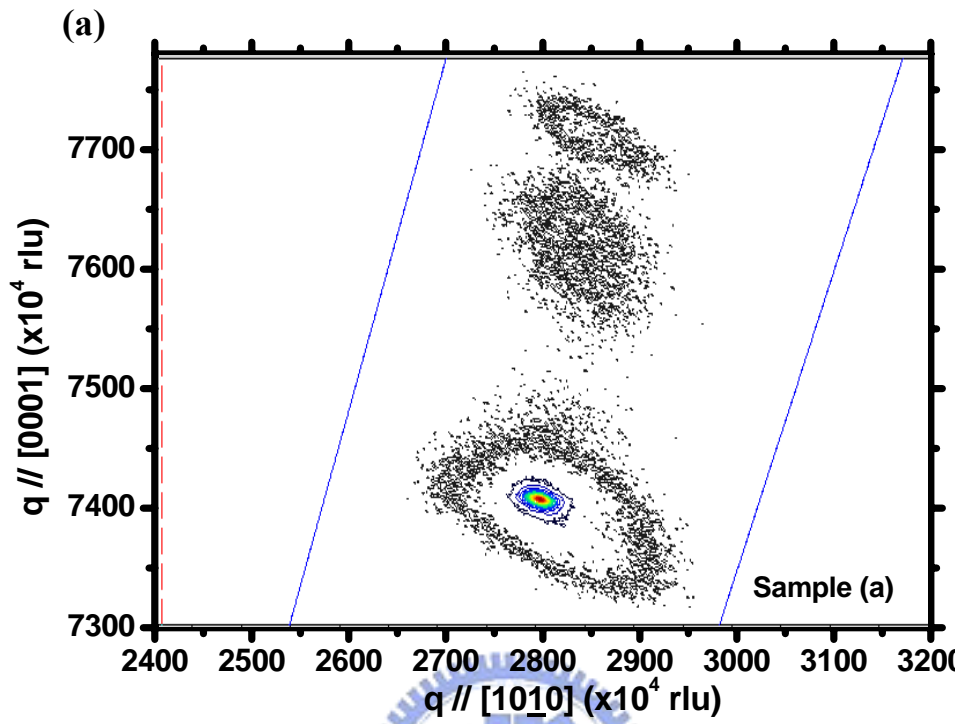


Figure 3-16 Microphotograph images of (a) Sample A, (b) Sample B, and (c) Sample C.



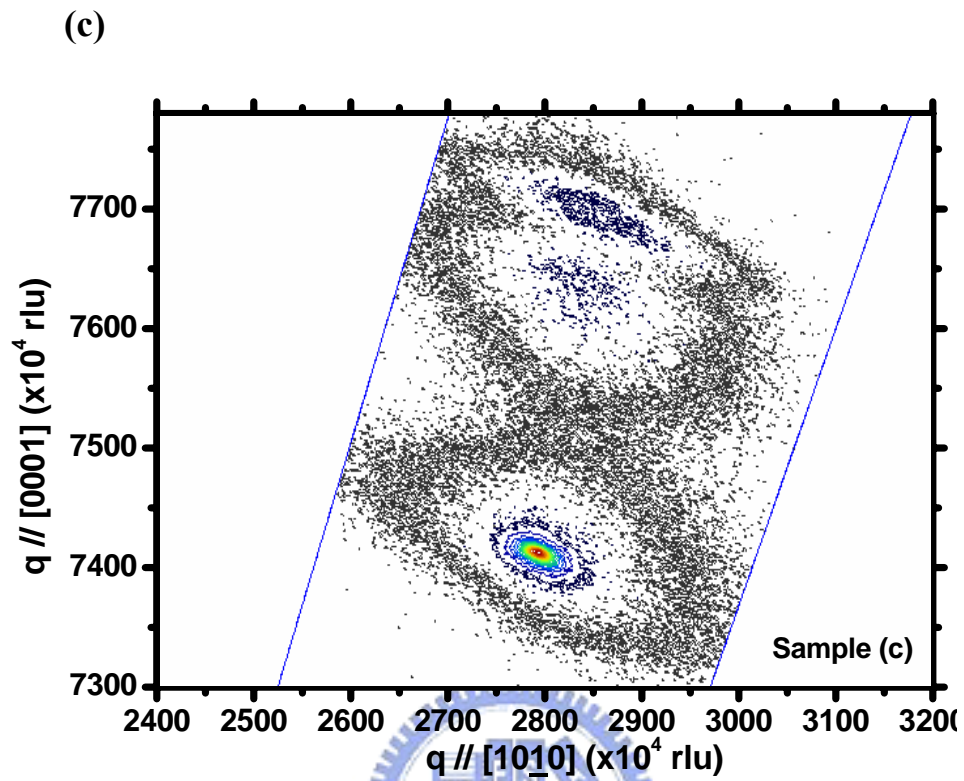


Figure 3-17 X-ray reciprocal space maps of the 20-pairs of AlN/GaN DBR around $(10\bar{1}5)$ of (a) sample A, (b) sample B, and (c) sample C

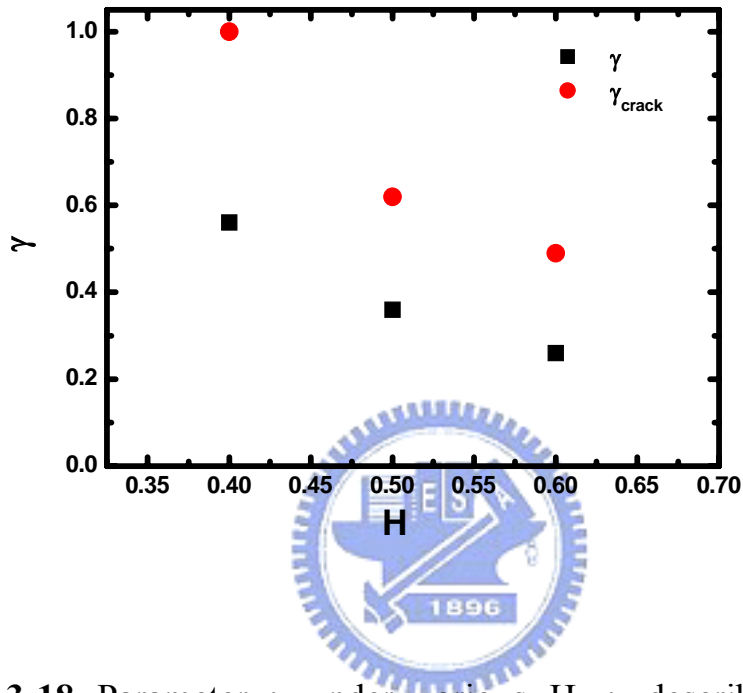


Figure 3-18 Parameter γ under various H. γ described the strain energy remained in whole AlN/GaN DBR structure and was determined by XRD. γ_{crack} described the strain energy remained after generating crack and was calculated from crack density on sample surface.

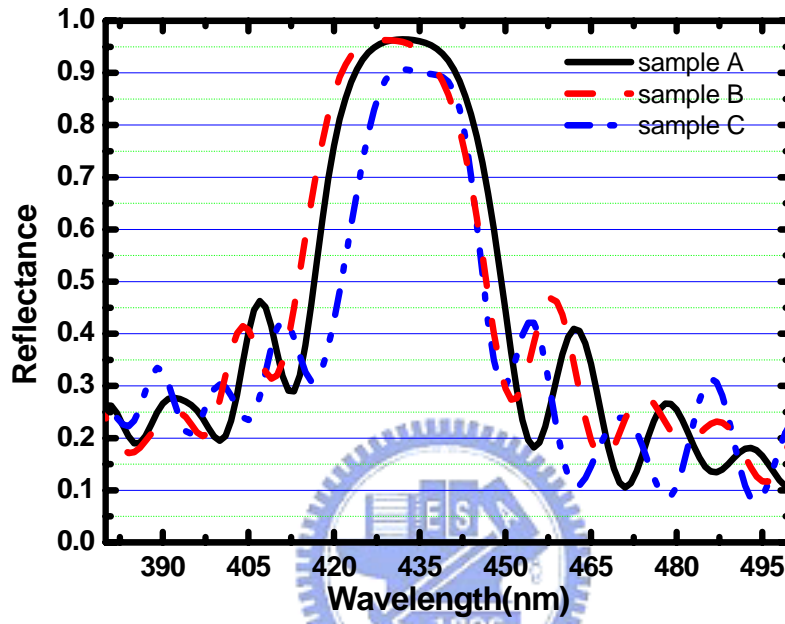


Figure 3-19 Reflectance spectra of the 20-pair AlN/GaN DBR structures measured with normal incidence at room temperature.



Chapter 4

Characteristic of Nitride-Based Microcavity Structure

Chapter 4 reports the characteristic of nitride-based microcavity structure which is composed of a nitride-based cavity space major included an active layer. The feasibility of the AlN/GaN DBR has been discussed in previous chapter, and then we fabricated a hybrid DBR resonator which is composed one AlN/GaN DBR as bottom mirror and one dielectric oxide DBR structure as top mirror. The feasibility of this nitride-based microcavity structure is examined by the performance of optical pumped. Following, the electrically driven device has been fabricated and the characteristics of these devices will be discussed.

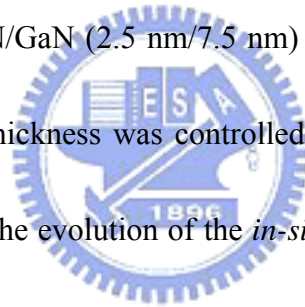


4-1 Fabrication Process of Nitride-Based Microcavity Composed of Hybrid DBR Resonator

In this section, we report the process of fabrication of GaN-based microcavity using the AlN/GaN DBR as the bottom mirror and a dielectric multiple layer structure as the top DBR mirror.

The structure of the GaN-based microcavity was grown in the EMCORE D-75 MOCVD system. The polished optical-grade C-face (0001) 2-inch diameter sapphire was used as substrate for the epitaxial growth of the GaN-based microcavity structure.

Trimethylindium, trimethylgallium, trimethylaluminum, and ammonia were used as the In, Ga, Al, and N sources, respectively. Initially, a thermal cleaning process was carried out at 1080°C for 10 min in a stream of hydrogen ambient before the growth of epitaxial layers. After depositing a 30-nm-thick GaN nucleation layer at 530 °C, the temperature was raised up to 1045°C for the growth of a 1- μ m-thick GaN buffer layer. Then a 25 pairs AlN/GaN DBR structure was grown at 1040°C under the fixed chamber pressure of 100 torr similar to the growth conditions reported at chapter 3. Then a 3 λ -cavity was grown on the 25-pair AlN/GaN DBR structure. The 3 λ -cavity was composed of an n-type GaN layer, a 10-pair In_{0.2}Ga_{0.8}N/GaN (2.5 nm/7.5 nm) multiple quantum well (MQW), and a p-type GaN. The cavity thickness was controlled by the *in-situ* reflectance monitoring, and Figure 4-1 illustrates the evolution of the *in-situ* reflectivity during the growth of the nitride-based microcavity structure. The characteristic of the 3 λ nitride-based cavity was performance by x-ray diffraction and photoluminescence (PL) system with a He-Cd laser as the pumping source. In the DCX-ray rocking curve, shown in Figure 4-2, the GaN peak, the InGaN peak, and satellite peaks are clearly observed, which shows the good quality of the GaN/InGaN interfaces and calculated the GaN/InGaN MQW properties with an average In content and pair thickness as 5 % and 10.0nm. Figure 4-3 shows the PL measurement results. The PL peak of the InGaN/GaN MQW LED was located at 450.3 nm with a 15 nm linewidth. The small oscillations caused by optical interference



effects indicated that the smooth surface and uniform interfaces of the InGaN/GaN MQW-LED structures. From the DC X-ray and PL results, the 10-pair InGaN/GaN MQW structure is a high-quality blue emitter and suitable to test the characteristic of nitride-based microcavity structure.

After the sample was grown, an 8-pair Ta₂O₅/SiO₂ dielectric mirror was deposited by the E-gun as the top DBR reflector. The schematic diagram and the scanning electron microscopy (SEM) image of the overall GaN-based microcavity structure are shown in Figures 4-4(a) and 4-4(b). During these processes, the reflectivity spectrum of the AlN/GaN DBR structure and the Ta₂O₅/SiO₂ dielectric mirror were measured by the n&k ultraviolet-visible spectrometer with normal incidence at room temperature. Figure 4-5 shows the reflectivity spectrum of AlN/GaN DBR and Ta₂O₅/SiO₂ DBR, respectively. The peak reflectance of the top and bottom DBR was 97.5% and 94% at 450 nm, respectively.

4-2 Characteristics of Optically Pumped Blue GaN-Based Microcavity Structure

In this section, we report the characteristics of the nitride-based microcavity by performing optical pumping at room temperature, and a laser operation with a stimulated emission has been measured.

The emission spectrum of the nitride-based microcavity structure was all measured

using a microscopy system (WITec, alpha snom) at room temperature. The PL emission was excited by the 325 nm He–Cd laser with a spot size of about 10- μm -diameter. The optical pumping of the sample was performed using a frequency-tripled Nd:yttrium–vanadium–oxygen₄ 355 nm pulsed laser with a pulse width of ~ 0.5 ns at a repetition rate of 1 kHz. The pumping laser beam with a spot size of 60 μm was incident normal to the surface of nitride-based microcavity structure. The light emission from the VCSEL sample was collected using an imaging optic into a spectrometer charge couple device (Jobin-Yvon Triax 320 Spectrometer) with a spectral resolution of ~ 0.1 nm for spectral output measurement. The schematic diagram of optical pumping system is shown

in Figure 4-6.

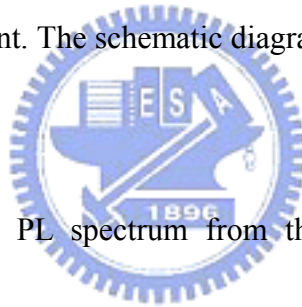


Figure 4-7 shows the PL spectrum from the nitride-based microcavity at room temperature. A narrow emission peak with full width at half maximum of 1.4 nm corresponding to the cavity resonant mode at 448 nm was observed. It indicates the emission peak was well aligned with vertical cavity formed by the high reflectance of AlN/GaN DBR and the Ta₂O₅/SiO₂ dielectric mirror. The cavity quality factor estimated from the emission linewidth of 1.4 nm is about 320. This value agrees with the nitride-based microcavity cavity formed by AlN/GaN DBR and Ta₂O₅/SiO₂ DBR. Figure 4-8 shows the variation of emission spectrum with the increasing pumping energy. A dominant laser emission line at 448 nm appears under a high pumping energy. The laser

emission spectral linewidth reduces with the pumping energy above the threshold energy and approaches 0.25 nm at the pumping energy of 3.8 μJ per pulse. The light emission intensity from the nitride-based microcavity as a function of the pumping energy is shown in Fig. 4-9. A distinct non-linear and threshold characteristic was observed at the threshold pumping energy (E_{th}) of about 1.5 μJ per pulse corresponding to an energy density of 53 mJ/cm^2 . Then the laser output linearly increased with the pumping energy beyond the threshold. The carrier density at the threshold is estimated to be about $3 \times 10^{20} \text{ cm}^{-3}$, assuming the reflectivity of the top mirror at pumping wavelength of 355 nm was 40%, the absorption coefficient of the GaN was about 10^5 cm^{-1} at 355 nm and the quantum efficiency was 10%. We estimated the threshold gain (g_{th}) of our nitride-based microcavity cavity using the equation [1, 2]

$$g_{\text{th}} = (1/2N_w L_w) \ln(1/R_1 R_2) \quad (4-1)$$

where N_w is the number of quantum wells, L_w is the width of each quantum well and R_1 , R_2 are the reflectivity of the top and bottom mirrors, respectively. We obtained the required threshold gain is about $1.45 \times 10^4 \text{ cm}^{-1}$. The parameters used in the estimations of carrier density at threshold and threshold gain are listed in the Table 4-1 [2, 3].

In conclusion, a nitride-based microcavity with hybrid DBR mirrors, consisting of AlN/GaN DBR and Ta₂O₅/SiO₂ was fabricated. The laser action was achieved under the optical pumping at room temperature with a threshold pumping energy density of about

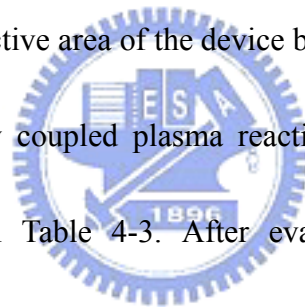
53 mJ/cm². The nitride-based microcavity emits 448 nm with a linewidth of 0.25 nm.

4-3 Fabrication Process of Nitride-Based Microcavity Light Emitting Device

In this section, we report the procedures of the fabrication nitride-based microcavity light emitting device (MCLED). An intra-cavity contacted device has been fabricated to avoid the current through the oxide DBR structure, and a transparent contact layer was used to resolve the problem of lateral hole current spreading which is a major challenge in nitride vertical cavity structure.

The blue nitride-based MCLEDs were composed of a 25 pairs AlN/GaN DBR, nitride-based 3λ -cavity which included an n-type GaN, a 10-pair InGaN/GaN MQW, a p-type GaN, and a 2-pair SiO₂/TiO₂ DBR structure. The PL and X-ray spectra of the 3λ nitride-based cavity structure were measured. In Fig. 4-10, The PL peak of the InGaN/GaN MQW LED was located at 410.2nm with an 18 nm line width, and the DCX-ray rocking curve, shown in Figure 4-11, the GaN peak, the InGaN peak, and one satellite peak are clearly observed, which shows the good quality of the GaN/InGaN interfaces and calculated the GaN/InGaN MQW properties with an average In content and pair thickness as 6% and 8.67nm. The reflectance spectra of the 2-pair TiO₂/SiO₂ DBR and the 20-pair AlN/GaN bottom DBR were measured and shown in Figure 4-12. The EL spectrum of the full MCLED structure is also shown in Figure 4-12. It indicates

the emission peak was well aligned with vertical cavity formed by the high reflectance of AlN/GaN DBR and the TiO₂/SiO₂ dielectric mirror and a narrow emission peak with full width at half maximum of 7.4 nm corresponding to the cavity resonant mode at 410.6 nm was observed. Before the process, the wafer should be cleaned. The initial clean procedures are shown in Table 4-2. For fabrication of nitride-based MCLED, the schematics of the fabrication steps which involves mesa defined, SiO₂ passivated as the current confinement layer, Ti/Al n-contact metal, transparent contact layer (TCL), Ni/Au p-contact metal, and dielectric TiO₂/SiO₂ DBR deposited are shown in Figure 4-13. The first step is to define the active area of the device by coating photo-resist (P.R) and to etch the p-GaN by inductively coupled plasma reactive ion etching (ICP/RIE). The detail procedures are shown in Table 4-3. After evaporating 150Å titanium and 2200Å Aluminum as the n-type contact, a 3000 Å SiO₂ passivated as the current confinement layer with the effective optical aperture was deposited by plasma enhanced chemical vapor deposition (PECVD). After the SiO₂ depositing, a circular pattern was defined by photo-lithography technology, and then the SiO₂ layer was etched by BOE. A TCL and a p-type contact were followed evaporated in the aperture. In the end, the MCLED was completed by capping the structure with 2-pair SiO₂/TiO₂ DBR structure. The schematic diagram and the SEM image of the top-view MCLED are shown in Figure 4-14.



4-4 Characteristics of stable emission nitride-based microcavity light-emitting devices

In this section, the performance of electrically driven the GaN-based microcavity light emitting devices (MCLEDs) is discussed. The stability, localization, and higher output power of the electroluminescence are discussed in detail for this vertical resonance cavity.

The MCLED was driven at room temperature by a continue current power supply (Modle-238, Keithley) controlled by a computer system. The spectrum of electro lumiance from the MCLED was collected using a microscopy system (WITec, alpha snom), and analyzed by a spectrometer charge couple device (Jobin-Yvon Trix 320 Spectrometer) with a spectral resolution of about 1nm. The detailed setup of the measured system was shown in Figure 4-15.

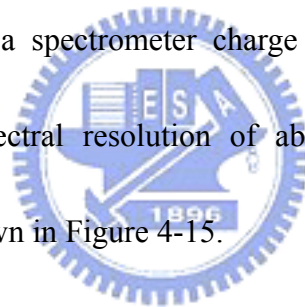


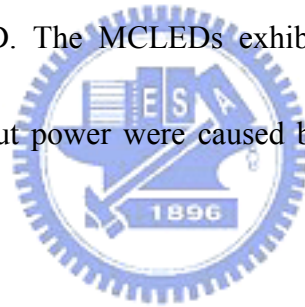
Figure 4-16 shows the top view of light emission photograph of the MCLED at 20mA current injection, and the photograph shows that the current is confined in the aperture area. Figure 4-17(a) shows the I-V characteristics for the nitride-based MCLED, the turn-on voltage is 3.8 V, and the resistance is about 650 Ω . Compared with the I-V characteristics of commercial nitride-based LED show in Figure 4-17(b), the higher turn-on voltage and resistance may be caused by the small aperture and thinner n-type GaN layer. The output power as a function of injection current density is shown in Fig. 4-18. Compared the output powers at 600 A/cm² injection current density, the intensity of

the MCLED was three times higher than the MCLED without top TiO₂/SiO₂ DBR layers. This output power increase was caused by the vertical resonant cavity effect and the directional light emission [5].

Figure 4-19 was the EL emission spectrum of MCLED. The typical EL emission peak without top DBR structure was located at 407.3 nm, and the peak of EL spectrum will be shift to 410 nm and coincide with the high reflectivity region of the top TiO₂/SiO₂ and the bottom AlN/GaN DBR structure. The line-width of the EL emission peak narrowed from 12.5 nm (with bottom AlN/GaN DBR) to 7.4 nm (with top TiO₂/SiO₂ and bottom AlN/GaN DBR). Because of the optical confinement of top and bottom DBR structures, the EL emission peak was fixed in this optical vertical cavity structure. The line-width narrowing and emission peak localization were caused by the resonance effect in this vertical cavity structure. The EL emission wavelength as a function of injection current density is shown in Fig. 4-20. The EL emission peak of a MCLED without top TiO₂/SiO₂ DBR layers has a stronger red shift of 0.48 nm/kA/cm² due to the thermal heating effect at a higher current density. A red shift of only 0.12 nm/kA/cm² is measured in the full MCLED device by varying the injection current. This stability of the EL wavelength was caused by the cavity effect with the resonant Fabry-Perot cavity.

In conclusion, 3λ GaN-based MCLED structures were grown by MOCVD. In MCLED structures, the 3λ InGaN/GaN MQW resonant cavities have been grown

between the top TiO₂/SiO₂ DBR and the bottom AlN/GaN DBR stack. For measuring the EL spectrum from the top surface issue, a lower reflectivity top TiO₂/SiO₂ DBR (81.7%) was deposited on the aperture region with a 300μm² area and the bottom AlN/GaN DBR has a higher reflectivity of 90.4%. From the EL measurement of the MCLED, the emission peak localization at 410 nm with a narrow line-width of 7.4 nm, and the output power was enhanced and three times the measure of the device without top DBR at the 600 A/cm² injection current density. A stable emission wavelength as varying the injecting current density with a low red-shift of 0.12 nm/kA/cm² was also measured in our nitride-based MCLED. The MCLEDs exhibit much less red shift with injection current and a higher output power were caused by the resonance effect in this vertical cavity structure.



References

- [1] T. Someya, R. Werner, A. Forchel, M. Catalano, R. Cingolani, and Y. Arakawa, *Science* 285, 1905, 1999.
- [2] T. Tawara, H. Gotoh, T. Akasaka, N. Kobayashi, and T. Saitoh, *Appl. Phys. Lett.* 83, 830, 2003.
- [3] G. Yu, G. Wang, H. Ishikawa, M. Umeno, T. Soga, T. Egawa, J. Watanabe, and T. Jimbo, *Appl. Phys. Lett.* 70, 3209, 1997.
- [4] Carl W. Wilmsen, Henryk Temkin, and Larry A. Coldren, “Vertical-Cavity Surface-Emitting Laser Design, Fabrication, Characterization, and Applications”, Chapter 3, 1999.



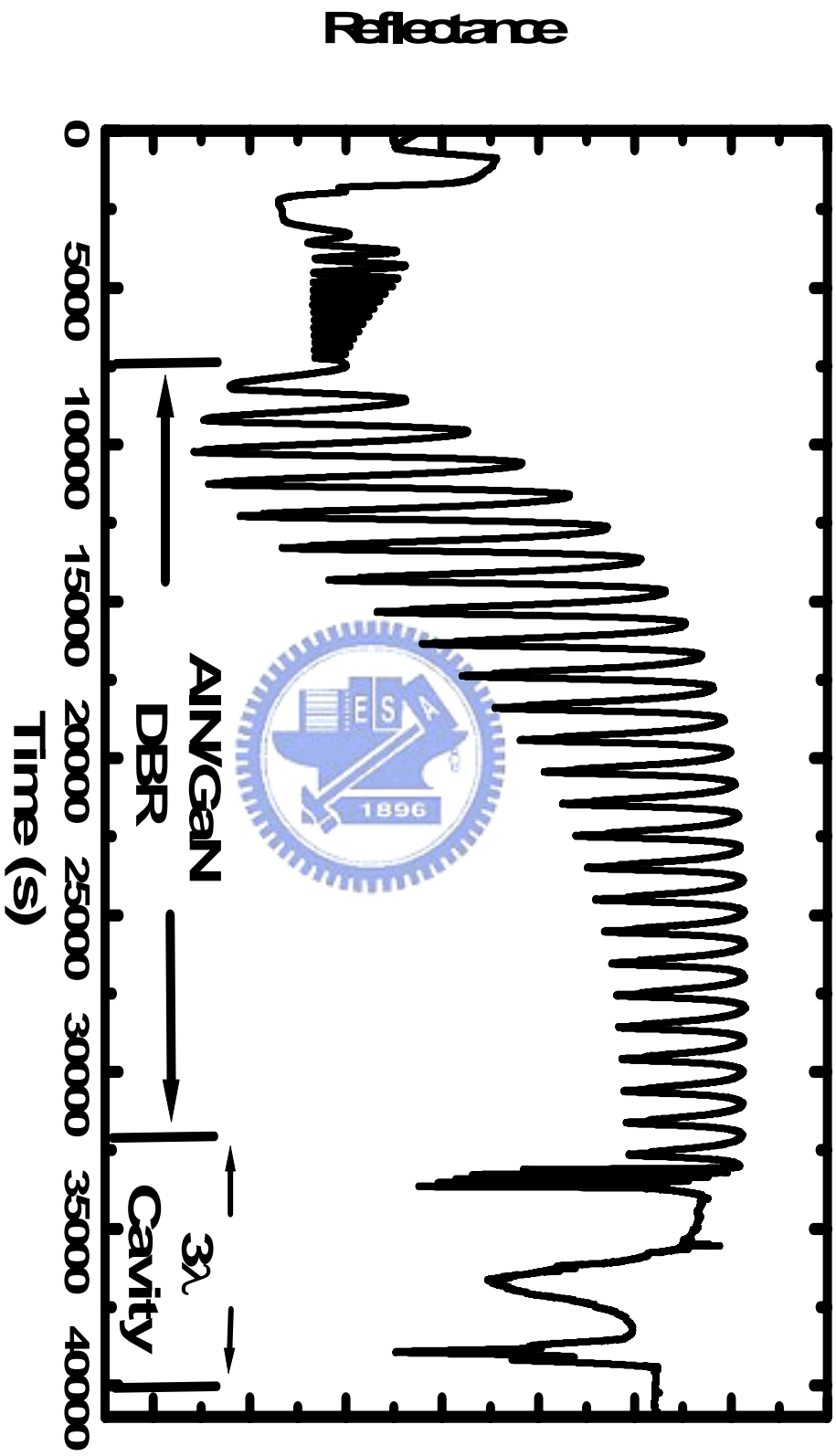


Figure 4-1 The measured reflectivity of nitride-based microcavity structure on sapphire.

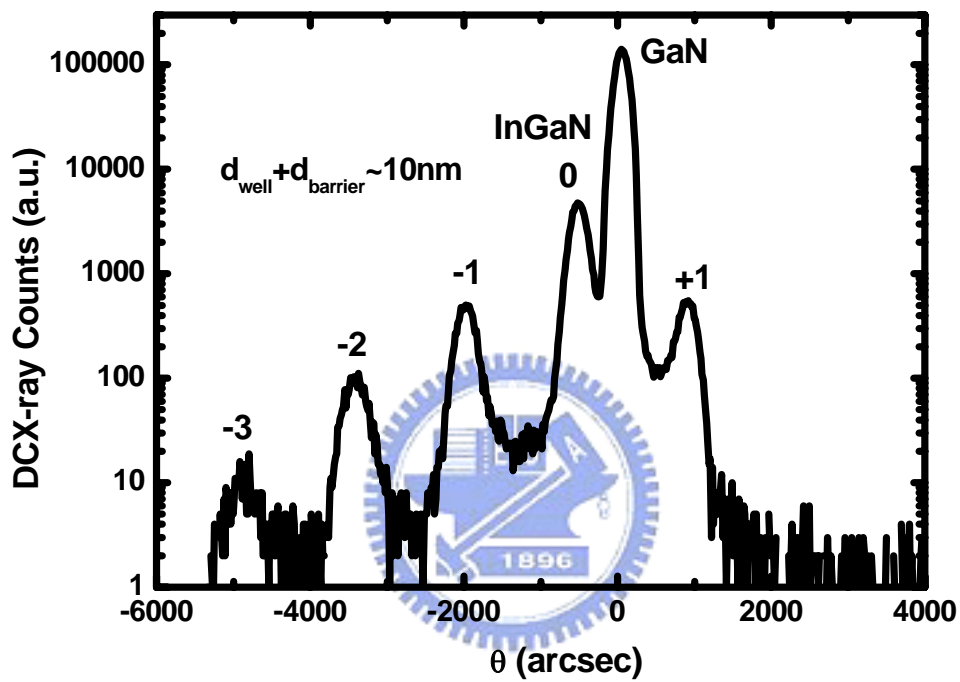


Figure 4-2 The DCX-ray rocking curve of 10-pair InGaN/GaN MQW structure used in the 3λ nitride-based microcavity structure.

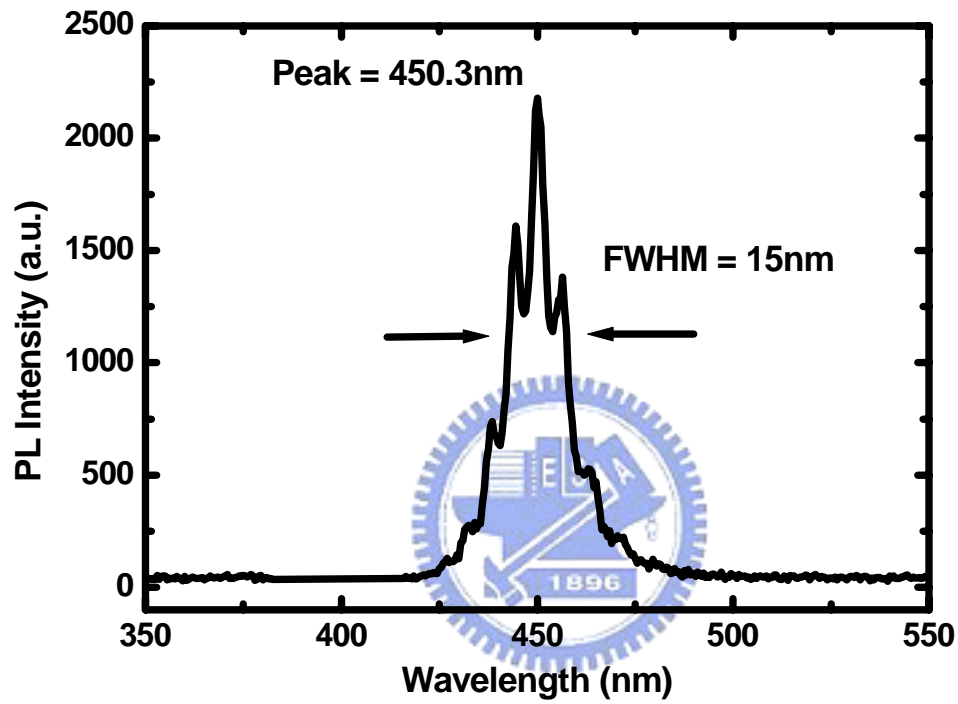


Figure 4-3 The photoluminescence spectrum of 10-pair InGaN/GaN MQW structure.

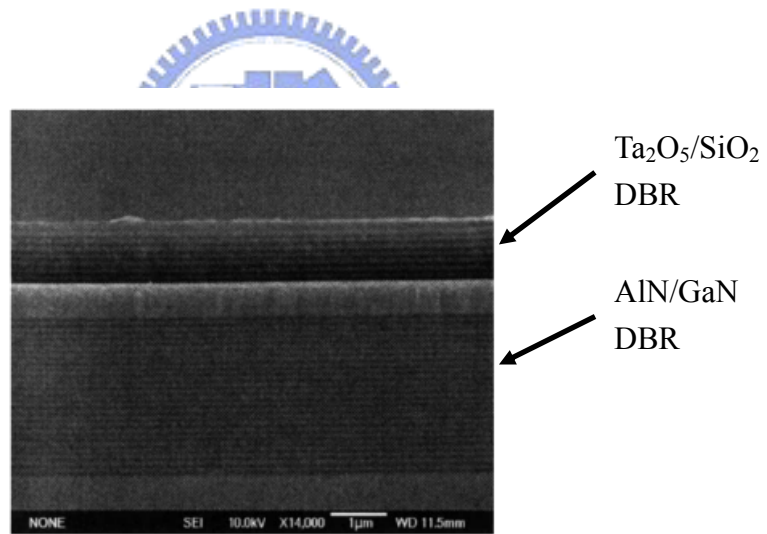
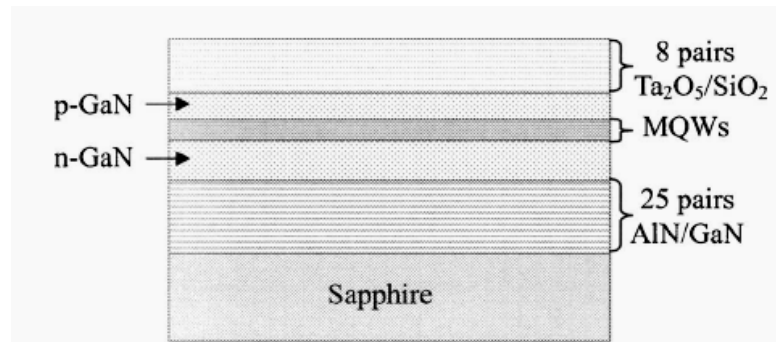


Figure 4-4 (a) The schematic diagram of the overall vertical-cavity surface emitting laser structure. (b) The SEM image of the full structure.

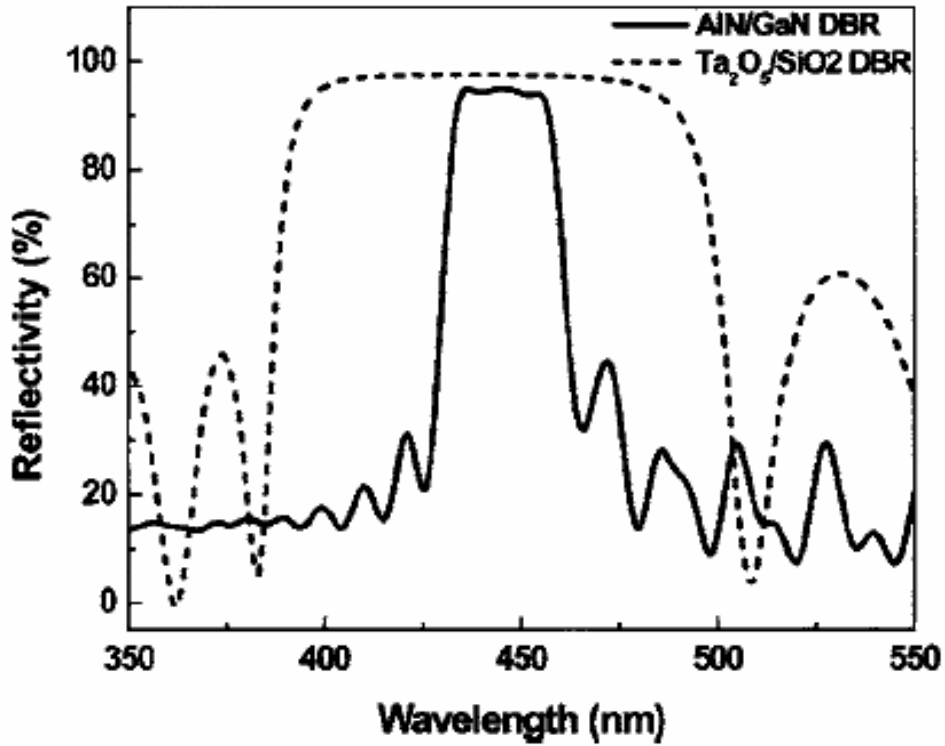


Figure 4-5 The reflectivity spectrum of the top 8-pair Ta₂O₅/SiO₂ DBR, and the bottom 20-pair AlN/GaN DBR; the peak reflectivity of the top and bottom DBRs are about 97.5% and 94% at 450 nm, respectively.

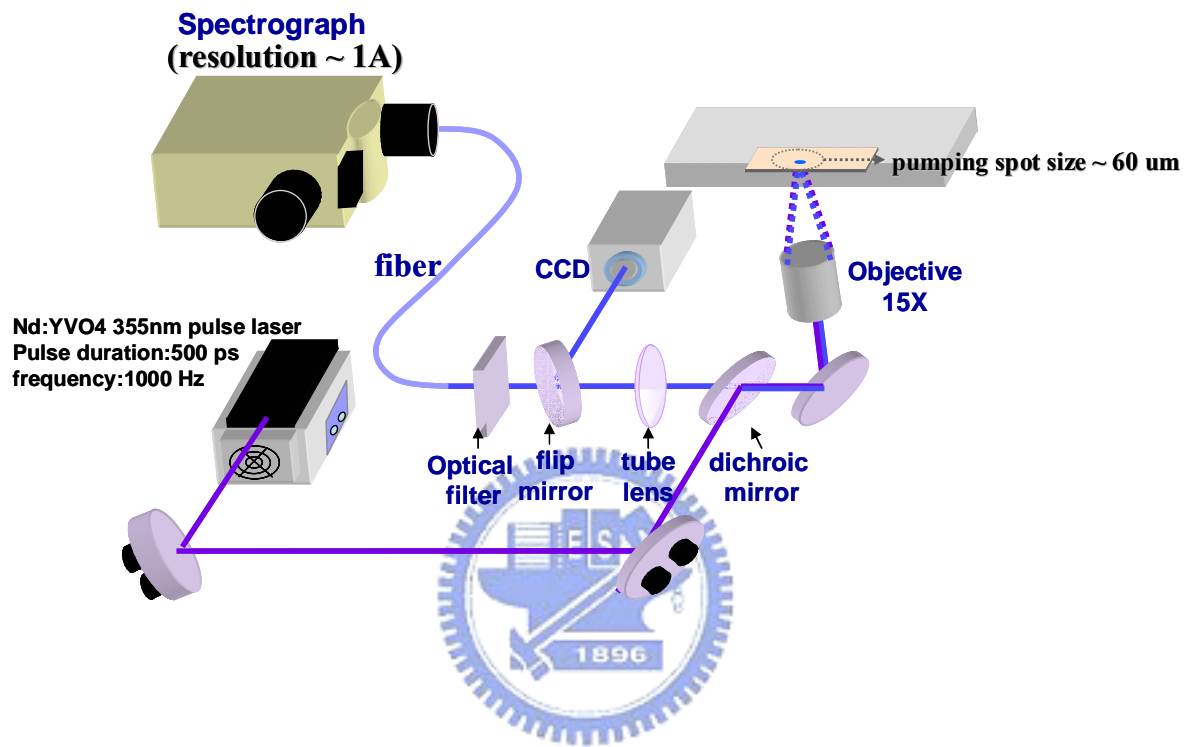


Figure 4-6 The schematic diagram of setup for optical pumping nitride-based microcavity structure

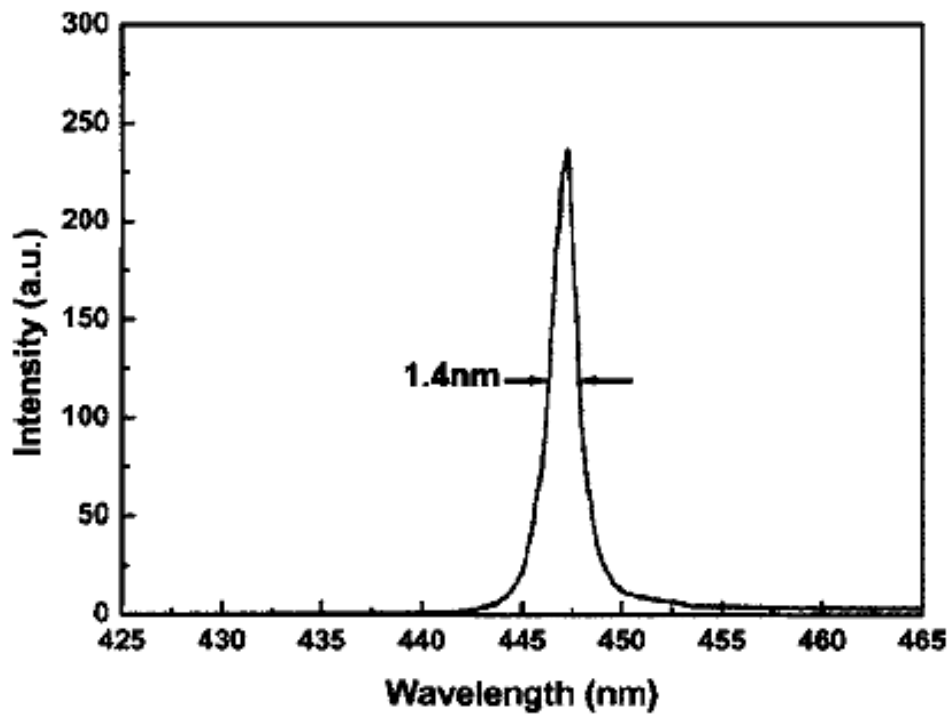


Figure 4-7 The PL spectrum of the GaN-based VCSEL at room temperature.

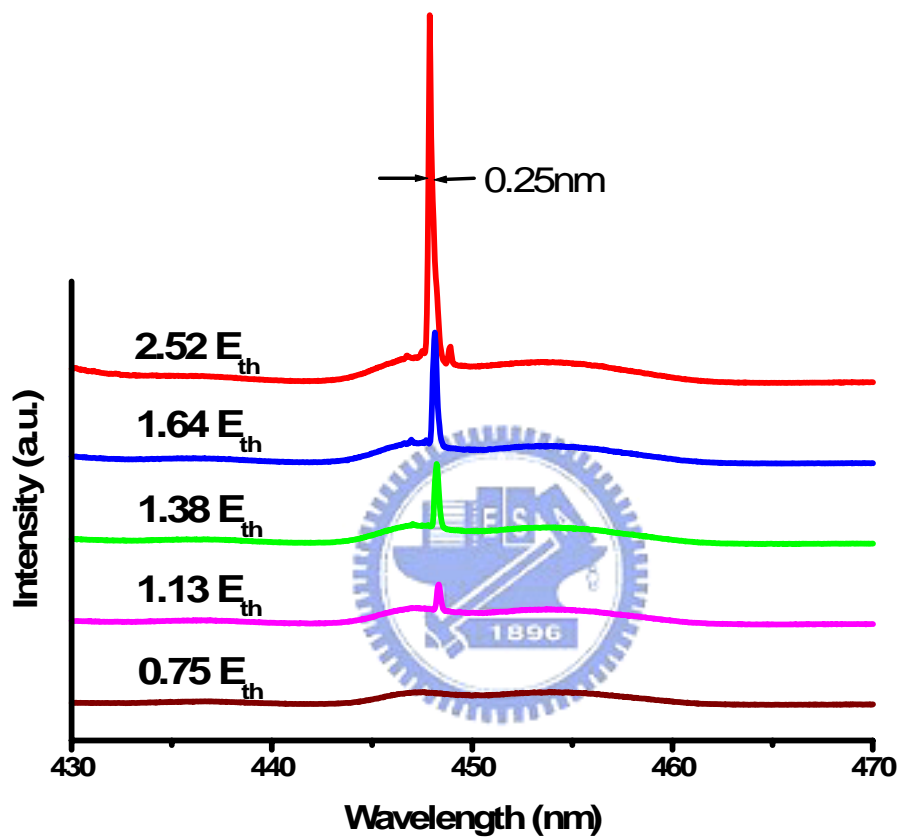


Figure 4-8 The variation of laser emission spectrum with the increasing pumping energy. The laser emission wavelength is 448 nm with a linewidth of about 0.25 nm.

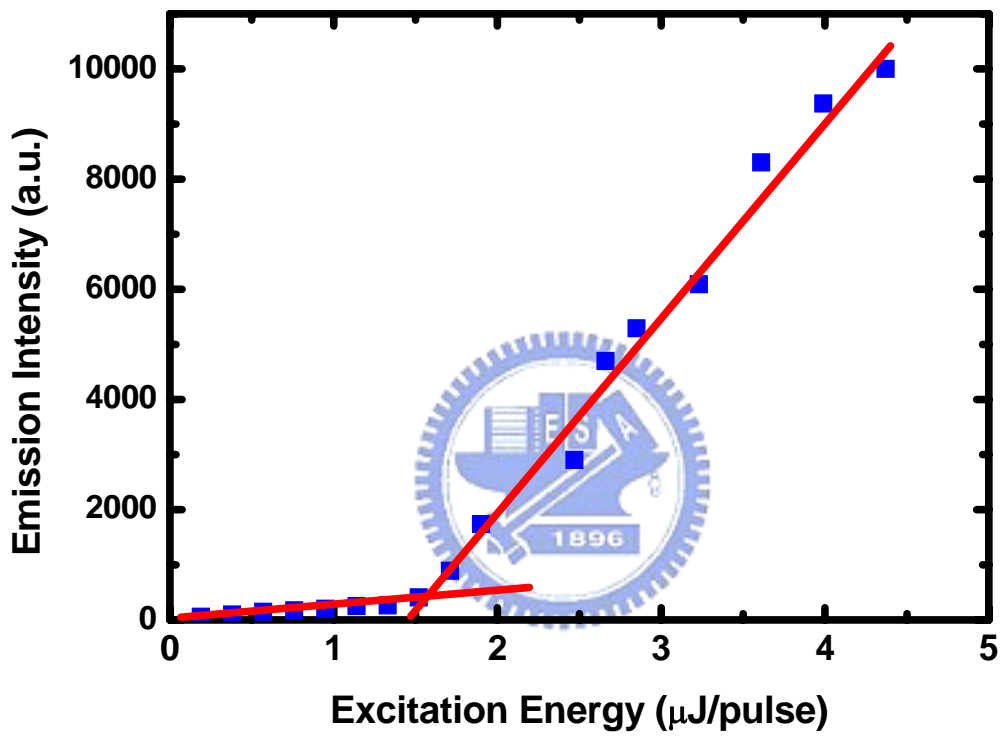


Figure 4-9 Emission intensity versus excitation intensity of the nitride-based microcavity. The threshold energy was about 1.5 μJ .

Parameter	Value
<i>The reflectivity of the top mirror at 355nm</i>	40%
<i>The GaN absorption coefficient at 355nm</i>	10^5 cm^{-1}
<i>The quantum efficiency</i>	10%^b
<i>The number of quantum well (N_w)</i>	10
<i>The width of each quantum well (L_w)</i>	2.5nm
<i>The reflectivity of the top mirrors (R_1)</i>	97.5%
<i>The reflectivity of the bottom mirrors (R_2)</i>	94.5%

Table 4-1 The parameters used in the estimation of threshold gain and threshold carrier density.

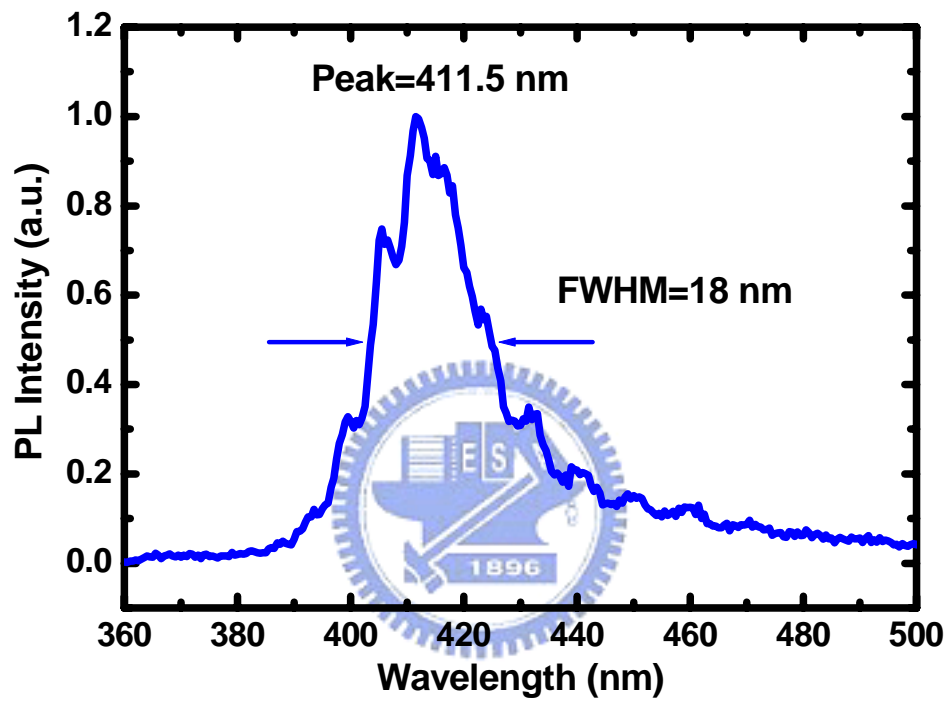


Figure 4-10 The photoluminescence spectrum of 10-pair InGaN/GaN MQW structure used in the nitride-based MCLED structure.

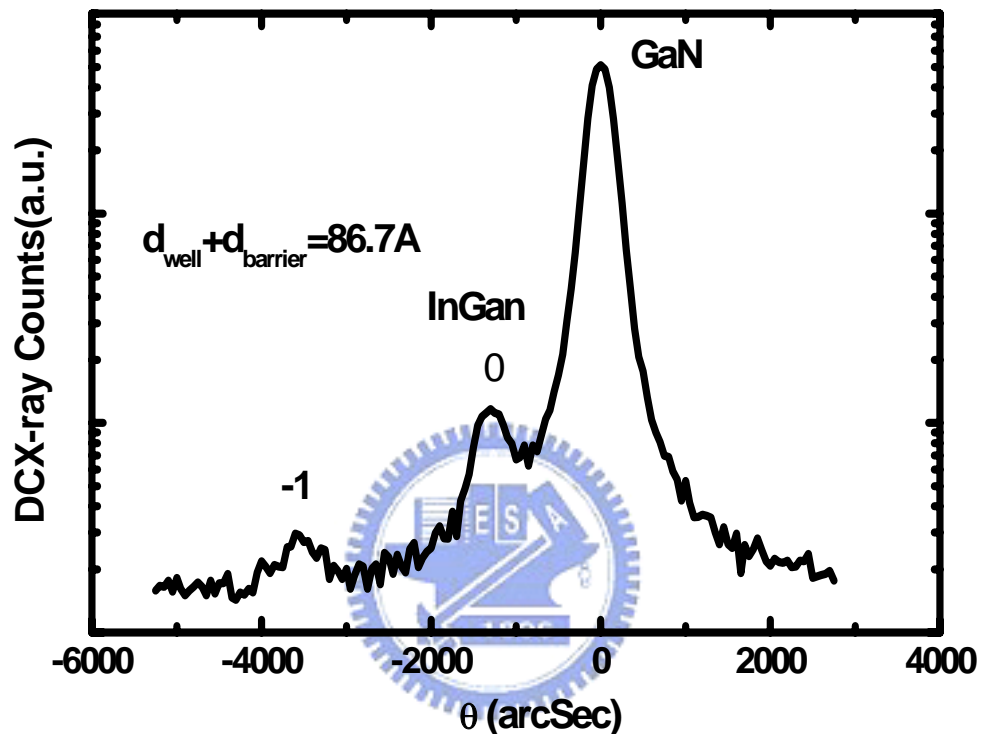


Figure 4-11 The DCX-ray rocking curve of 10-pair InGaN/GaN MQW structure used in the nitride-based MCLED structure.

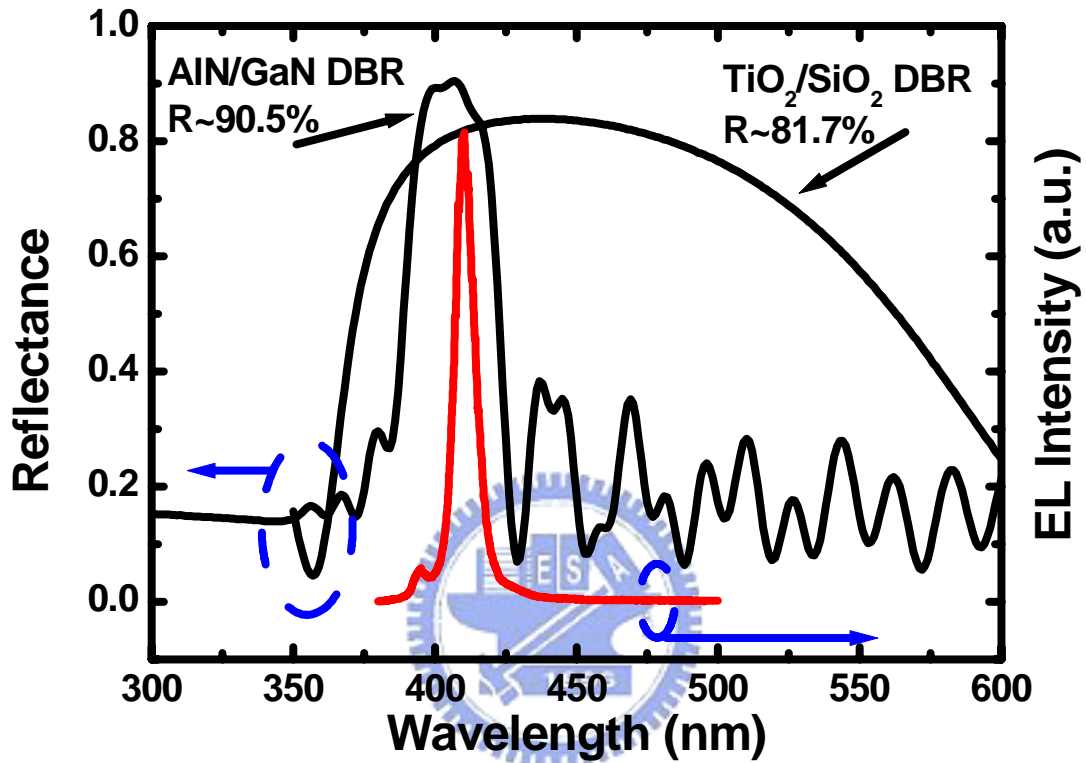


Figure 12. Reflectance of 2-pairs TiO₂/SiO₂ DBR and 20-pairs AlN/GaN bottom DBR. The EL emission spectrum was located at 410 nm in these two DBRs high reflectance spectra.

-
- 1. Degreasing by ultrasonic baths in acetone (ACE) 5 min;**
 - 2. Dipping by ultrasonic baths in isopropyl alcohol (IPA) 5 min;**
 - 3. Rising in de-ionize water (D.I. water) 5 min for surface clean;**
 - 4. Blowing with N₂ gas for surface drying;**
 - 5. Baking by hot plate 120oc ,5min, for wafer drying.**
-

Table 4-2 Initial Clean (I.C.) Process



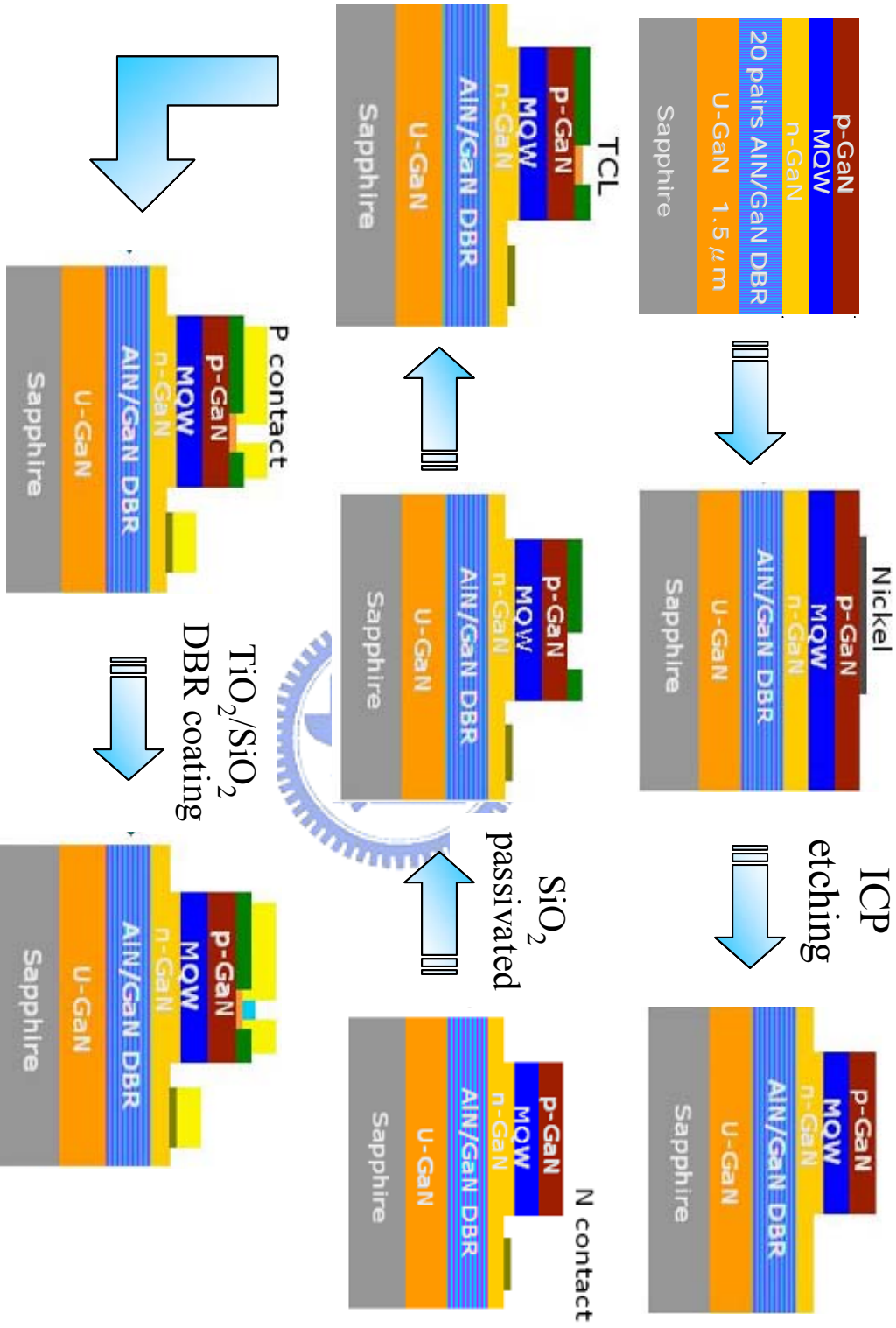


Figure 4- 13 The Process steps of the nitride-based microcavity light emitting device on sapphire

Step	Goal	Process
1	<u>Mesa</u>	(1) I.C.; (2) define pattern of mesa by photography; (3) Ni mask deposited by E-gun; (4) dry etching by ICP to form the mesa structure; (6) remove Ni mesa etching mask by HNO ₃ .
2	<u>N-contact</u>	(1) I.C.; (2) define pattern of N-contact by photography(IR exposure); (3) Ti/Al/Ni/Au(20nm/150nm/20nm/200nm)deposited by E-gun and lift-off.
3	<u>Passivated</u>	(1) I.C.; (2) grow 300nm SiO ₂ by PECVD; (3) define pattern of passivated by photography (positive exposure); (4) wet etching by BOE to define the SiO ₂ current confined structure.
4	<u>TCL</u>	(1) I.C.; (2) define pattern of TCL by photography (IR exposure); (3) Ni/Au(5nm/5nm) deposited by E-gun and lift-off.
5	<u>P-contact</u>	(1) I.C.; (2) define pattern of P-contact by photography (IR exposure); (3) Ni/Au (20nm/200nm) deposited by E-gun and lift-off.
6	<u>DBR</u>	(1) I.C.; (2) define pattern of DBR by photography (IR exposure); (3) SiO ₂ / TiO ₂ DBR deposited by E-gun and lift-off.

Table 4-3 Detail process flowchart of nitride-based MCLED structure.

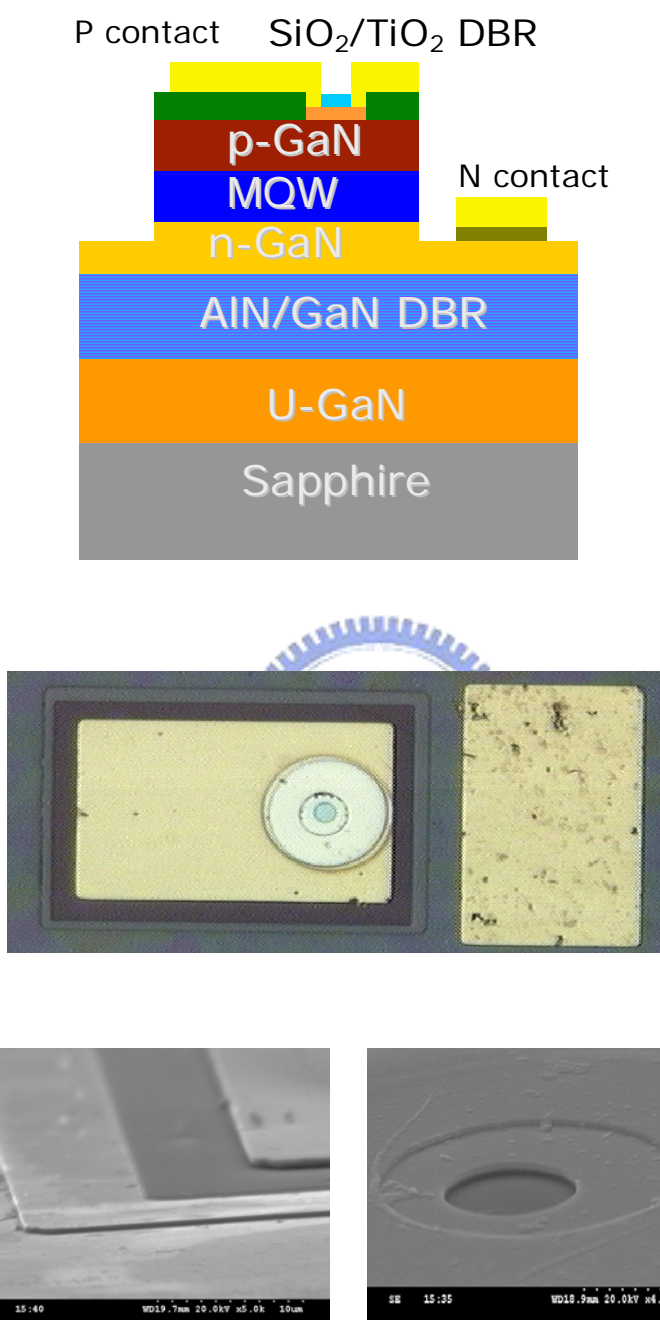


Figure 14 (a) 2D schematic diagram of completed nitride-based MCLED structure. (b) microscopic top view image of MCLED. (c) SEM images of MCLED.

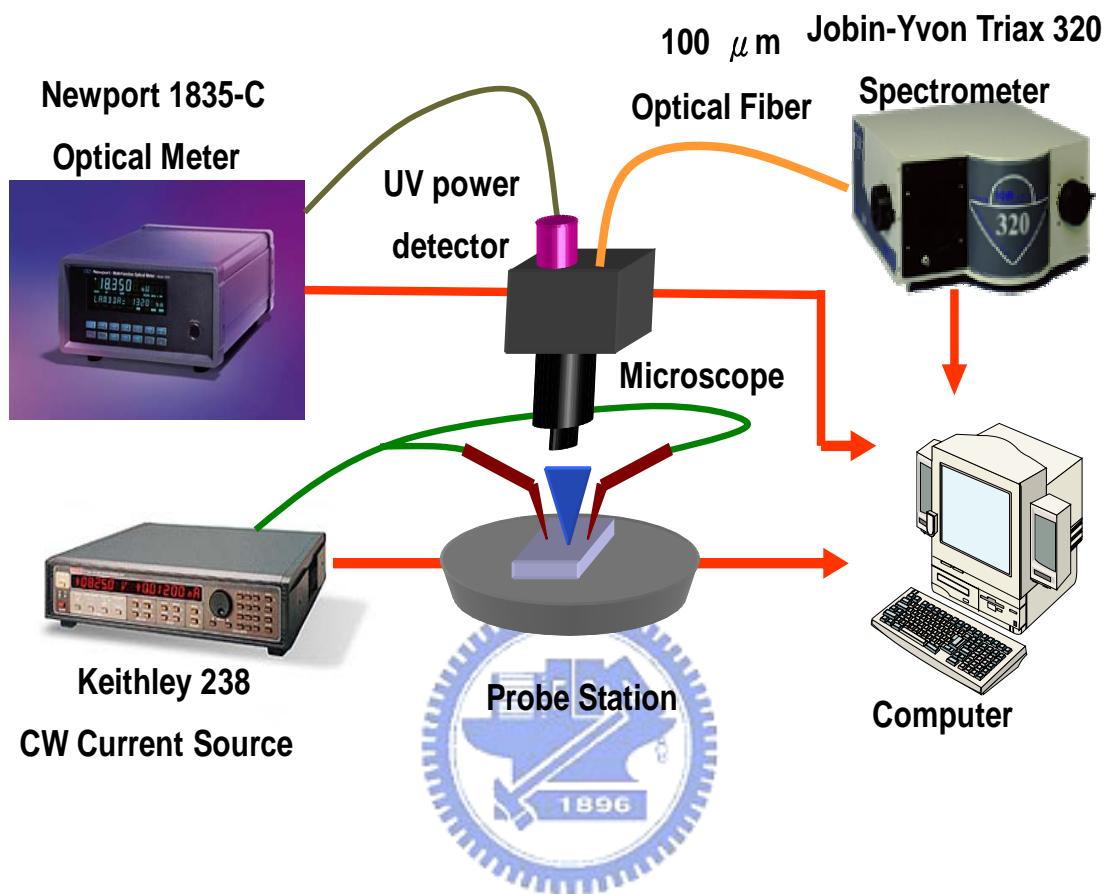


Figure 15 The setup of EL measurement system

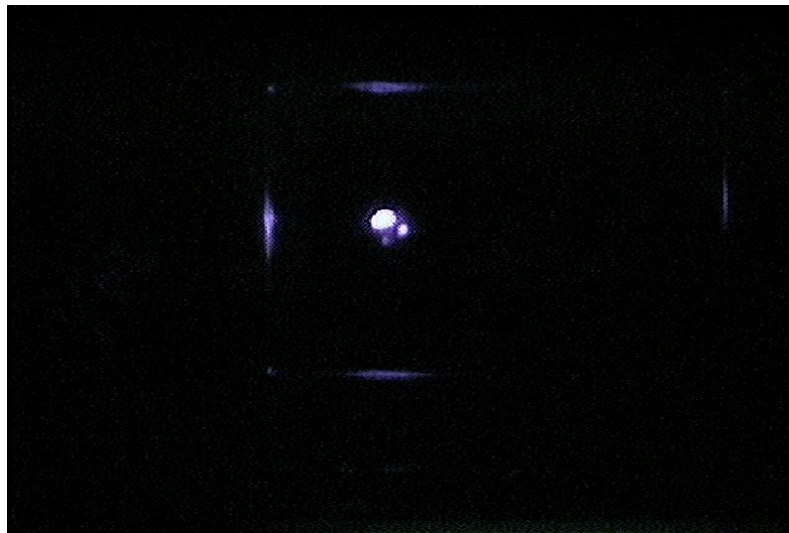
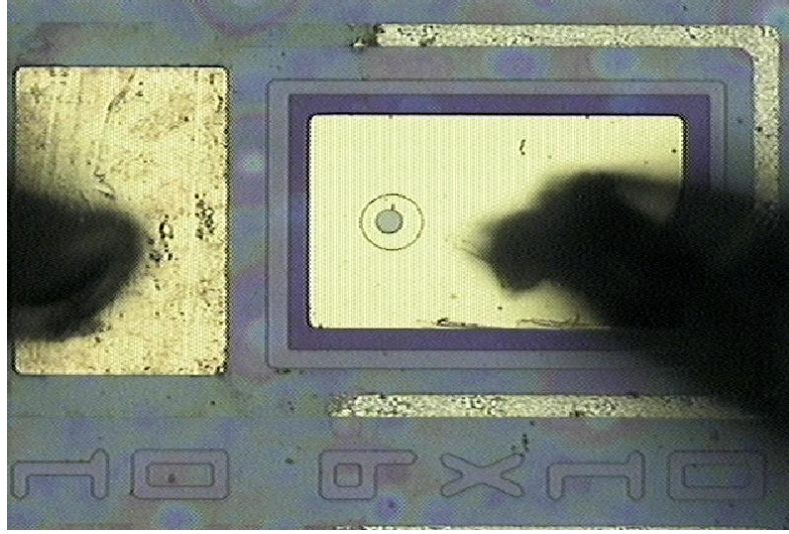


Figure 16 The top view of light emission photograph of the MCLED at 20mA current injection

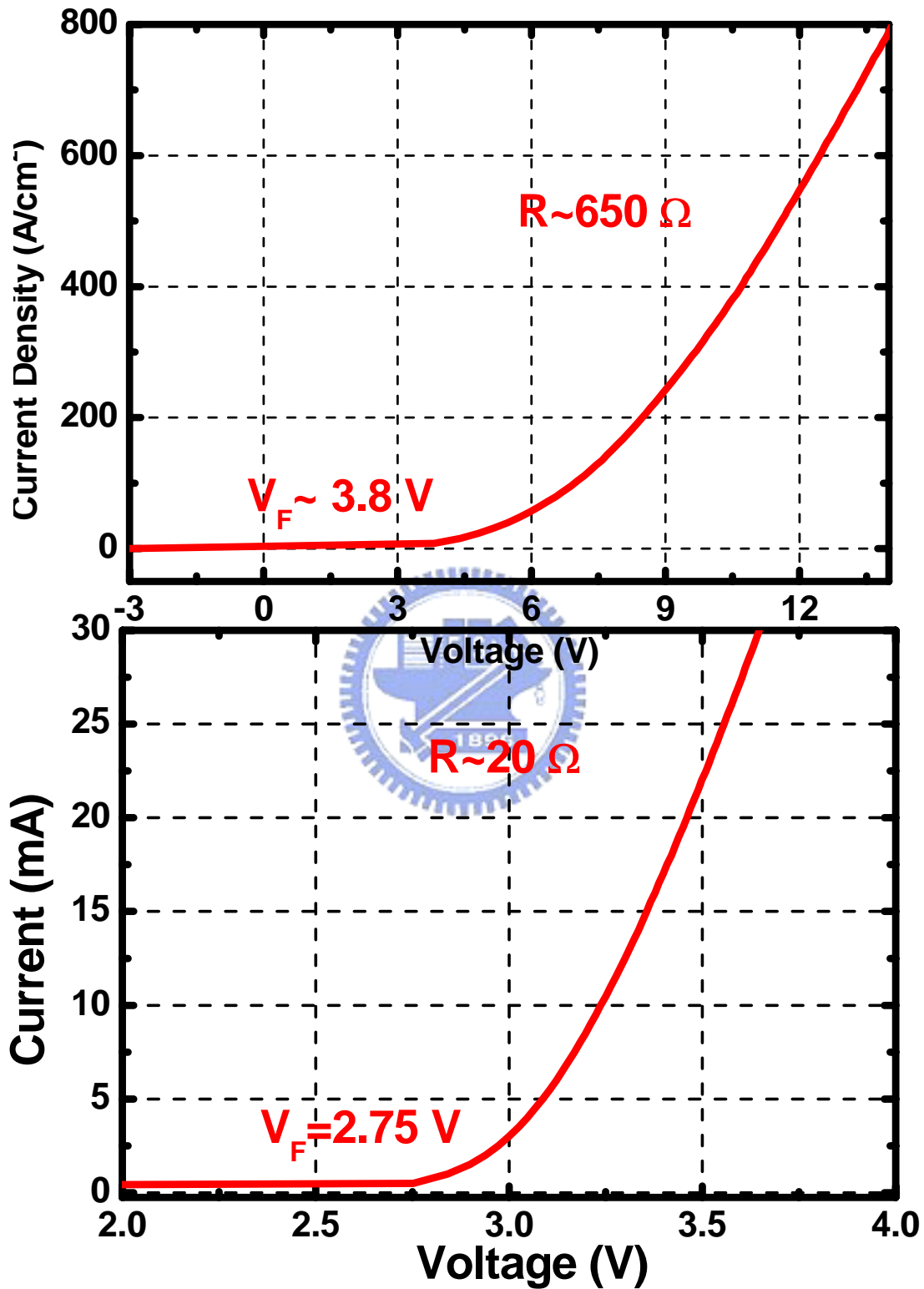


Figure 17 The I-V curves of nitride-based MCLED and commercial LED structures

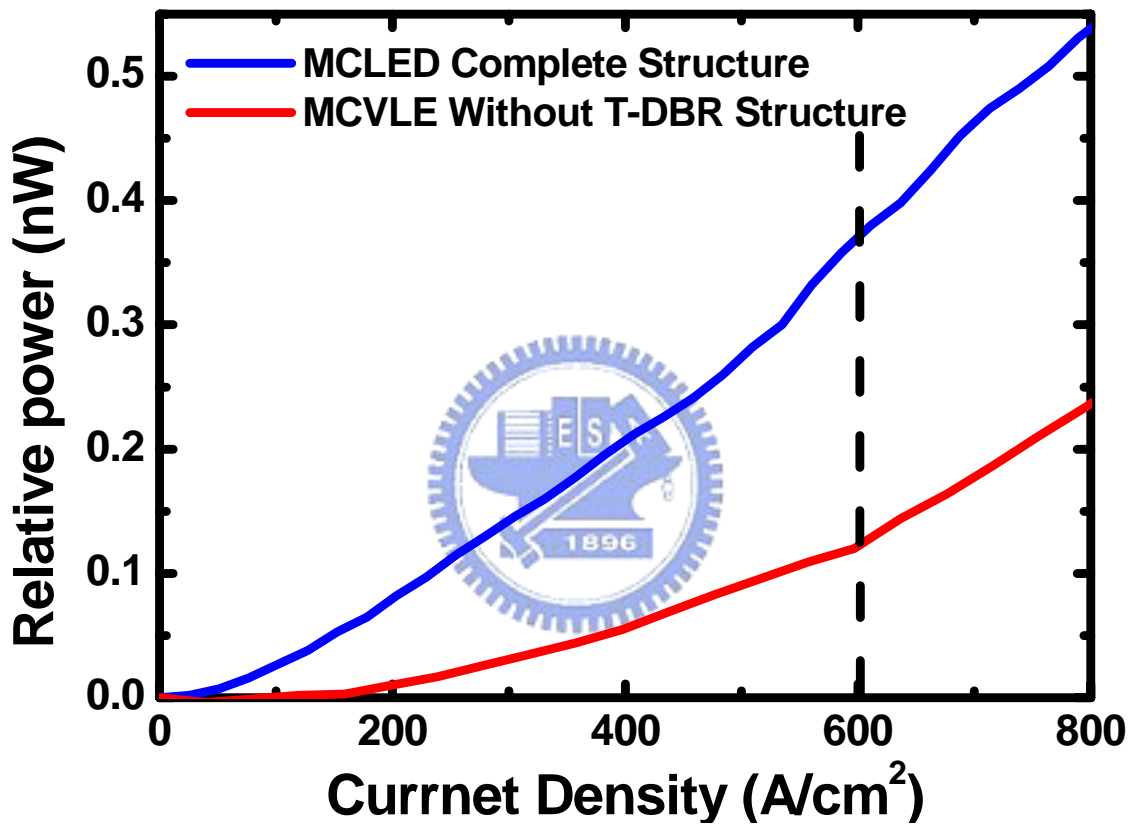


Figure 18 Comparison of the output power of the complete MCLLEDs and without top TiO₂/SiO₂ DBR structure at different injection current densities.

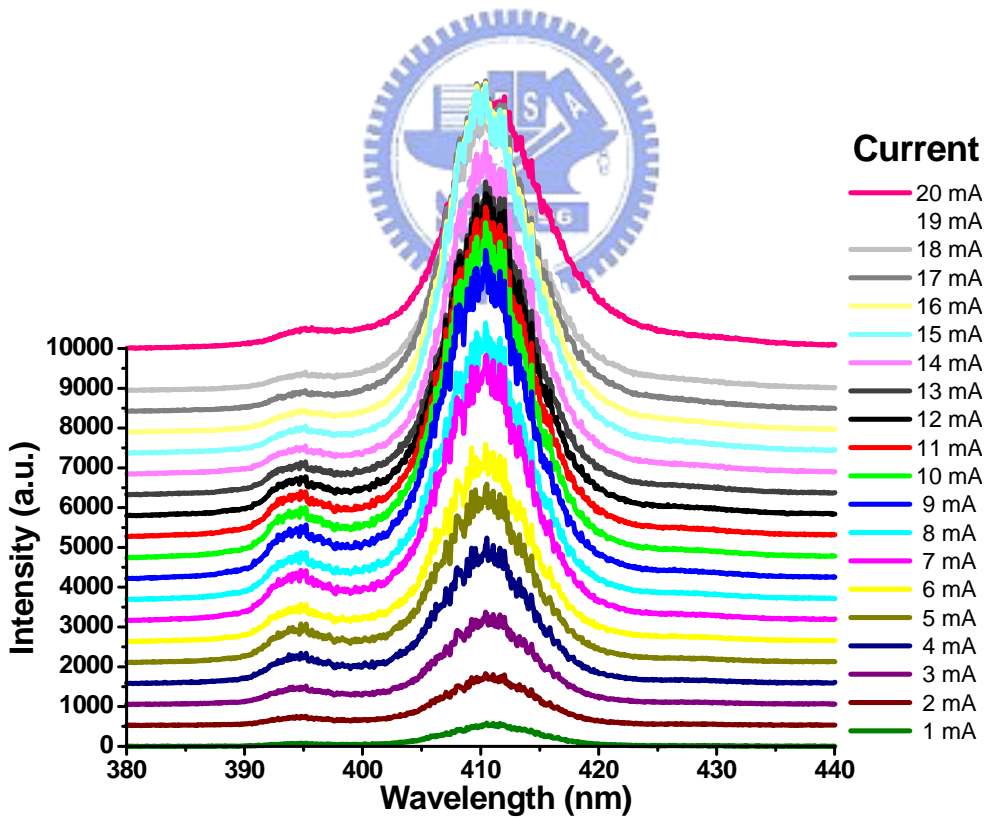
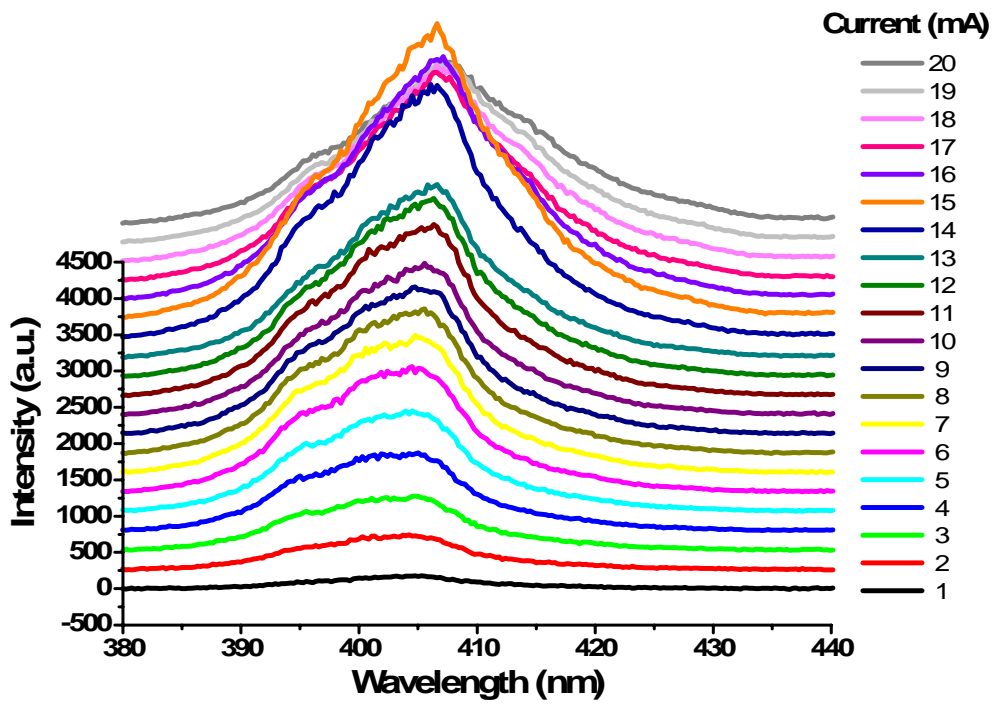


Figure 19 EL spectra of (a) without top-DBR and (b) complete MCLED structures under various current driven.

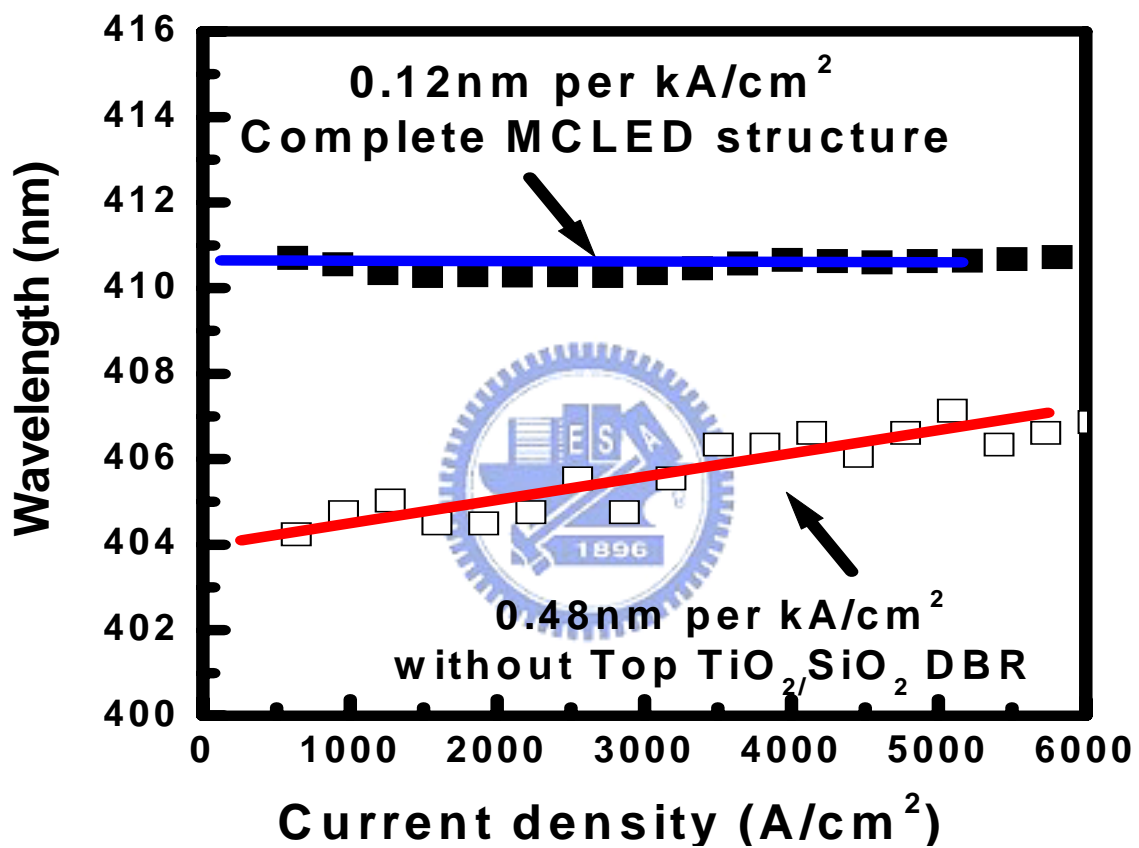


Figure 20 The current dependence of the peak positions of the complete and without top DBR nitride-based MCLD structures.




Chapter 5

Self-Assembled InGaN Quantum Dots Grown by MOCVD System

Chapter 5 reports the self-assembled InGaN QDs structure grown by MOCVD system.

We start this section with the introduction of techniques of self-assembled nitride-based QDs structures. It includes the anti-surfacent method, strain induced method, and phase separation. After that, the effect of growth interruption on self-assembled InGaN QDs will be discussed.

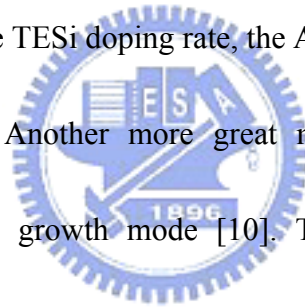
5-1 Introduction of Self-Assembled Nitride-Based Quantum Dots



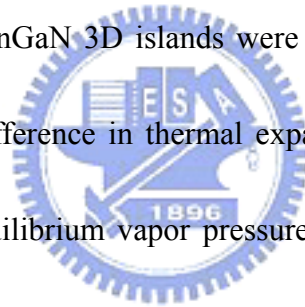
In section 1-4, QD structures have been introduced to be of great interest for development of new devices with superior performance. For example, LDs with QDs embedded in the active layer are predicted to improve laser characteristics, such as suppression of temperature dependence of the threshold current [1], a reduced threshold current density [2, 3], high-frequency modulation with negligible chirping effect [4], and nonlinear gain effect [5]. Nitride-based QDs will be more efficient in reaching lasing threshold because to the zero-dimensional electronic density of states in the QDs play an essential role for improving threshold current characteristics particularly in wide bandgap semiconductors [6, 7]. Moreover, nitride-based QDs structure could obtain high internal

quantum efficiency since the localized carriers in the QDs could minimize the effect of large defect density generated due to the use of foreign substrate with large lattice mismatch [8].

The self-assembled InGaN QDs grown by MOCVD was first reported by using anti-surfactant to change the surface free energy of epi-layers [9]. Si as the anti-surfactant was used to form the InGaN QDs in the InGaN/AlGa_xN system. The dose of TESI to the AlGa_xN surface was found to play a significant role as a surfactant to establish dot structures, with no dot being formed without TESI. The size and density of the InGaN dots were controlled by the TESI doping rate, the Al content of the Al_xGa_{1-x}N surface, and the growth temperature. Another more great method to form 3D island is called Stranski-Krastanow (S-K) growth mode [10]. The epitaxial growth by MOCVD is essentially a non-equilibrium process, and it is very useful to categorize it into three different modes as in equilibrium theory. These three growth modes with a schematic diagram shown in Figure 5-1 represent a layer-by-layer or 2D growth (Frank-Van der Merwe mode, FVDM mode), a island or 3D growth (Volmer-Weber mode, VW mode), and a 2D layer followed by 3D islands (S-K mode). These modes are deduced from equilibrium considerations of the surface and interface energies for lattice mismatch systems. In a lattice-mismatched system, the bulk elastic energy in the epilayer induced by strain plays an important role. Since it increases with layer thickness, a strain



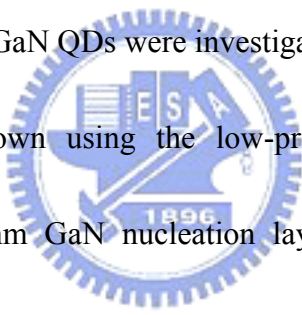
relaxation is expected when the layer thickness is increased beyond a critical value. In this case, the stress field tends to force the atoms to coalesce. The strain energy can be partially released by the formation of islands through elastic relaxation, without any dislocations in the islands. GaN QDs structures were also grown by MBE and MOCVD systems [11, 12]. The size and density of the GaN dots formed by S-K growth mode were controlled by growth thickness and growth temperature. The self-assembled InGaN QDs structure without using anti-surfactant was also reported [13]. The surface morphology of InGaN QDs was depended on InGaN thickness and growth temperature. However, it is generally believed these InGaN 3D islands were formed by In-segregation because the large lattice mismatch, difference in thermal expansion coefficients, and several orders difference of nitrogen equilibrium vapor pressure between GaN and InN would lead a phase separation of InGaN and the formation of nanometer-scale In-rich clusters [14-19]. It is likely that the high-quantum efficiency of InGaN-based laser emitting diodes is mostly due to the large localization of excitons because the pathways of nonradiative recombination are hindered once the excitons are captured in a small volume.



5-2 Effects of growth interruption on InGaN/GaN self-assembled quantum dots grown by MOCVD

This section reports the Effects of growth interruption on InGaN/GaN self-assembled quantum dots grown by metal organic chemical vapor deposition. The growth

interruption, as an important technique for improving quality of the quantum-structure interface, was believed to facilitate the elastic relaxation resulting in the formation of the 3D island formation [20]. In addition, the adatoms can relax to energetically favorable position and approach thermodynamic equilibrium during the interruption growth [21]. As a result, ad-atoms desorption and diffusion effects during the growth interruption shall influence the morphological and optical properties of the QDs. The effect of thermal treatment during the growth interruption on formation of InGaN QDs has been studied. The influences of adatom desorption and diffusion effects on the morphological and optical properties of the InGaN QDs were investigated.



All samples were grown using the low-pressure vertical-type EMCORE D-75 MOCVD system. A 30 nm GaN nucleation layer were grown first at 500°C on a (0001)-oriented sapphire substrate followed by a GaN buffer layer under H₂ ambient gas grown at 1110°C. During the growth of a GaN buffer layer, the flow rate of trimethylgallium (TMG) was 68.4 μ mol/min and NH₃ was used as a group V source with a flow rate of 3 l/min, corresponding to a V/III ratio of about 2000. After the GaN buffer layer was grown, the growth temperature was reduced to 660°C to grow an InGaN layer with a V/III ratio of about 8300. Contrarily to the standard InGaN quantum well growth, the growth temperature and V/III ratio were reduced to facilitate the InGaN quantum dot growth [13]. The optimal growth time judged by QDs density was

determined to be 30 s. After the InGaN growth was completed, a growth interruption was introduced for these samples with different interruption time (t_{int}) of 30 s, 60 s, and 120 s for sample A, B and C, respectively. The schematic diagram of the overall InGaN QDs structure is shown in Figure 5-2. The surface morphologies of these samples were examined by atomic force microscopy (AFM). The AFM data were analyzed by Scanning Probe Image Processor (SPIP) to gather the geometric statistics of InGaN QDs. The optical characteristics of these samples were investigated by photoluminescence (PL) using a commercial microscope system.

Figure 5-3 shows the reflectance intensity and AFM image of the GaN/sapphire template. Figure 5-3(a) is the reflectance traces measured by a real-time in situ normal-incidence optical reflectometer ($\lambda = 600$ nm). The trace of the reflectance intensity proceeded with several stages during GaN growth: (i) the nucleation layer growth, (ii) temperature ramping for high temperature undoped GaN growth, (iii) lateral growth and surface roughening, (iv) island coalescence, and (v) quasi-two-dimensional (2D) growth of undoped GaN. Figure 5-3(b) shows the AFM image of the surface morphology of the GaN/sapphire template. There are some dark spots on the surface with a density of about 3×10^8 cm⁻². The surface of the GaN/sapphire template is very flat with an average deviation $R_a = 0.14$ nm for the surface roughness. Previous report had shown that the flat template surface was important to fabricate self-assembled InGaN QDs without using

anti-surfactant [13].

Figure 5-4(a) is the typical AFM scanned result over an area of $1 \mu\text{m}$ square of sample B with the interruption time of 60 s. A section analysis along the dash line in Figure 5-4(a) is shown in Figure 5-4(b), and the dense QDs distribution can be observed. Figure 5-4(c) clearly shows the shape profile of a single InGaN QD structure with the lateral size and height of about 30 nm and 0.8 nm, respectively. Figure 5-5 shows AFM images of InGaN QDs for different InGaN growth and interruption time. In order to gather the geometric statistics of InGaN QDs, SPIP was used to analyze the AFM data of InGaN QDs structures. The dependence of average size and the density of InGaN QDs on the growth time were shown in Figure 5-6 (a) and (b), respectively. The results show that the QD density depends on the InGaN growth time. The mean sizes (diameter, height) of the QDs are (11.5 nm, 1.6 nm), (16.7 nm, 2.1 nm), and (18.3 nm, 2.6 nm) for the growth time of 30, 40, and 50 s, respectively. As the InGaN growth time was increased from 30 to 50 s, the QD density decreased from $4.5 \times 10^{10} \text{cm}^{-2}$ to $3.7 \times 10^{10} \text{cm}^{-2}$.

The effect of growth interruption on the morphology of InGaN QDs was studied by various the interruption times from 30 s to 120 s with InGaN growth time fixed at 30s. The surface roughness of average deviation decreases from $R_a = 0.26 \text{ nm}$ to $R_a = 0.21 \text{ nm}$ by increasing tint from 30 s to 120 s. It indicated that the growth interruption at 660°C could influence the surface morphologies. From the SPIP analysis, the lateral size and

height histograms associated with each sample are shown in Figure 5-7. The standard deviation of QDs height is 1.19 nm, 0.78 nm, and 0.91 nm for sample A, B, and C, respectively. The results indicated that the growth interruption may be beneficial for uniform distribution of InGaN QD size. Figure 5-8 (a) shows the averaged height and diameter of the samples with various interruption times. The mean size (diameter, height) of sample A, B and C are (14 nm, 2.4 nm), (11.5 nm, 1.6 nm), (15 nm, 2.5 nm), respectively. The InGaN QDs reduced first then increased their dimension as the interruption time increased. Figure 5-8 (b) shows the interruption time dependence on the QDs density and the QDs coverage, which describes how many QDs occupied on the surface above the wetting layer. The QDs coverage increased from 20.0% to 28.8% by increasing tint from 30 s to 120 s. However, the QDs densities were $2.88 \times 10^{10} \text{ cm}^{-2}$, $4.5 \times 10^{10} \text{ cm}^{-2}$, and $3.28 \times 10^{10} \text{ cm}^{-2}$ for sample A, B, and C, respectively. Sample B with tint = 60 s had the largest QDs density. These morphological results could be explained by the influence of ad-atom diffusion and desorption effect. The QDs coverage always increases as the interruption time increases implies that the sample surface has ad-atom surface diffusion effect during the process of interruption growth. During the growth interruption period $30 \text{ s} < t_{\text{int}} < 60 \text{ s}$, the increase in dot density indicated that new InGaN dots were generated by the ad-atom diffusion from wetting layers. On the same time, the ad-atom desorption from “old” dot structures could reduce the size of QDs structure. Therefore,

the average dot size is decreased during the growth interruption period $30 \text{ s} < t_{\text{int}} < 60 \text{ s}$. During the further process of interruption growth after 60 s, the decrease of dot density and increase of average size could be mainly ascribed to the ad-atom surface diffusion between the InGaN QDs, leading to the enlargement of the larger islands combining the smaller ones due to the Ostwald ripening [22].

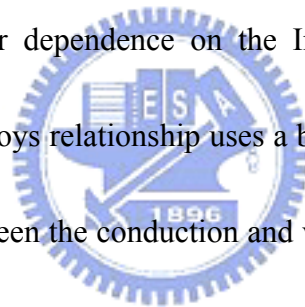
Figure 5-9 shows the PL spectra of InGaN QDs under various interruption times from 30 to 120 s at room temperature (RT). A He-Cd laser was used as the excitation source in the PL measurement. The PL emission peaks were 2.49 eV, 2.60 eV, and 2.72 eV, and the PL linewidths were 170 meV, 210 meV, and 180 meV for samples A, B, and C, respectively. The RT-PL of the InGaN QDs samples shows a blue-shift trend as the interruption time was increased from 30 s to 120 s. However the average heights of the InGaN QDs samples were 2.4 nm, 1.6 nm, and 2.5 nm for samples A, B, and C, respectively as shown in Figure 5-8 (a), indicating that the sizes of InGaN QDs do not always decrease with increasing the interruption time. The blue-shift of the PL emission peak may be caused by the reduction of the In composition in the InGaN QDs during the growth interruption. The similar effect was also reported in the InGaAs QDs [23]. The decrease of In composition in the InGaN QDs suggests that the desorption rate of In atoms could be faster than that of Ga atoms at 660°C .

Temperature-dependent PL was performed on samples A, B, and C in order to study

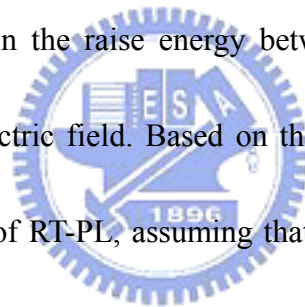
the radiative efficiency of the InGaN QDs. Figure 5-10 shows the Arrhenius plot of the integrated PL intensity for the three samples. The experimental data were fitted by the well-known PL thermal quenching equation $I = C \exp(E_A/kB_T)$, where E_A was attributed to the height of the energy barriers which a thermally activated carrier should pass through to release its energy via emission of phonons [24]. The corresponding thermal activation energies E_A from the high temperature range of the figure were extracted and obtained to be 63.1 meV, 89.7 meV, and 35.0 meV for samples A, B, and C, respectively. These values of the thermal activation energy could also describe the carrier confinement capability of the QDs structure. High carrier confinement capability assured a high internal quantum efficiency and radiative efficiency. The highest thermal activation energy occurred at $t_{\text{int}} = 60$ s indicated that the growth interruption technique could improve the radiative efficiency. However, the decrease in the activation energy of sample C could be related to the deformation of InGaN QD structure since the long growth interruption with 120 s would tend to destroy the InGaN QDs structure, resulting in the strain relaxation and the subsequently defects generation in the InGaN QDs during the long growth interruption step. Table 5-1 is the arrangement of PL measurement results.

In order to evaluate the In composition in InGaN QDs, the electron and hole ground state energy levels for three InGaN QDs samples were calculated by modeling the QD as

an InGaN pyramid standing on a GaN surface. For uncapped QDs structure, infinite barriers were used in all direction except for the contact area between InGaN and GaN interface where a finite barrier was used. The InGaN QD structure was supported with a perfect cylindrical symmetry, therefore the eigenstate of InGaN QD structure can be calculated in cylinder coordinate. Figure 5-11 is the schematic of the simulation model of InGaN QD structure. Table 5-2 is the necessary parameters for calculating the ground state energy levels of InGaN QD structure. The effective masses and the dielectric constants used in the calculated were interpolated between the values of pure GaN and InN by assuming a linear dependence on the In content [25]. The band gap versus composition for InGaN alloys relationship uses a bowing parameter of about 1.4 eV [26]. The band offset ratio between the conduction and valence band was 7:3 [27]. Figure 5-12 is the simulation result of transition energy shift (ΔE) due to the confinement effect on electrons and holes for these three InGaN QD samples without considering the internal electric fields in QD structure. The simulation result shows that the transition energy shifts for sample A, B, and C are 258 meV, 337 meV, and 245 meV, respectively. The simulation result can not match the tendency of PL emission shift listed in Table 5-1. In order to estimate more accurately the electron and hole ground state energy levels of InGaN QD structure, the effect of an internal electric field was considered because the transition energy of the light emitted from an III-nitride quantum-confined structure

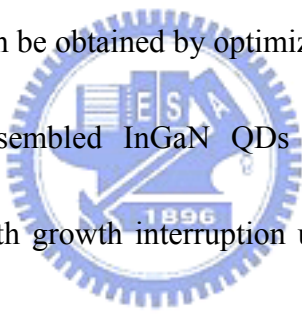


depends not only on the band gap but also on the large internal electric field due to piezoelectric (PZ) and spontaneous polarization [28]. However, the value of the internal electric field was not clear at the present time because the study of III-nitrides is in its infancy and each sample for investigation has different crystal qualities [29]. Fig. 5-13 is the simulation result of transition energy shift (ΔE) due to the confinement effect on electrons and holes for these three InGaN QD samples under various internal electric fields from 0 MV/cm to 1 MV/cm. It can be seen that sample B with a small QD size is not as sensitive to the internal electric field as other samples with a larger QD size. Therefore the difference in the raise energy between samples A and B gets larger as increasing the internal electric field. Based on the results of temperature-dependent PL and the transition energy of RT-PL, assuming that there was no further strain relaxation during $30s < t_{\text{int}} < 60s$, the internal electric field was determined to be as 0.5 MV/cm in samples A, and B. Figure 5-16 is the calculated result of the In compositions for these three samples. The In compositions of samples A and B were 0.28 and 0.27, respectively. However, the In composition of sample C was calculated by extrapolation to be 0.25 and the internal electric field was modified to be 0.2 MV/cm. The reduction of internal electric field in sample C might be resulted from the relaxation of the lattice strain induced by the defect generation, which agrees with the reduced thermal activation energy in sample C. As a result, long growth interruption step could lead to crystal quality



degradation of InGaN QDs structure.

Table 5-3 summarizes the growth interruption effect on InGaN QDs. From the experimental and simulation results, we determined that the growth interruption can modify the size of InGaN QDs and extend the emission wavelength to the short wavelength region, and at the same time improve the QD optical quality by ad-atom desorption and diffusion effects. The desorption effect can decrease the size and In composition of InGaN QDs structure. On the other hand, the surface diffusion effect can increase the QDs areas occupied on the surface above the wetting layer. In addition, the high InGaN QD density can be obtained by optimized the growth interruption time.



In conclusion, self-assembled InGaN QDs structures were grown on sapphire substrates by MOCVD with growth interruption under a low V/III ratio (~8300) and a low growth temperature (660°C). The density of InGaN QDs was about $4.5 \times 10^{10} \text{ cm}^{-2}$ with an average lateral size of 11.5 nm and an average height of 1.6 nm. The effects of the growth interruption time on the morphological and optical properties were studied and simulated. Our results suggested that the growth interruption can modify the size of InGaN QDs and extend the emission wavelength to the short wavelength region, and at the same time improve the QD optical quality. This growth interruption technique was feasible for formation of multi layer InGaN QDs structures and applicable for the fabrication of GaN-based light emitting devices.

References

- [1] M. Asada, Y. Miyamoto, and Y. Suematsu, IEEE J. Quantum Electron., 22, 1915, 1986.
- [2] G.T. Liu, A. Stintz, H. Li, Electron. Lett. 35, 1163, 1999.
- [3] Tanaka S, Hirayama H, Aoyagi Y, Narukawa Y, and Fujita S, Appl. Phys. Lett., 71, 1299, 1997
- [4] A. V. Sakharov, W. V. Lundin, I. L. Krestnikov, V. A. Semenov, A. S. Usikov, A. F. Tsatsul'nikov, Yu. G. Musikhin, M. V. Baidakova, Zh. I. Alferov, N. N. Ledentsov, A. Hoffmann, and D. Bimberg, Appl. Phys. Lett., 74, 3921, 1999.
- [5] S. Tanaka, S. Iwai, and Y. Aoyagi, Appl. Phys. Lett., 69, 4096, 1996.
- [6] Y. Arakawa, M. Nishioka, H. Nakayama, and K. Kitamura, IEICE Trans. E-79-C-11, 487, 1996.
- [7] Y. Arakawa, T. Someya, and K. Tachibana, phys. stat. sol. (b) 244, 1, 2001.
- [8] Li Jiawei, Ye Zhizhen, Nasser NM. Physica A., 16, 244, 2003.
- [9] Hirayama H, Tanaka S, Ramvall P, Aoyagi Y. Appl. Phys. Lett. 72, 1736, 1998.
- [10] Werner Seifert, Niclas Carlsson, Mark Miller, Mats-Erik Pistol, Lars Samuelson, and L. Reine Wallenberg, Prog. Crystal Growth and Charact., 33, 423, 1996.
- [11] B. Daudin, F. Widmann, G. Feuillet, Y. Samson, M. Arlery, and J. L. Rouvière, Phys. Rev. B, 56, R7069, 1997.
- [12] B. Damilano, N. Grandjean, F. Semond, J. Massies, and M. Leroux, Appl. Phys. Lett., 75, 962, 1999.
- [13] Tachibana K, Someya T, Arakawa Y. Appl. Phys. Lett. 74(1999) 383
- [14] L. Nistor, H. Bender, A. Vantomme, M. F. Wu, J. Van Landuyt, K. P. O'Donnell, R. Martin, K. Jacobs, and I. Moerman, Appl. Phys. Lett. 77, 507 (2000)
- [15] H. K. Cho, J. Y. Lee, K. S. Kim, and G. M. Yang, Appl. Phys. Lett. 77, 247 (2000)
- [16] N. Sharma, P. Thomas, D. Tricker, and C. Humphreys, Appl. Phys. Lett. 77, 1274 (2000)

- [17] F. Hofer, W. Grogger, G. Kothleitner, and P. Warbichler, *Ultramicroscopy* 67, 83 (1997)
- [18] H. Chen, R. M. Feenstra, J. E. Northrup, T. Zywietz, and J. Neugebauer, *Phys. Rev. Lett.* 85, 1902 (2000)
- [19] N. A. Shapiro, P. Perlin, C. Kisielowski, L. S. Mattos, J. W. Yang, and E.R. Weber, *MRS Internet J. Nitride Semicond. Res.* 5, 1 (2000)
- [20] Damilano B, Grandjean N, Semond F, Massies J, Leroux M. *Appl. Phys. Lett.* 75, 962, 1999.
- [21] Meixner M, Kunert R, Scholl E. *Physical Review B* 67, 195301, 2003.
- [22] Convertino A, Cerri L, Leo G, Viticoli S. *Journal of Crystal Growth* 261, 458, 2004
- [23] Leon R, Yong Kim, Jagadish C, Gal M, Zou J, Cockayne DJH. *Appl. Phys. Lett.*, 69, 1888, 1996.
- [24] D V Korbutyak, V P Klad'ko, S G Krylyuk, V G Litovchenko¹, A V Shalimov and A V Kuchuk. *Semicond. Sci. Technol.*, 19, 475, 2004.
- [25] P. P. Paskov,^a R. Schifano,^b and B. Monemar T. Paskova, S. Figge, and D. Hommel. *J. Appl. Phys.*, 98, 093519, 2005.
- [26] Wu J, Walukiewicz W, Yu KM, Ager JW, Haller EE, Hai Lu, Schaff WJ. *Appl. Phys. Lett.* 80, 4741, 2002
- [27] Van de Walle CG, Neugebauer J. *Appl. Phys. Lett.*, 70, 2577, 1997.
- [28] F. Bernardini and V. Fiorentini, *Phys. Status Solidi B*, 216, 391, 1999
- [29] Ursula M. E. Christmas, A. D. Andreev, and D. A. Faux, *J. Appl. Phys.* 98, 073522, 2005

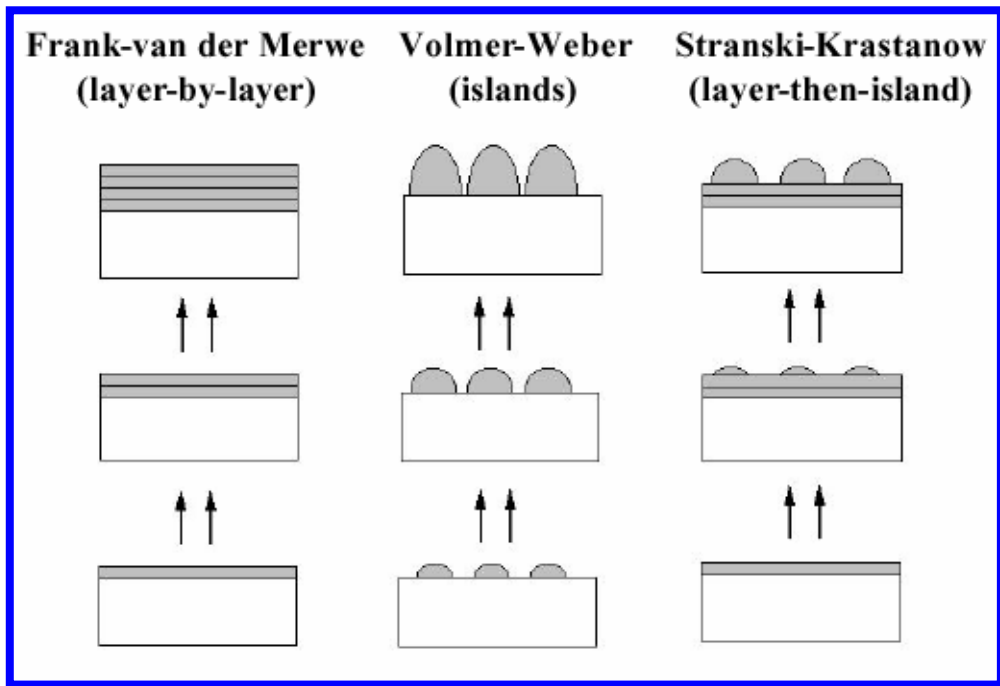


Figure 5-1 The schematic diagram of three heteroepitaxial growth modes.

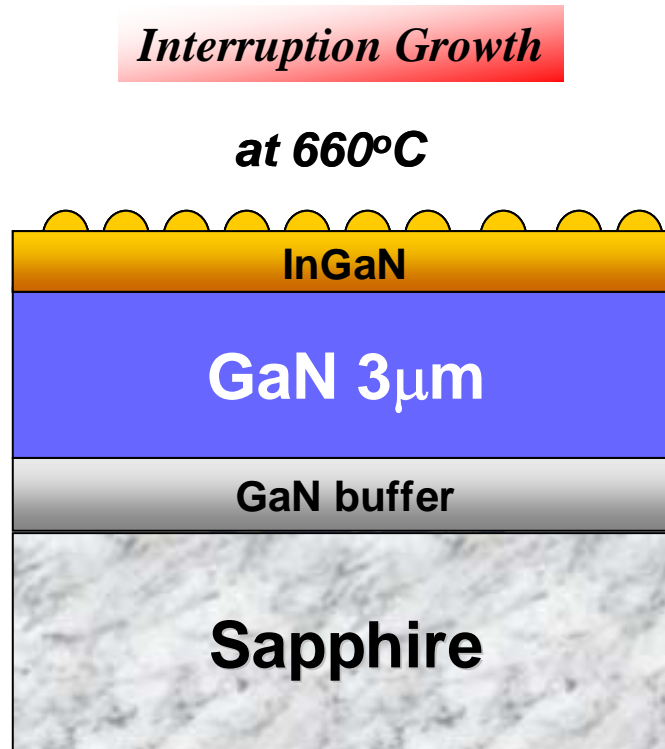
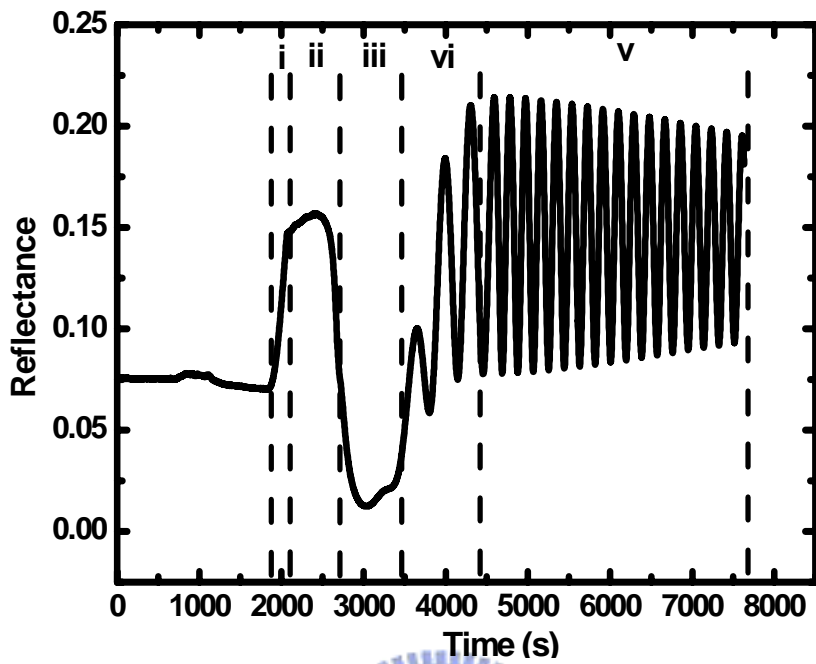


Figure 5-2 The schematic diagram of the overall InGaN Quantum Dots structure.

(a)



(b)

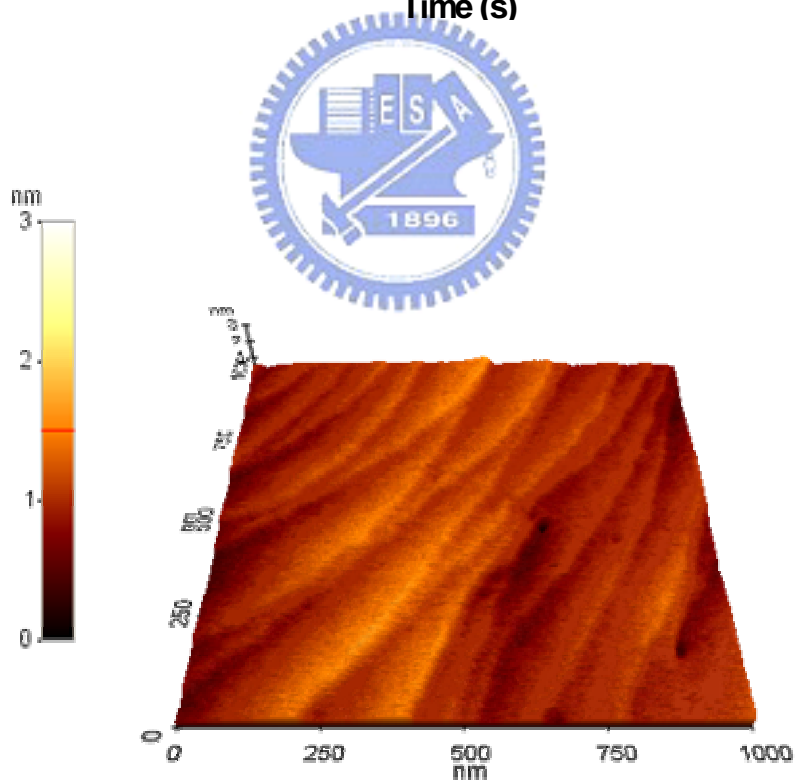


Figure 5-3 (a) The in-situ reflectance trace measurement for a whole sequence of GaN epitaxial thin film on sapphire substrate. and (b) AFM image of the GaN/sapphire template.

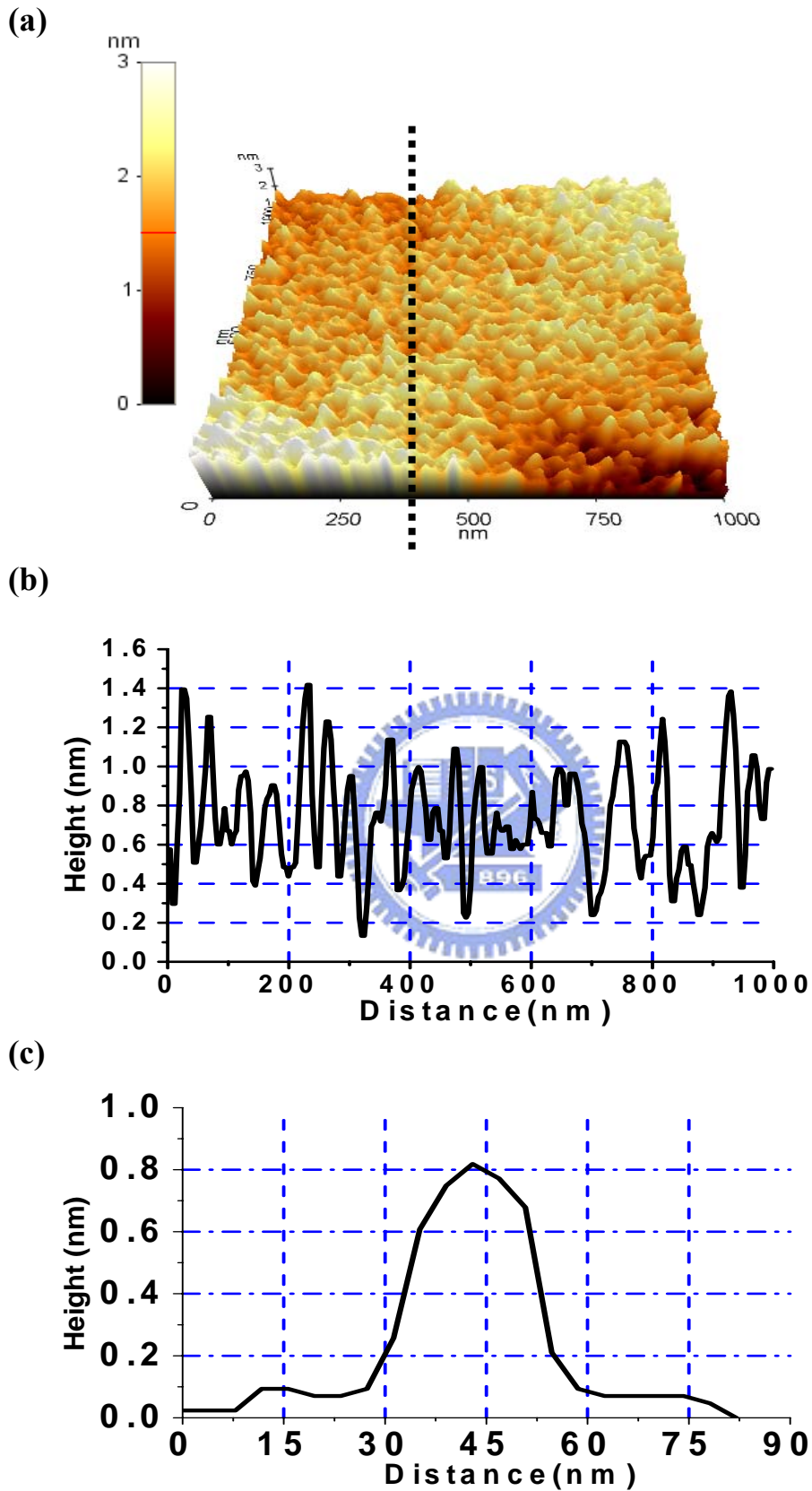


Figure 5-4 (a) An typical AFM $1\ \mu \times 1\ \mu$ image of sample B with tint = 30s, (b) section analysis along dash line in (a), (c) the shape profile of a single InGaN QD structure.

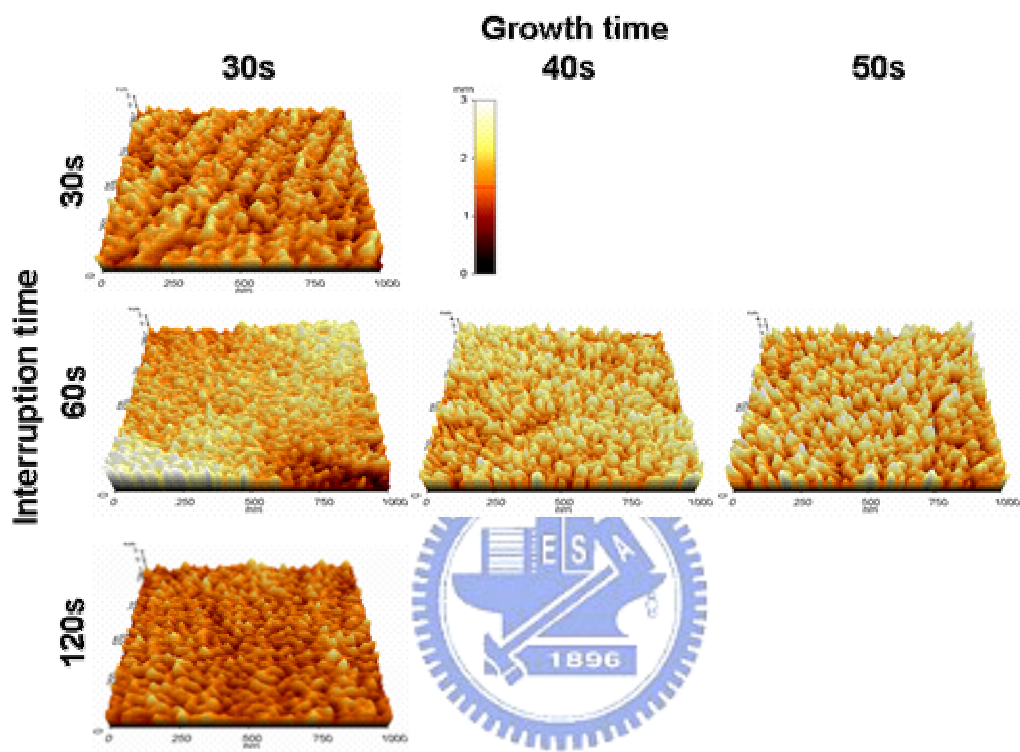
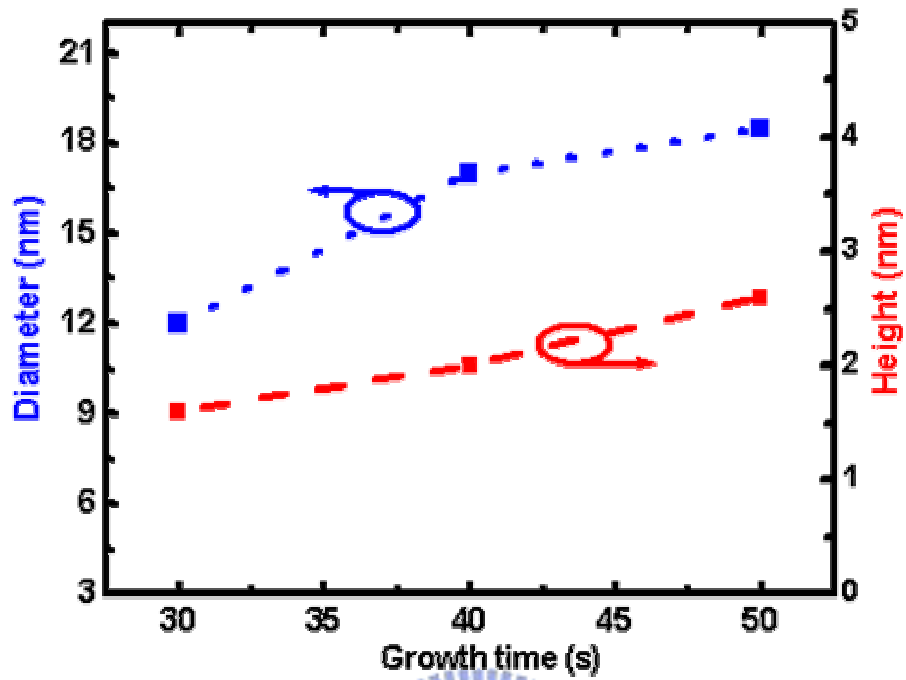


Figure 5-5 Surface morphologies of InGaN QDs under various growth and interruption times.

(a)



(b)

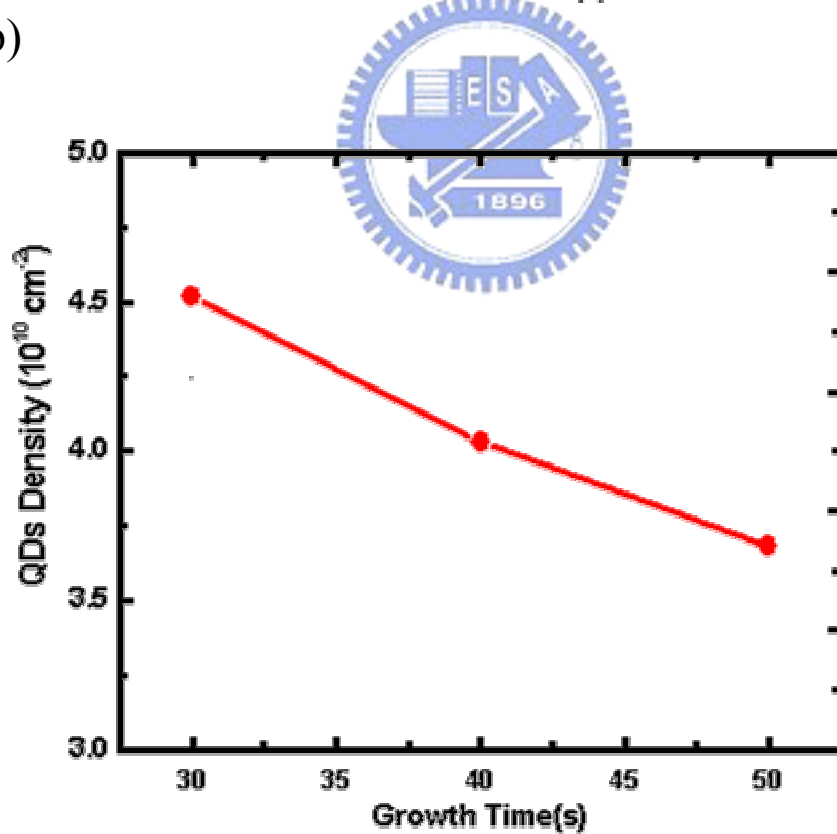


Figure 5-6 (a) Average diameter and height in dependence of the InGaN growth time, and (b) Dependence of the density of InGaN QDs on the InGaN growth time.

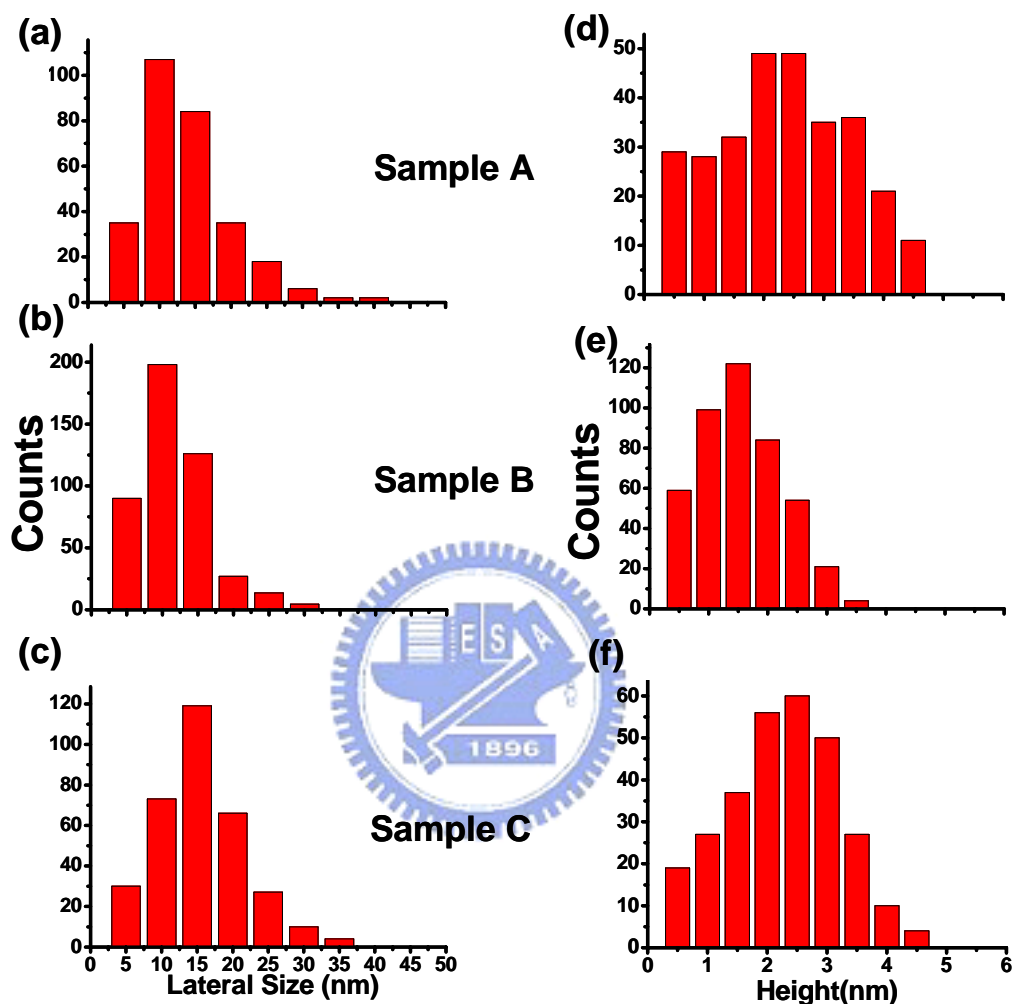
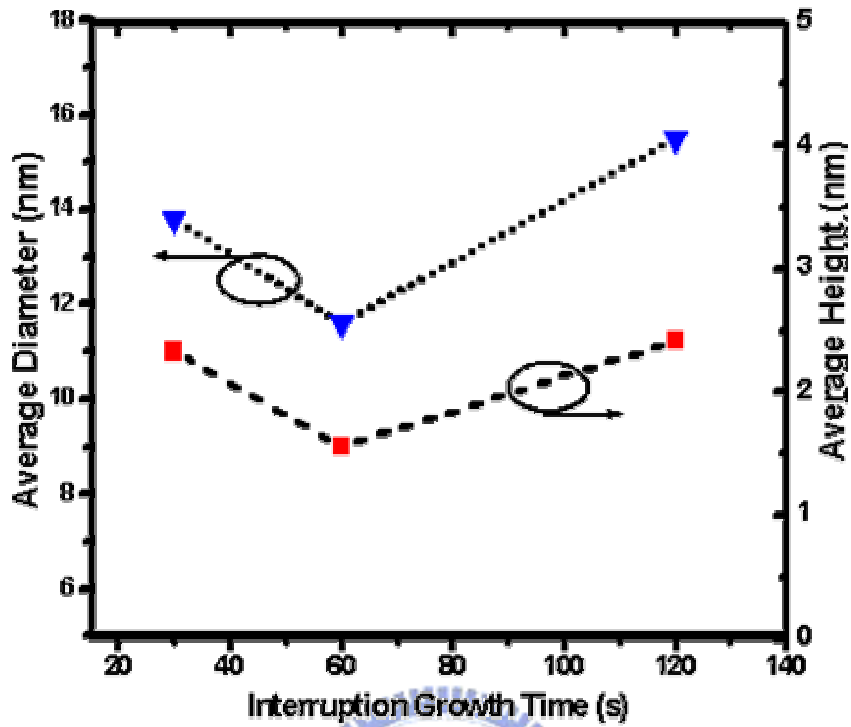


Figure 5-7 Histograms of the dot lateral size and height distribution. (a), (b), and (c) are the lateral size distribution for sample A, B, and C, respectively. (d), (e), and (f) are the height distribution for sample A, B, and C, respectively.

(a)



(b)

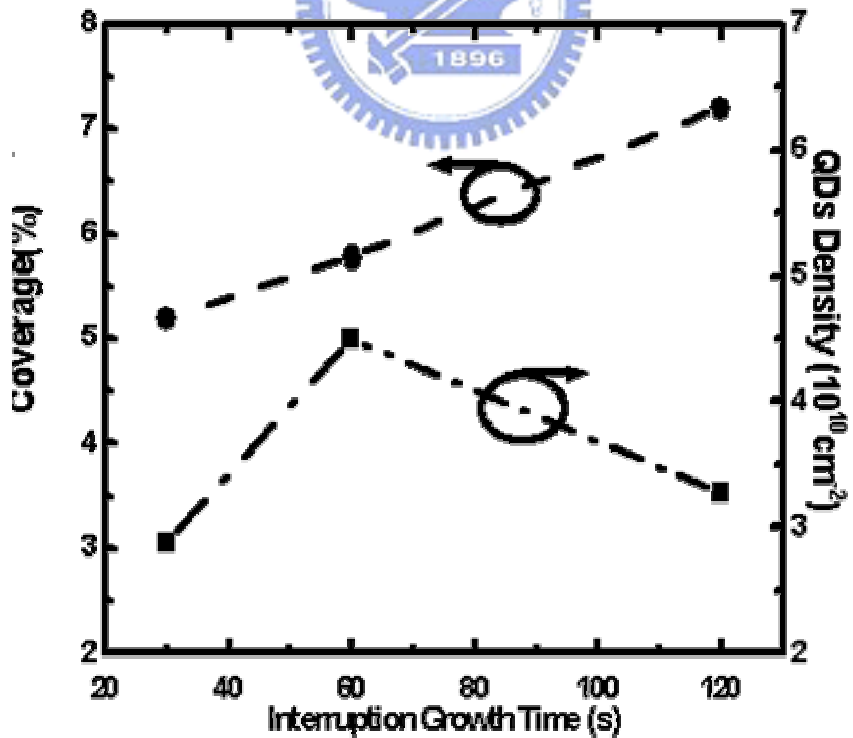


Fig. 5-8 (a) Average diameter and height in dependence of the interruption time, and (b) Dependence of the density and the coverage of InGaN QDs on the interruption time.

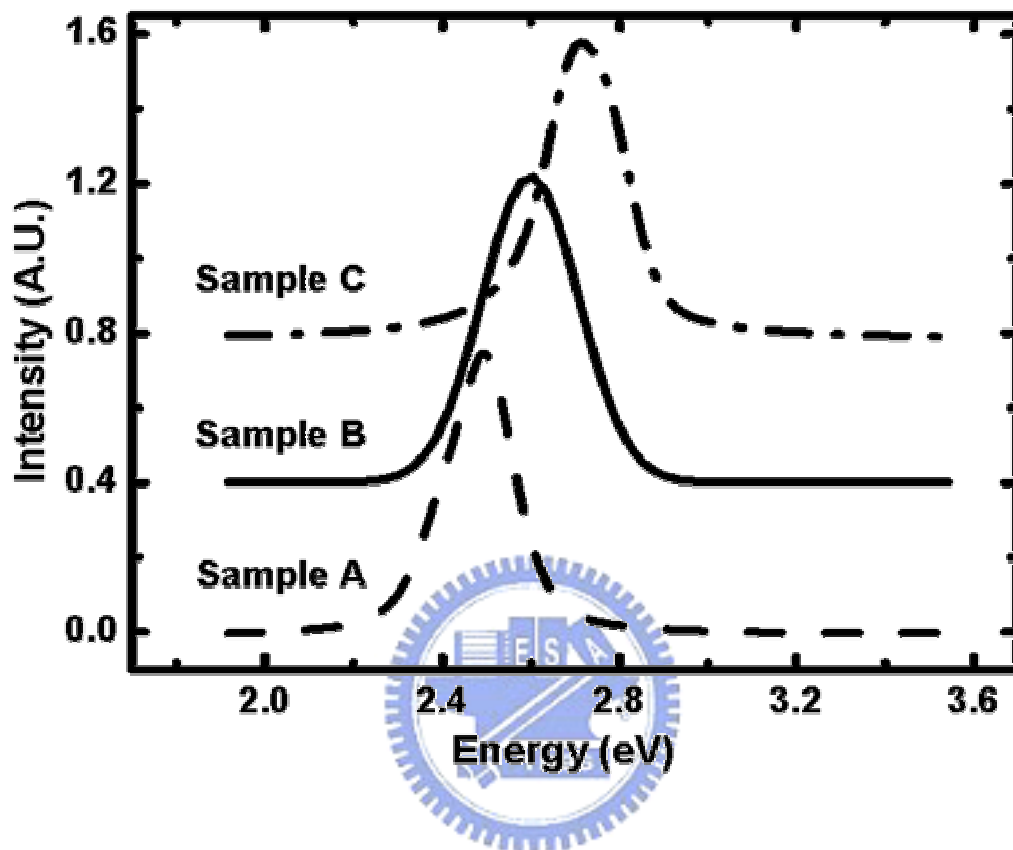


Figure 5-9 Photoluminescence spectra of sample A, B, and C at room temperature under the excitation power of 20 mW.

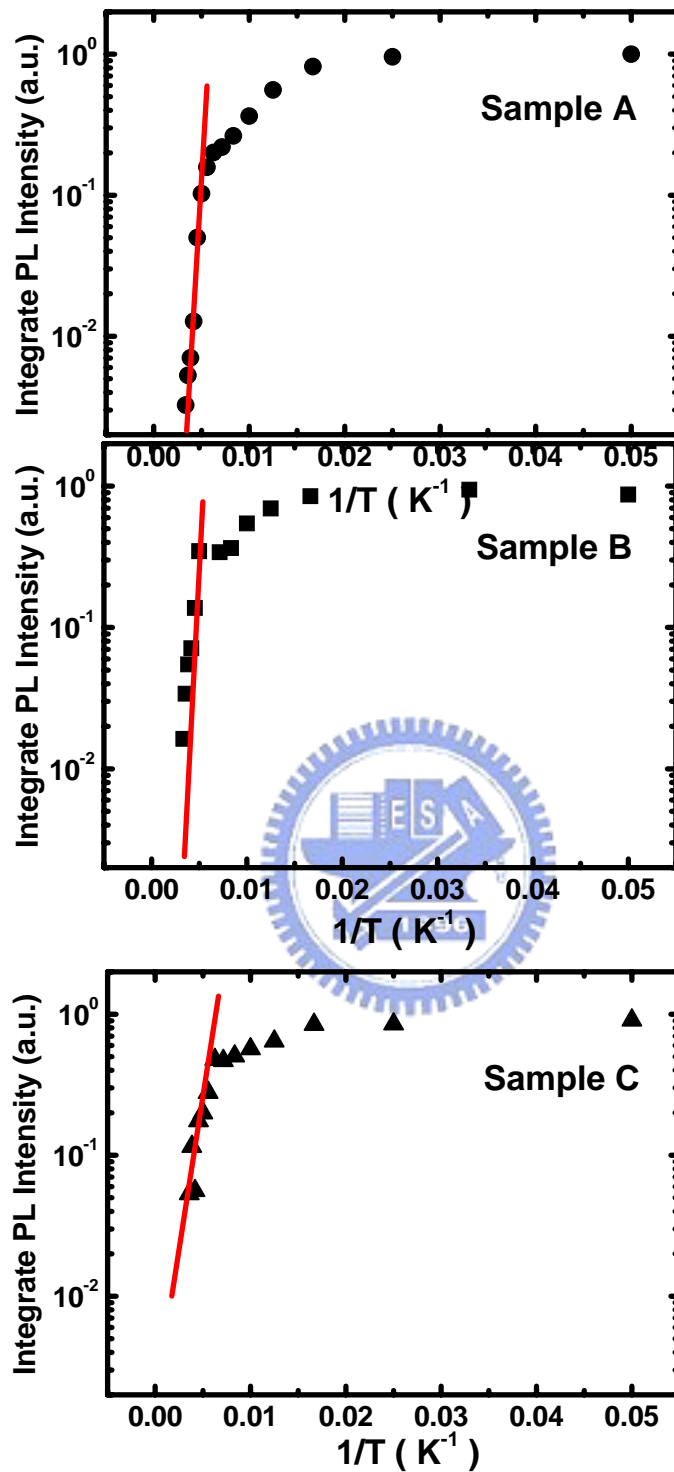


Figure 5-10 Arrhenius plots of the temperature dependence of the integrated PL for (a) sample A, (b) sample B, and (c) sample C. The solid lines are linear regressions at high temperature to extract the values of the activation energies E_a .

		AFM Results		PL Results		
Sample	t_{int}	Size (D/H) (nm)	Peak (eV)	FWHM (meV)	E_a (meV)	ΔE (meV)
A	30	14/2.4	2.497	172	63.1	-
B	60	11.5/1.5	2.590	217	89.7	120
C	120	15/2.5	2.735	189	35	230

Table 5-1. The arrangement of AFM and PL measured

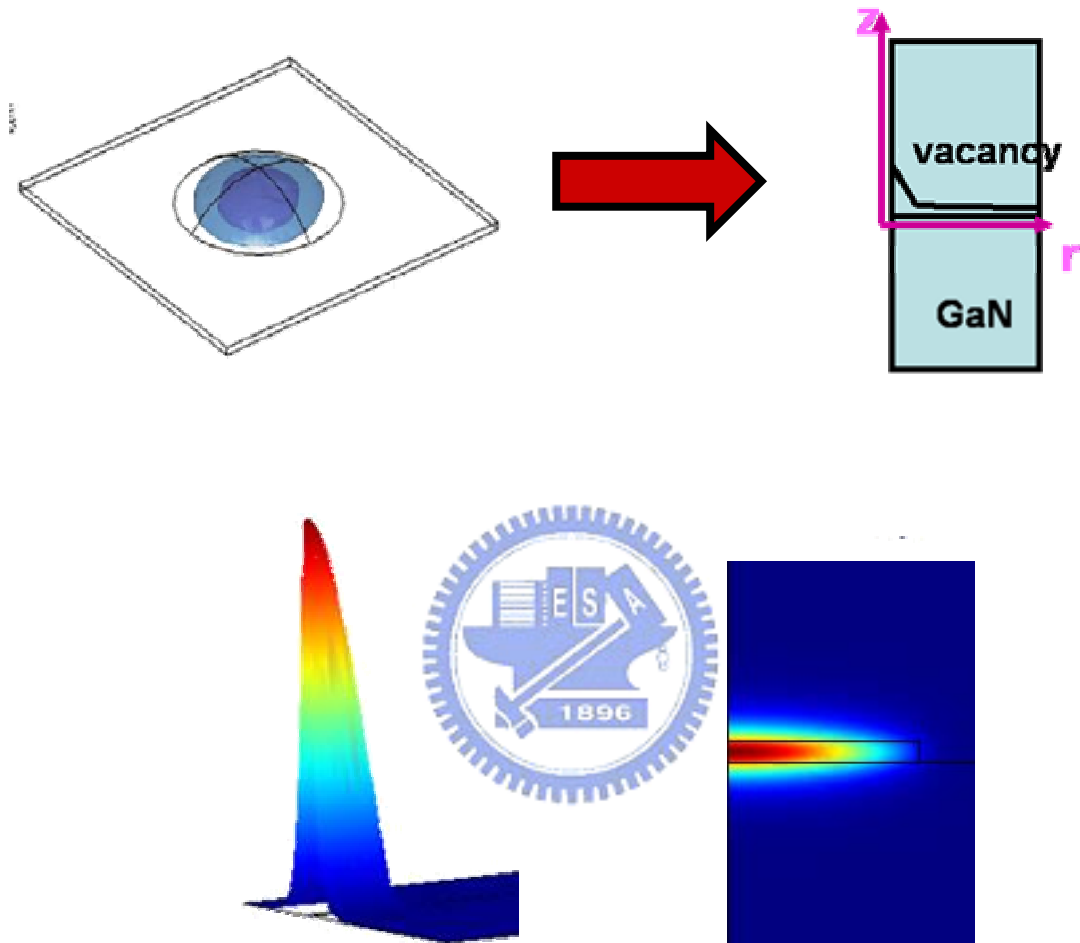


Figure 5-11 The schematic of the simulation model of InGaN QD structure.

	m_e^*	m_v^*	E_g
GaN	0.13 m_0	1.40 m_0	3.42eV
InN	0.11 m_0	1.65 m_0	0.77eV

Bowing Factor : -0.143eV
 DEc : DEv = 7:3
 Internal Electric Field F < 0.82MV/cm

Table 5-2. The necessary parameters for simulation of InGaN QDs structure

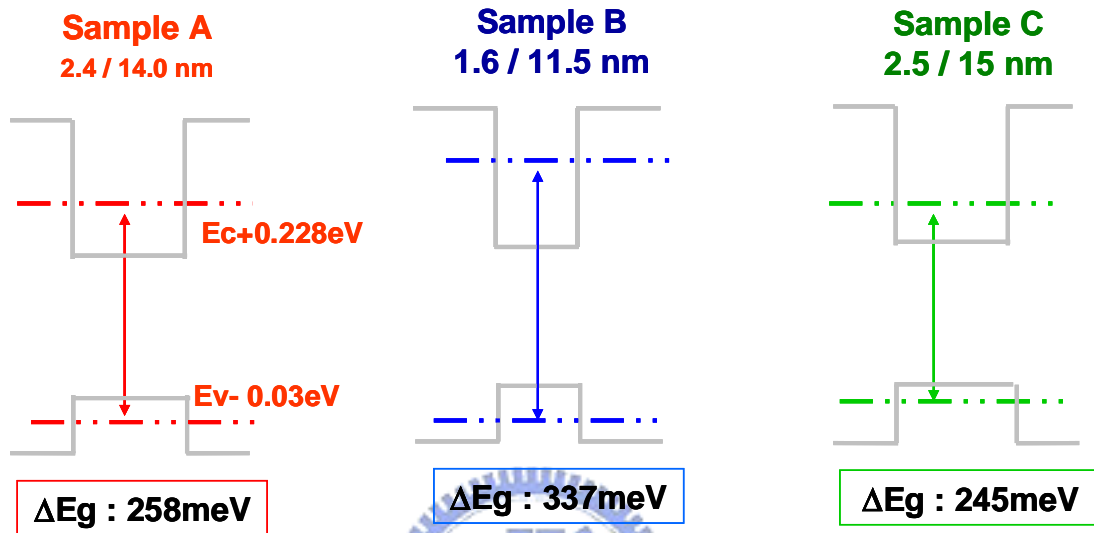


Figure 5-12 The calculation result of raise energy due to the confinement effect on electrons and holes with the same In composition for these three InGaN QD samples.

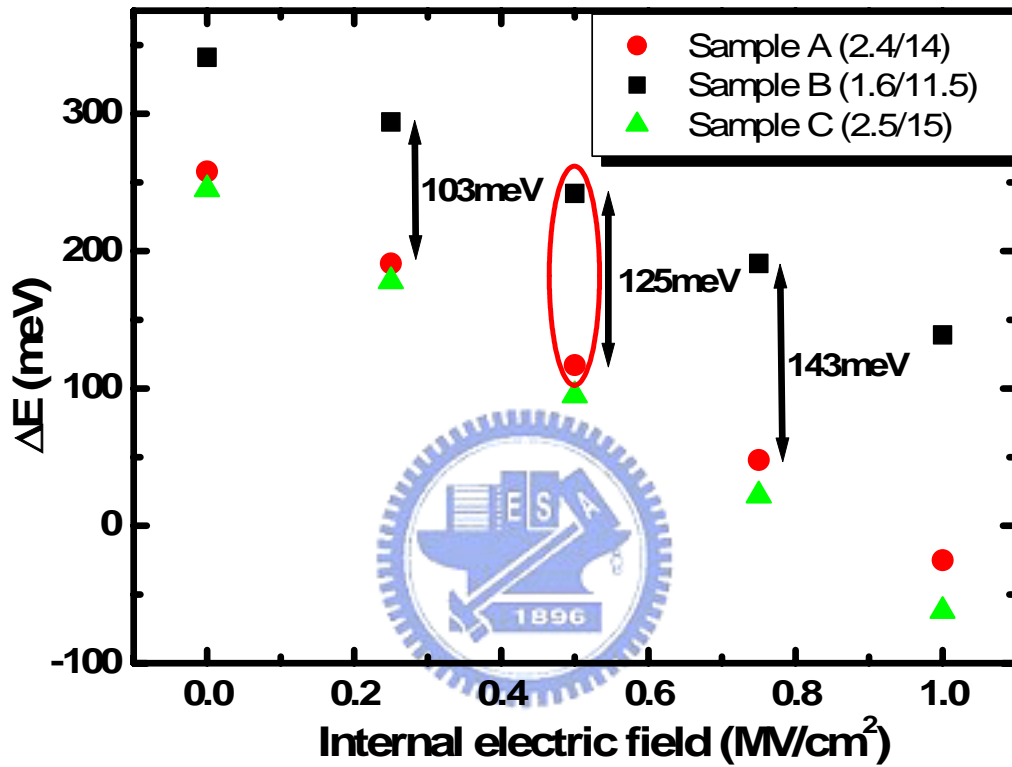


Figure 5-13 The calculation result of raise energy due to the confinement effect on electrons and holes with the same In composition for these three InGaN QD samples under various internal electric fields from 0 MV/cm to 1 MV/cm.

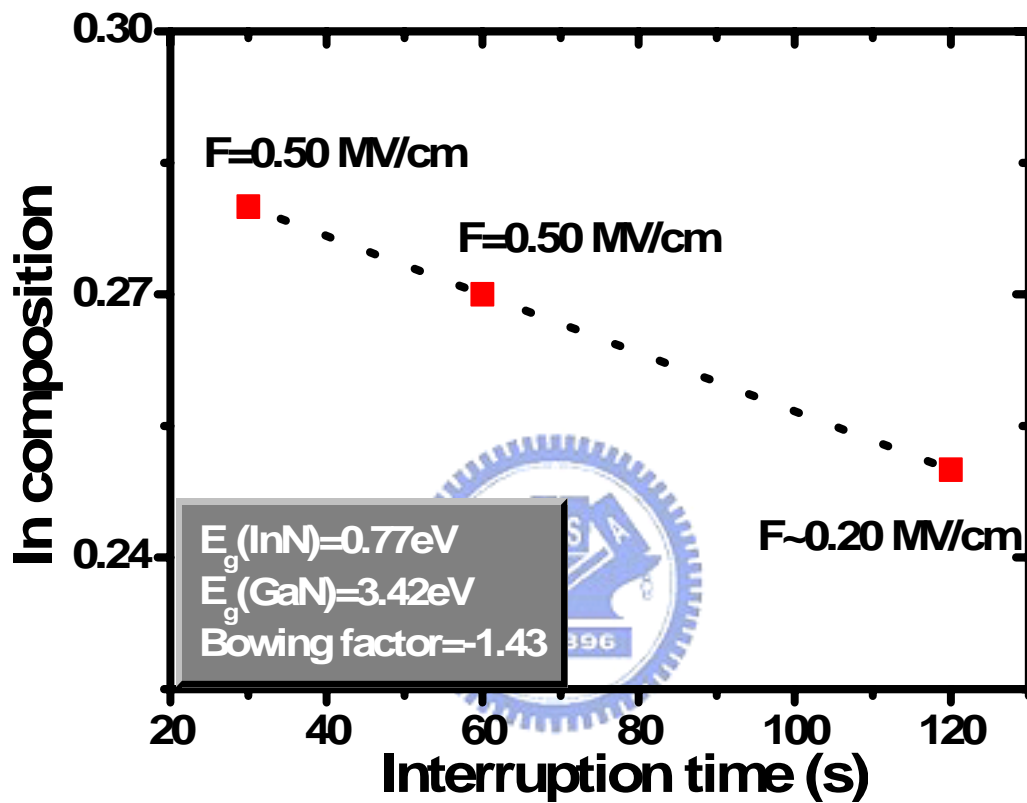


Figure 5-14 the calculation result of the In compositions for these three samples. The In compositions of sample A and B were 0.28 and 0.27, respectively. The In composition of sample C was determined by extensive method and the internal electric field was modified to 0.2 MV/cm.

Sample	t_{int}	AFM Results		PL Results			Simulation Results	
		Size (D/H) (nm)	Peak (eV)	FWHM (meV)	E_a (meV)	Internal Electric Field (MV/cm)	In Composio n	
A	30	14.0/2.4	2.49	172	63.1	0.5	0.28	
B	60	11.5/1.5	2.61	217	89.7	0.5	0.27	
C	120	15.0/2.5	2.72	189	35.0	0.2	0.25	

Table 5-3. The arrangement of analysis results for growth interruption effect on InGaN QDs structure



Chapter 6

Conclusions and Further Works

Conclusions

In this study, we have explored and fabricated the nitride-based quantum confined light emitting structures and devices, and it included the material growth, structures characterization, and device fabrication. We have achieved the following benchmarks with the assistance of modern epitaxial technology provided by metal organic chemical vapor deposition (MOCVD) system.

(1) Determination of optima growth ambient gas for AlN/GaN distributed Bragg reflectors (DBRs) structure grown by MOCVD system:

We have grown AlN/GaN DBR structure with high reflectance by MOCVD growth under pure N₂ ambient gas. For the nitride-based DBR structure, the accurately thickness of the individual layers in DBR structure is important to obtain high reflectance and wide stopband width. We have demonstrated the DBR structures with AlN layer grown under three different ambient gases; pure N₂, mixture N₂/H₂ and H₂ conditions, The AlN/GaN DBR structure grown under pure N₂ ambient gas with the highest peak reflectivity of about 94.5% with a stopband width of 18 nm at center wavelength of 442 nm was obtained. On the other hand, both the peak reflectivity and the stopband width were decreased and the center wavelengths of the DBR structures were blue-shifted. Therefore

for realization of a high reflectivity and broad bandwidth of AlN/GaN DBR by using the MOCVD growth method, the pure N₂ as the growth ambient gas should be the preferable and optimal condition.

(2) Successful fabrication of a crack-free AlN/GaN DBR structure:

We have successfully grown a crack-free AlN/GaN DBR structures on (0001) sapphire with high reflectance by MOCVD. The serious problem of surface crack generated from the tensile strain relaxed in AlN/GaN DBR structure has been resolved by growing a non-quarterwave stacks AlN/GaN DBR structure. By reducing the ratio of AlN and GaN growth thickness, the density of surface crack per unit area could be reduced. The peak reflectivity of 20-pair DBR structure is about 96% with a stopband width of 27 nm around the center wavelength of 430 nm under pure N₂ ambient gas for growth of whole DBR structure. By these approaches, the realization of high quality III-nitride DBRs with high reflectance and crack-free surface will pave the way for development of nitride-based VCSELs.

(3) Successful demonstration of optically pumped GaN-based VCSELs:

We have demonstrated a nitride-based microcavity structure with a hybrid DBR resonator and tested the quality by optically pumped the nitride-based microcavity. The nitride-based microcavity consisting of AlN/GaN DBR as bottom mirrors, a 3λ thick

cavity composed n-GaN, 10-pair InGaN/GaN MQW, and p-GaN, and Ta₂O₅/SiO₂ DBR as top mirror was fabricated. The laser action of the nitride-based microcavity was achieved under the optical pumping at room temperature with a threshold pumping energy density of about 53 mJ/cm² and emits 448 nm with a linewidth of 0.25 nm.

(4) Demonstration of nitride-based light emitting devices:

We demonstrated the property of a 3λ nitride-based microcavity light emitting device (MCLED) grown by MOCVD. In MCLED structure, the 3λ thick resonant cavity has been grown between the top TiO₂/SiO₂ DBR and the bottom AlN/GaN DBR stack. From the EL measurement of the MCLED, the emission peak localization at 410 nm with a narrow line width of 7.4 nm. Based on the resonance effect in this vertical cavity structure, the MCLEDs exhibit a higher output power and much less red-shifting with injection current: the output power was enhanced and three times the measure of the device without top DBR under 600 A/cm² injection current density, and a stable emission wavelength as varying the injecting current density with a low red-shift of 0.12 nm/kA/cm² was also measured in our nitride-based MCLED.

(5) Successful growth of an InGaN 3-D islands structure:

We have successfully grown the self-assembled InGaN QDs structures on (0001) sapphire substrates by MOCVD with growth interruption. The flat surface of

GaN/Sapphire template, and the critical growth conditions with a low V/III ratio (~8300) and low growth temperature (660°C) have been used to form the self-assembled InGaN QDs structure. The density of InGaN QDs was about $4.5 \times 10^{10} \text{ cm}^{-2}$ with an average lateral size of 11.5 nm and an average height of 1.6 nm, respectively.

(6) Demonstration of the effect of growth interruption on InGaN 3-D islands structure:

We also demonstrated the effects of the growth interruption time on the morphological and optical properties. Our results suggested that the growth interruption can modify the size of InGaN QDs and extend the emission wavelength to the short wavelength region, and at the same time improve the QD optical quality. This growth interruption technique was feasible for formation of multi layer InGaN QDs structures and applicable for the fabrication of GaN-based light emitting devices.

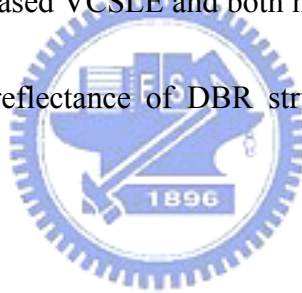
Future work

Although many benchmarks of nitride-based quantum confined light emitting structures and devices have been done, our long-term research in nitride-based microcavity structure included electrically driven continuous wave (CW) nitride-based VCSELs and single photon emitter structure has yet to be fulfilled. All previous steps will provide precious information and experience in the future. To achieve this goal, the

following actions require to be done:

(1) Improvement of nitride-based microcavity quality:

Improvement of microcavity quality can improve the collection efficiency of spontaneous emission, reduce the threshold current density of VCSELs structure, and raise the efficiency of light-matter interaction at a fundamental level. The improvement of microcavity quality included the reduction of the optical mirror loss and the internal material absorption loss in microcavity. Figure 6-1 shows the relationship of threshold current density of nitride-based VCSLE and both mirrors reflectance. Improvement of the material quality and the reflectance of DBR structure will be the initial steps in the further.



(2) Development of conductive AlN/GaN distributed Bragg reflectors:

DBR structure would be highly desirable with vertically conductive. The development of conductive DBR structures can reduce the thickness of n- or p-spacers and lets the semiconductor microcavity with shorter cavity length is possible. Although AlN is commonly believed to be invariably insulating by nature, and the huge conduction band offset between GaN and AlN (2.2 eV) seems to completely hinder a carrier flow across the heterointerfaces, A GaN/AlN DBR structure with vertically conducting is possible [1]. The fabrication of bottom AlN/GaN DBR structure with n-type doping will

be tested since we have obtained a high reflectance and crack-free AlN/GaN DBR structure.

(3) Development of a uniform current spreading p-side junction with low optical loss:

The need for lateral injection of holes from the p-side of the junction to the optically active volume poses a major challenge for nitride-based VCSELs. The commercial used of transparent contact layer is not suitable for fabrication of intracavity nitride-based VCSEL structures because of its large optical loss per single pass. Two approaches will be tested in this direction. First is using an indium-tin oxide (ITO) to replace TLC structure as the electrical contact to p-GaN. ITO will have a low optical loss if it was designed and placed at the standpoint of the light standing wave. Second is developing a nitride-based (Easki) tunnel junction structure which allows the use of low-resistivity n-type layers instead of high resistivity p-type layers as an ohmic contact layer. Both of these two structures may be very useful for nitride-based VCSEL structures.

(4) Development of multi-layer InGaN QDs structure grown by MOCVD:

To further increase the internal quantum efficiency and the filling factor of the InGaN QDs structure, not only the dot density should be increased, but the multi-layer QDs structure is essential for fabrication of high efficiency light emitting devices. The

fabrication issues of multi-layer QDs structure are included the critical growth condition for forming self-assembled QDs, the broad size distribution of QDs obtained by Stranski-Krastanov growth mode, and the new nonradiative centers not introduced during the stacking process. Although the fabrication of high quality multi-layer QDs structure is more difficult than the MQW structure, the special epitaxial technique for InGaN QDs structure has to be established in the further.

(5) Combination of QDs structure and nitride-based microcavity Structure

Microcavity light emitting devices can increase the efficiency and speed of semiconductor spontaneous light emitters. However, small sized MCLEDs suffer from edge effects due to carrier loss and nonradiative recombination that can limit their efficiency. Using QDs structure as the active layer can resolve these effects for the strong carrier localizing capability. Furthermore, semiconductor microcavity structure combined with QDs structure is the best candidates for observing the research field of Cavity quantum electrodynamics (CQED), which is one of the core issues of modern optics research field. Despite the tough work of fabricating high quality nitride-based microcavity with QDs structure, nitride-based materials are the best candidates for executing the experiments of CQED at room temperature.

(6) Nitride-based single photon emitter:

Semiconductor QDs structure embedded in microcavity structure is the candidate of single photon emitter which is needed for quantum cryptography and quantum computer. Because GaN-based materials in comparison to GaAs and InAs materials have wider direct bandgap, large conduction band offset, larger exciton binding energy, higher electrons saturation speed, high piezoelectric effect, and large electron effective mass, the GaN quantum confined microcavity structure is a much desirable device for the single photon emission allowing for higher-temperature operation. Improvement of the control on the density of nitride-based QDs structure and the resonant energy of the nitride-based microcavity will be the necessary step in the further.



Reference

- [1] Tommy Ive, Oliver Brandt, Helmar Kostial, Thorsten Hesjedal, Manfred Ramsteiner, and Klaus H. Ploog, Appl. Phys. Lett., 85, 1970, 2004



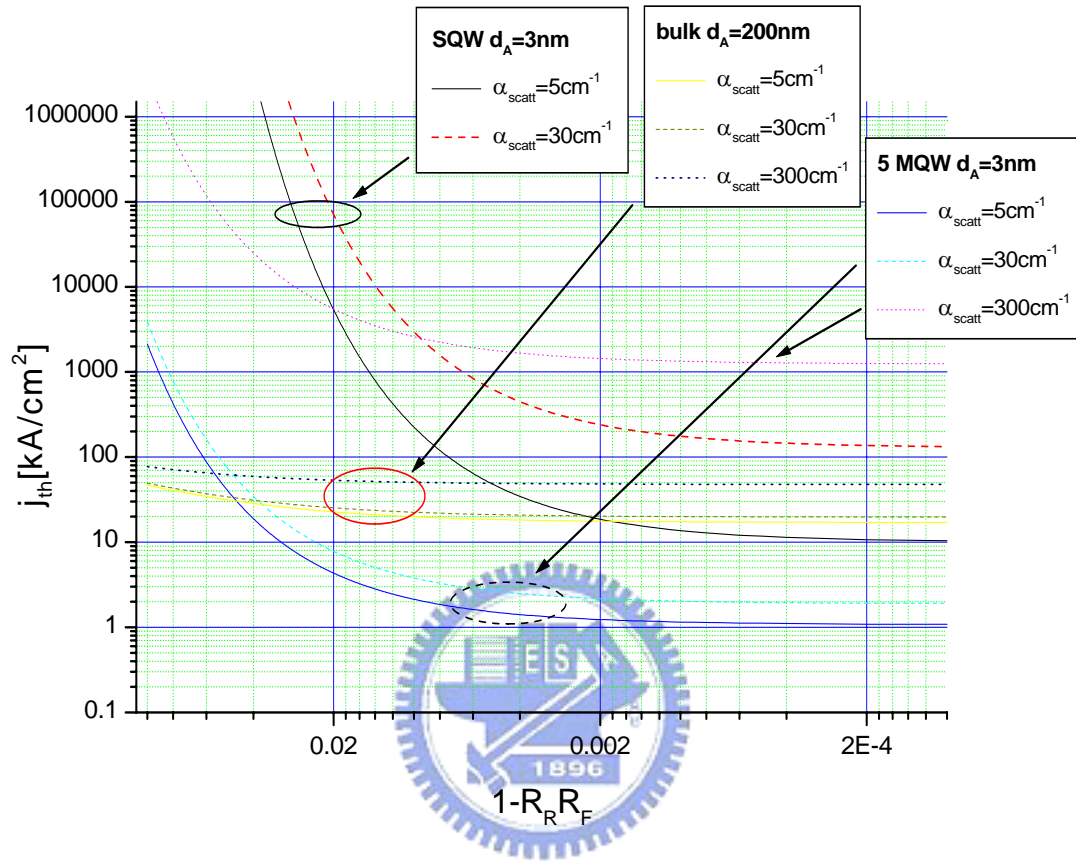


Figure 6-1 The simulation results of the threshold current density under various mirror loss and scattering loss.